ULg Library

http://lib.ulg.ac.be

http://matheo.ulg.ac.be

Study of a suction caisson foundation for offshore wind turbines

Auteur : Ortolani, Carlo
Promoteur(s) : Collin, Frederic
Faculté : Faculté des Sciences appliquées
Diplôme : Master en ingénieur civil des mines et géologue, à finalité approfondie
Année académique : 2015-2016
URI/URL : http://hdl.handle.net/2268.2/1329

Avertissement à l'attention des usagers :

Tous les documents placés en accès ouvert sur le site le site MatheO sont protégés par le droit d'auteur. Conformément aux principes énoncés par la "Budapest Open Access Initiative"(BOAI, 2002), l'utilisateur du site peut lire, télécharger, copier, transmettre, imprimer, chercher ou faire un lien vers le texte intégral de ces documents, les disséquer pour les indexer, s'en servir de données pour un logiciel, ou s'en servir à toute autre fin légale (ou prévue par la réglementation relative au droit d'auteur). Toute utilisation du document à des fins commerciales est strictement interdite.

Par ailleurs, l'utilisateur s'engage à respecter les droits moraux de l'auteur, principalement le droit à l'intégrité de l'oeuvre et le droit de paternité et ce dans toute utilisation que l'utilisateur entreprend. Ainsi, à titre d'exemple, lorsqu'il reproduira un document par extrait ou dans son intégralité, l'utilisateur citera de manière complète les sources telles que mentionnées ci-dessus. Toute utilisation non explicitement autorisée ci-avant (telle que par exemple, la modification du document ou son résumé) nécessite l'autorisation préalable et expresse des auteurs ou de leurs ayants droit.

LATERALLY LOADED MONOPILES FOR OFFSHORE WIND TURBINES: ANALYSIS AND IMPROVEMENT OF THE P-Y CURVES

ORTOLANI Carlo

Promoteurs:
COLLIN Frédéric, Université de Liège
DI PRISCO Claudio, Politecnico di Milano

Travail de fin d'études présenté en vue
de l'obtention du grade de :
Ingénieur Civil des Mines et Géologue

Année Académique 2015–2016

Summary

Résumé en Français

L'industrie éolienne offshore tente actuellement de se développer plus durablement, afin d'être compétitive sur un marché dominé par les énergies fossiles. Le développement de nouvelles technologies doit découler de l'optimisation de technologies existantes.
Les monopieux représentent de loin les substructures les plus populaires pour les éoliennes offshore: elles deviennent de plus en plus imposantes et peuvent être utilisées dans des conditions de site complexes. Cependant, il existe des preuves montrant que la méthode standard pour la conception de ces ouvrages, originellement développée pour l'industrie pétrolière et gazière et basée sur les *courbes p-y*, ne donnent pas une prédiction correcte de l'interaction entre le sol et la fondation soumise à des charges latérales. En particulier la réponse du système en terme de raideur doit être ré-examinée, vu qu'elle affecte directement la dynamique de toute la structure.
Ce travail de fin d'études suit une approche typique pour ce type de problème : avec un modèle 1D proposant les outils basiques pour implémenter les méthodes actuelles de conception, une analyse aux éléments finis 3D est développée pour des monopieux subissant une charge latérale. Une analyse détaillée des *courbes p-y* extraites est présentée pour des pieux courtes et élancées. Ensuite, en considérant des argiles tendres, une comparaison directe entre les résultats numériques et les prédictions des méthodes standards est effectuée, afin de donner des indications spécifiques pour l'amélioration des courbes.

Abstract in English

The offshore wind energy industry is setting the basis for a more sustainable expansion, in order to be competitive in a market still led by fossil-fuel-based energy sources. The development of new technologies must be supported by the optimization of existing technologies.
Monopiles are by far the most popular substructure type for offshore turbines, becoming larger and suitable also for complex site conditions. Nonetheless, there is evidence that the standard design method, originally conceived for the oil and gas industry and based on the *p-y curves*, does not provide a correct prediction of the interaction between soil and foundation under lateral loads. In particular the stiffness response of the system must be re-assessed, as it affects directly the dynamics of the overall structure.
This thesis follow a typical approach for this kind of problem: along with 1D modelling providing the basic tools to implement the existing design methods, a 3D finite element analysis is developed for a monopile under lateral loading. A detailed analysis of the extracted *p-y curves* is presented for slender and short piles. Then, with a focus on soft clay soils, a direct comparison of numerical results with the standard methods prediction is conducted, resulting in specific indications for future improvement of the curves.

Riassunto in Italiano

L'industria eolica sta gettato le basi per una espansione più sostenibile, allo scopo di essere competitiva in un mercato ancora guidato dalla produzione di energia da combustibili fossili. Lo sviluppo di nuove tecnologie deve essere affiancato dall'ottimizzazione delle tecnologie esistenti.
I monopali sono di gran lunga le sottostrutture più utilizzate per turbine offshore, crescendo di dimensione e potendosi adattare anche a siti dalle condizioni più complesse. Tuttavia, ci sono evidenze che il metodo di design standard, originariamente concepito per l'industria estrattiva di gas e petrolio e basato sulle *curve p-y*, non caratterizza in modo adeguato le interazioni tra suolo e fondazione sotto carichi laterali. In particolare, la risposta in rigidezza del sistema dev'essere rivalutata, poiché essa influenza direttamente la dinamica dell'intera struttura.
Questa tesi segue un approccio tipico per questo tipo di problema: assieme ad un modello 1D in grado di fornire gli strumenti base per l'implementazione dei modelli standard esistenti, si sviluppa un modello 3D di analisi agli elementi finiti per monopali sotto carichi laterali. Un'analisi dettagliata delle *curve p-y* ottenute viene presentata per monopali snelli e corti. Infine, con particolare attenzione a argille soffici, si conduce una comparazione diretta dei risultati numerici con le previsioni fornite dai metodi standard, giungendo così a specifiche indicazioni atte ad una migliore definizione delle curve.

Contents

Chapter 1

Introduction

1.1 Background

> "The world is now aware that the problems due to the dependence on oil and increasing carbon emissions must be solved. Breaking the dependence on fossil fuels offers many opportunities for strengthened competitiveness, technological development and progress."
>
> — Bakmar Christian LeBlanc

Offshore wind power is a domestic, sustainable and largely untapped energy resource. It establishes itself as an alternative to fossil fuels and a key technology in achieving the energy and climate goals of the future, helping reduce carbon emissions, and decreasing the economic and supply risks associated with reliance on imported fuels [1].
Nonetheless, the offshore wind industry currently relies on subsidy schemes to be competitive with fossil-fuel-based energy sources; therefore, a significant cost reduction for future projects is vital for this industry to survive. The development of new technologies must be supported by the optimization of existing technologies, with a special focus on design methods [2].
Last year, monopile substructures remained by far the most popular substructure type, with a net total of 385 installed worldwide - a share of 97%. Their simple design is well suited to mass fabrication, as well as their installation approach, a conventional impact driving-based, is considered as low-risk and robust for most soil conditions. While monopiles are typically designed for relatively shallow water depths - below 35 meters - designers are considering more and more the transition into deeper water, where other foundation types are usually preferred, as well as the development of larger turbines. In fact, as the reduction of costs has become a key issue, the ability to adapt to more complex site conditions - up to 70 meters of water depths - supported by the development of larger turbines - from 3-4 MW to 5-8 MW of capacity - may set the basis of a further and more economically sustainable expansion of the industry.

In this approach, a better characterization of the soil-structure interaction under lateral loading is required. For slender, small diameter pile-based turbines, this would allow a more accurate prediction of their fundamental frequency, so that an improved control on the overall performance and power production; in fact, in terms of serviceability, the dynamic response of the upper structure depends heavily on the pile-soil stiffness. As the pile diameter increases, the characterization have to be improved even more, since the actual methods may not guarantee reliable results for this new type of foundation.
The standard method lies on the *p-y curves*: they provides the non-linear relationship between lateral deflection and horizontal soil pressures in laterally loaded piles. While at large displacements the ultimate lateral resistance characterizes the failure condition, the behaviour at small displacements is governed by the initial slope. Specific recommendations are provided, especially by the norms API (American Petroleum Institute [11]) and DNV (Det Norske Veritas [12, 13]), to properly build the first part of the curve; however full-scale measurements on existing wind farms have remarked the low accuracy of this procedure, in particular in terms of underestimation of the natural frequency.

In addition, the *p-y curves* improvement should take in account the eventual change in geometry: a bigger diameter is thought to lead to additional resistances along and at the base of a pile.

The problem is usually tackled by means of 3D numerical modelling coupled to field measuring campaigns, useful to re-asses the existing mechanical laws, along with 1D modelling, which provides the tools to compare different design methods. An example of this approach in the study of lateral loaded piles is the *PISA* project (Pile Soil Analysis)[4, 5], currently one of the most advanced research program on the subject; it represents the main source of inspiration for the work presented in this thesis.

1.2 Objectives

With focus on monopiles foundations for offshore turbines, the main goal of the thesis is to provide a full analysis of the soil-pile response under lateral monotonic loads. The system is characterized in terms of *p-y curves* and the numerical modelling is realized by means of LAGAMINE, a 3D finite element code developed by the University of Liège.
In addition, we make use of a 1D finite element code in PYTHON, developed during an internship at Cathie Associates[6], in order to compare the 3D analysis to the standard design method based on the API norms. The specific case of soft clays is considered: along with an assessment of the API *p-y curves*, further indications are given regarding the new method proposed by Jeanjean (2009)[41], aimed to an overall improvement of the curves.

Two different monopile geometries are investigated: while for slender piles the 1D standard method based on lateral springs is generally assumed to be valid, this might not be the case for short piles, for which additional diameter and base effects should eventually be taken into account.

1.3 Structure of the thesis

Chapter 1 contains the introduction to the thesis, including the background of the work and its main objectives.

Chapter 2 provides an overview on offshore wind farms, with a focus on common support structures and the typical loads applied to offshore turbines.

In chapter 3 we approach to the design of foundations, with a specific revision of design methods for monopiles in terms of both axial and lateral capacity. More details are given for soils under static lateral loading and the definition of the *p-y curves*.

In chapter 4 we present the 1D finite element model. Along with some details of the formulation - for which we refer also to the appendices - the process of cross-validation is resumed. In addition, we propose some modifications to the standard model based on lateral springs, by introducing a more complex formulation for the beam and additional base resistance contributions.

Chapter 5 contains the 3D finite element analysis, aimed to the extraction and analysis of the *p-y curves*. Two geometries are investigated, corresponding to slender and short-large piles under lateral loads. In the first case a simplified model provides a sensitivity analysis aimed to identify all the phenomena contributing to the soil-pile response, while a full model helps to reproduce more realistic conditions; we proceed in the same way for the second case, for which the simplified model is useful to highlight some typical geometry-related features.

Chapter 6 is dedicated to a more realistic case of monopiles in soft clay. For the two geometries and by means of the full models, we compare the results of the 3D simulations with the standard methods prediction. In particular the 1D code is calibrated with the *p-y curves* according to API/Matlock

(1970) and Jeanjean (2009) formulations, for which an overall evaluation is proposed along with some indications aimed to their improvement.

Chapter 7 summarizes the main conclusions and results of the thesis, including the limitations of the method and some proposals for future works.

The appendices are mainly dedicated to detailed formulation and structure of the 1D code.

Chapter 2

Offshore Wind Farms

2.1 Introduction

In 2002, the first large-scale offshore wind farm was installed in Denmark [1]. Over the past 10 years, strong political and industrial forces, especially in northern Europe, have supported the development of the offshore wind industry, which provides competitive production prices for renewable energy. Political strategies in Europe and, more recently, in the United States aim to enlarge to the wind energy sector in order to limit the dependence on oil, gas and coal [18].
At the end of 2015, 3′230 turbines were installed and grid-connected, making a cumulative total capacity of 11 GW; including sites under construction, there are 84 offshore wind farms in 11 European countries [3]. Countries leaders in the European market are UK, Germany, Denmark, Belgium and Netherlands (Figure 2.1), with installation concentrated in the North Sea, Irish Sea and Baltic Sea.

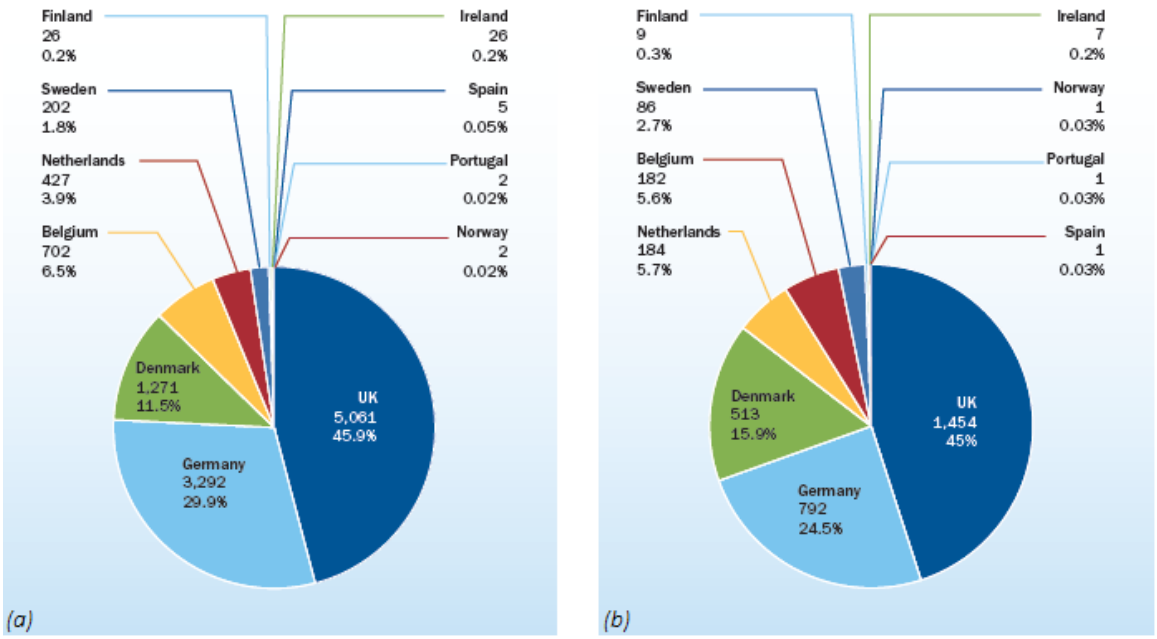

Figure 2.1: Cumulative share by Country: installed capacity in MW (a) and installed offshore wind turbines (b), after EWEA 2015 [3].

Disadvantages of onshore wind turbines concern the land occupation, as dense populated and existing built-up areas limit suitable locations, and the increasing size of structures, due to logistic problems during transportation of large components. Such limitations do not exist for offshore turbines, as seas potentially offer infinite sites and ships and barges can easily accommodate large structures.
On the other hand, construction costs offshore are higher than onshore, and an important factor is support structures, accounting for about 25-30% of the total cost. The economical feasibility has been

increased as turbines became bigger and more efficient: from 2010 to 2015 wind turbine capacity has passed from an average of 3 MW to 4.2 MW, with an increased deployment of 4-6 MW turbines - a gradual introduction of 6-8 MW turbines in 2018 is expected. In the same period, the average wind farm size has more than doubled, from 155.3 MW to 337.9 MW, and selected sites have moved further from shore and into deeper waters. At the end of 2015, the average water depth of grid-connected wind farms was 27.1 m and the average distance to shore was 43.3 km (Figure 2.2).

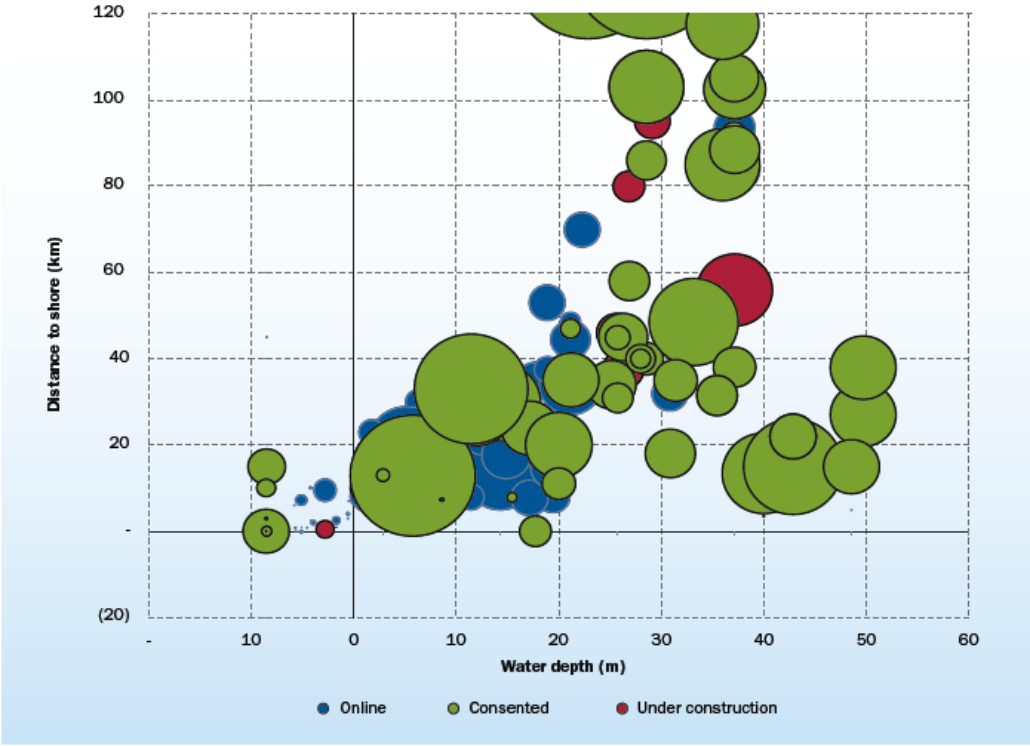

Figure 2.2: Average water depth and distance to shore of online, under construction and consented wind farms, after EWEA 2015.

However, the cost of energy still must be reduced to enable wind energy to be more commercially viable: the development of new and more cost-effective technologies must be supported by the optimization of existing technologies [2]. At this purpose, substructure design methods must be optimized and adapted to bigger superstructures and deeper waters, along with the introduction of innovative, low-cost and low-risk concepts.

2.2 Governing Dynamics of Offshore Wind Turbines

Offshore wind turbines are dynamically loaded structures, with loads arising from the wind, waves and the rotor excitations. In the dynamic analysis of structure, we can distinguish the first excitation frequency, which is the rotational frequency of the rotor (f_{1P}), and the triple-blade passing frequency ($f_{3P} = 3f_{1P}$), which primarily arises due to aerodynamic impulse loads as the blades pass the tower (Figure 2.3). Similarly, site-specific spectral densities typically present wave frequency peaks between 0.1 and 0.3 Hz, depending on wind speed and site conditions.
To avoid resonance, the overall structure - turbine, tower, support structure and foundation - have to be designed with a fundamental/natural frequency f_0 (first tower bending frequency) that is different from the rotor and wave frequencies [18]. The most common design method refers to a soft-stiff structure, for which the fundamental frequency is in the range between f_{1P} and f_{3P}: in the foundation, this results in a lower required stiffness, thereby in less need for steel [1]. For small turbines, f_0 is usually towards the top end of the wave frequencies, while is around 0.20– 0.23 Hz for a 6–8MW offshore wind

turbine on a monopile.

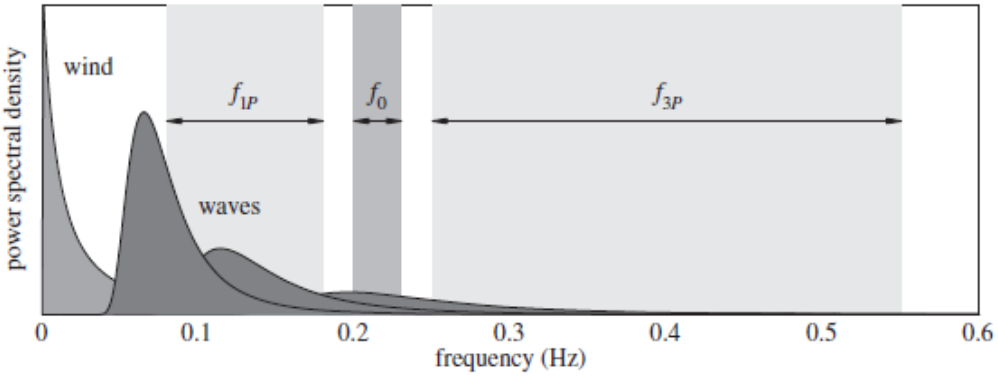

Figure 2.3: Illustration of typical excitation ranges of a modern offshore wind turbine. Wave spectra represent different wind speeds. Not to scale [2].

As the tendency in the future is to build larger turbines, with taller towers and heavier nacelles, the rotation frequency will decrease and the range between f_{1P} and the hydrodynamic excitation (soft-soft range) is likely to disappear; furthermore, the natural frequency of the higher towers will decrease more rapidly - with the height squared - falling in the region of wave frequencies. This will impose even greater demands on the design of the support structure, which would need to be made stiffer by using more or higher quality material.

We now understand how a proper characterization of the soil-structure interaction under lateral loading can have an impact on the overall design. In particular, natural frequencies are related to small displacements, so to the stiffness response of the pile-soil system. With current p-y curves methods, this stiffness is not always well defined, resulting in a wrong estimation of f_0: measurements on 400 offshore wind turbine structures supported by monopiles show that f_0 has generally been under-predicted, implying reduced loads and greater life expectancy (Figure 2.4). As a result, improved p-y curves could allow a further optimization of future structures.

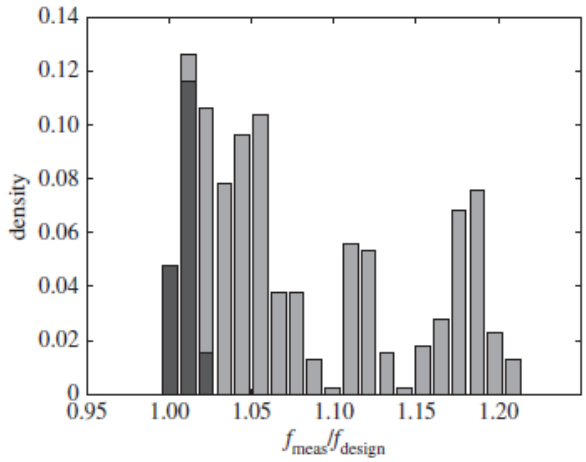

Figure 2.4: Measured first tower bending frequency (f_{meas}) compared to the design frequency (f_{design}) for 400 offshore wind turbines. Dark grey,West of Duddon Sands OffshoreWind Farm; light grey, other offshore wind farms (Kallehave, 2015).

2.3 Typical Support Structures

Several concepts for offshore wind turbines support structures exist, each characterized by advantages and limitations. Geotechnical site conditions and water depth are usually the primary design drivers: along with transportation, logistics and installation, they determine the cost-effectiveness of a particular substructure [1].
The support system refers to the foundation, transition piece, and scour protection [20]. It typically extends from below seabed level to above the splash zone, while the interface to the turbine tower is located up to 20 m above the mean sea level. The entire substructure is meant to be moment resistant, by transferring this load to the surrounding soil either by way of a single (monopod) or multiple (multipod) interface. This interface can be realized with different solutions, each of which has a limited range of application with respect to the site condition (Figure 2.5). A typical classification proposed by the Center for Wind Energy (at JMU [21]) is based on the water depth: we distinguish shallow, transitional and deep waters, respectively ranging from 0 to 30 meters, 30 to 60 meters, 60 to 900 meters.
A review of the main types of foundation is now presented, referring to [20, 1, 18, 21, 3, 13].

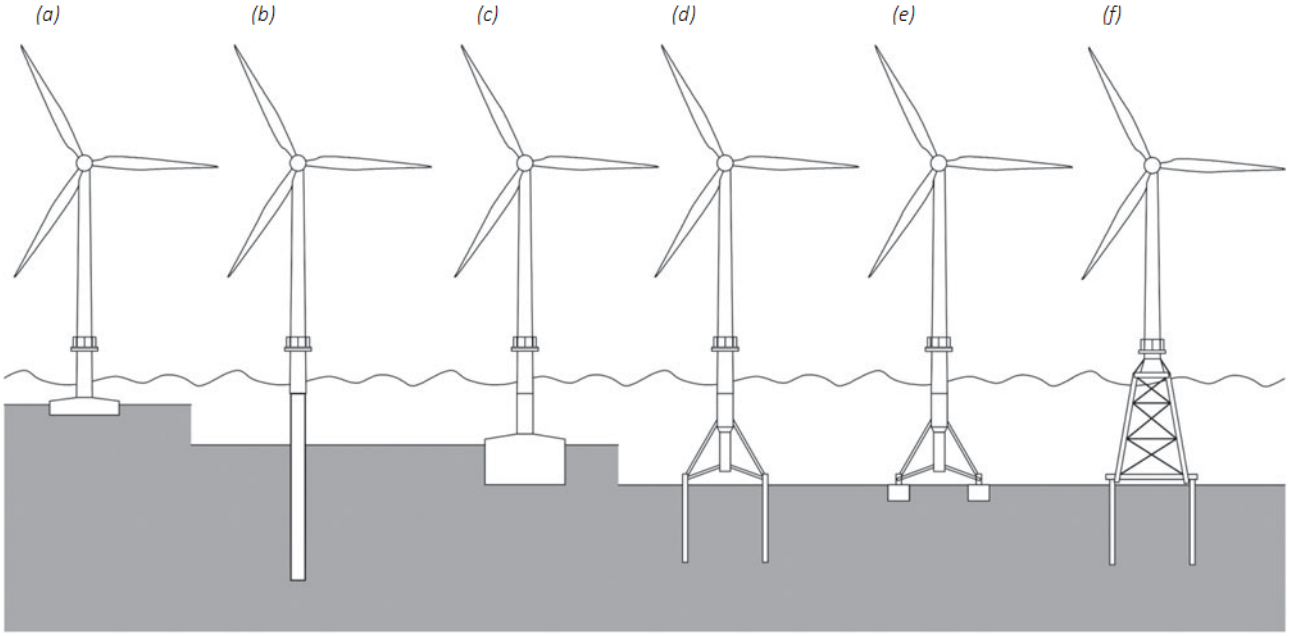

Figure 2.5: Some typical foundation concepts in function of the water depth (Kallehave 2015). Share on commercial projects of main types, as of February 2016 [3]. (a) Gravity-based foundation (9.1%), (b) monopile foundation (80.1%), (c) caisson foundation, (d) multipile foundation, (e) multi caisson foundation and (f) jacket foundation (5.4%).

2.3.1 Gravity-based foundations

Gravity-based foundations are concrete or steel structures that resist the overturning loads solely by means of its own self-weight (Figure 2.5.a). Their application is limited to shallow waters, usually less than 10 meters, due to installation costs and the difficult handling of the large weight: in fact, they are usually built onshore, then transported and lowered into place using cranes. Once in place, filling material such as sand or gravel can be added to achieve the required weight, ranging from 1400 to over 3000 tons, guaranteeing the wanted stability.
Loadings are transferred by a large base to the seabed; hence, an extensive ground preparation must be carried out before installation, consisting in silt removal and seabed levelling. The upper sediment layers should have a limited inclination and sufficient bearing capacity: if smooth enough, sites presenting hard rock ledge or competent soil can be particularly suitable, while installation of piles would

be difficult.
The cost-effectiveness of gravity foundations is due to the cheap fabrication costs, while installation costs are higher with respect to monopiles.

2.3.2 Monopiles

Monopiles are large diameter, thick walled, steel tubulars that are driven (hammered) or drilled (or both) into the seabed, in water depths up to 35-40 m (Figure 2.5.b). They are the most commonly deployed foundation structure used in the offshore wind energy industry due to lower cost and simplicity: the simple design is well suited to mass fabrication, as well as their installation approach is considered as low-risk and robust for most soil conditions. In addition, comparing to relatively new foundation concepts, monopiles design principles have been well coded and are well known, even if the non-linear interaction with the surrounding soil is still object of study.
Diameters (D) usually range from 4 to 6 meters, with lengths (L) around 30 to 50 meters. These are said to be slender piles ($L/D > 5$), characterized mainly by a bending behaviour when laterally loaded. As designers are now considering more and more shorter piles ($L/D < 5$), for which rigid deflections prevail, bigger diameters would be involved, up to 8-10 meters (Figure 2.6): this would allow the construction of larger turbines - from 3-4 MW to 5-8 MW of power capacity - and the installation also in deeper waters - up to 70 meters. For both types, thickness, usually $\sim 1\%D$, and penetration depth, $\sim 40 - 50\%L$, depend on specific factors such as design load, soil conditions, water depth and environmental conditions.

Figure 2.6: A 7.5 m diameter monopile for GodeWind OffshoreWind Farm [19].

Depending on the subsurface conditions, piles are driven into the seabed by either large impact or vibratory hammers, or grouted into sockets drilled into rock; efficiency and cost-effectiveness of the installation decreases when drilling is preferred to driving. Some seabed preparation might be required, such as the laying of gravel to prevent erosion; however, compared to gravity base foundations, monopiles have minimal and localized environmental impact.

2.3.3 Suction Caissons

Suction caissons are simple steel fabrications consisting of a centre column connected to a steel bucket through flange-reinforced shear panels, able to distribute loads from the centre column to the edge of the bucket itself (Figure 2.5.c).
They are well suited for shallow depths and the installation method is simple and quick: the caisson is allowed to settle into the seabed and suction is applied by mean of a pump attached to the head. This helps the structure to pull itself deeper in the sediments and to behave as a gravity foundation, relying on the weight of the encompassed soil. The stability is ensured by the limited period of a wave,

whose action does not last enough for the bucket to be definitively pulled from the soil.
Comparing to monopile foundations, suction caissons are lighter and more durable structures, providing a greater resistance to vertical and lateral loads due to the larger diameter. They are also easier to install and to remove during decommissioning - it suffices to apply a pressure inside.

2.3.4 Tripods

Tripods can substitute monopiles to limit the deflections of the wind towers in transitional waters. Instead of entering directly the soil, the pile lies on a pre-fabricated steel frame: this frame, triangular in plan view, consists of steel pipe members connecting each corner and is able to distribute loads from the tower onto three steel piles, driven into the seabed to a certain depth, depending on the seabed geology and water depth (2.5.d). Solutions with tripod structure equipped with suction bucket anchors instead of piles exist as well (2.5.e).
The structure is constructed onshore and transported by barge to the site, in which a minimal seabed preparation is sufficient.

2.3.5 Jackets

Jacket foundations, also called braced lattice frames, represent an adaptation from the oil and gas industry and have been installed a sites hundreds of meters deep. As a modification of tripod frame, the jacket consists of a 3-leg or 4-leg structure made of steel pipes interconnected with bracing to provide the required stiffness (2.5.f).
The structure is prefabricated onshore and placed upon a large transport barge to be transported to the installation site, for which minimal seabed preparation is sufficient. Jackets are suitable for waters as far as 60 meters deep and, comparing to monopiles, are sensibly lighter - up to 50% less - resulting in lower costs of transportation and installation.

2.4 Loads and Load Effects

A foundation should be designed to carry static, cyclic and transient loads without excessive deformations or vibrations in sustained structure (API, 2003). Contrary to most onshore foundations, foundations for offshore wind turbines must resist significant static and cyclic horizontal loading and large moments at seabed, in addition to vertical loads (Figure 2.7): in particular, their design must take care of lateral loading generated from both wind and waves.
In this section we define and specify load components and load combinations to be considered in the overall strength analysis for OWTs. As reported by DNV (2010), the loads acting on support structures and foundations may be listed as: permanent loads, variable functional loads, environmental loads and deformation loads. Special attentions should be given to their effects on strength of supporting soils as well as on structural response of the foundation system.
Where not specified, we mainly refer to the standards recommended by the Det Norske Veritas (DNV, 2010).

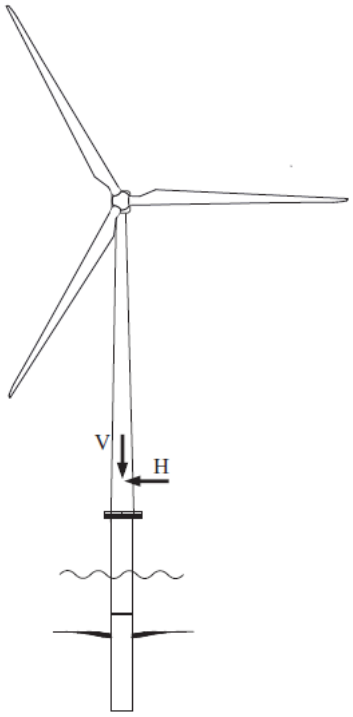

Figure 2.7: Resulting loads on an offshore wind turbine [1].

2.4.1 Permanent loads

Permanent loads do not vary in magnitude, position or direction during the period considered, usually named as passive or *dead* loads (Reese and Van Impe, 2011). Examples are: mass of structure, mass of permanent ballast and equipment, external and internal hydrostatic pressure of a permanent nature, reaction to the above - e.g. articulated tower base reaction.

2.4.2 Variable functional loads

Variable functional loads are time-dependent, since they may vary in magnitude, position and direction during the period under consideration; they are active, or *live*, loads related to operations and normal use of an installation.
For an offshore wind turbine structure, they usually consist of: actuation loads - resulting from the operation and control of the wind turbine; loads on access platforms and internal structures - ladders and platforms; ship impacts from service vessels; crane operational loads. The characteristic value of a variable functional load is the maximum (or minimum) specified value, which produces the most unfavourable load effects in the structure. In addition, they can contribute to fatigue: in this case, characteristic load histories must be well defined and should be included as design parameter.

2.4.3 Environmental loads

Environmental loads are active (*live*) loads related to operations and normal use of a structure. Examples are: wind loads, hydrodynamic loads induced by waves and current - including drag forces and inertia forces - earthquake loads, current-induced loads, tidal effects, marine growth, scour, snow and ice loads.
Environmental loads result to be the most relevant concerning the design of OWT, since they are responsible for lateral and cyclic loading: in particular in this section we will mainly focus on the main features of wind and waves loads.

2.4.3.1 Wind

Specifically for wind turbines, wind-generated loads on the rotor and the tower include wind loads produced directly by the wind, as well as indirect loads that result from the wind-generated motions of the turbine and its operation. Direct loads consist mainly of aerodynamic blade loads and drag forces on tower and nacelle; indirect loads mainly of gravity loads on the rotor blades, centrifugal and Coriolis forces, gyroscopic and braking forces.
Determination of wind-generated loads requires a collection of statistical data on wind velocities from appropriate sources, then translate these velocities into forces on a structure, employing proper shape factors as function of the geometrical element [22]. It is clear that this type of problem includes a certain level of complexity and should be tackled referring to specific domains of study, such as aerodynamics. In this regard, Kallehave (2015)[2] remarks that an offshore wind turbine is typically completed using two models: besides the geotechnics-based model of the support structure, a second model including the turbine and tower structure must be developed.
Nevertheless, a pertinent snapshot of the main wind-related parameters is presented. According to DNV (2010)[13], for normal wind conditions, corresponding to return periods not exceeding 50 years, the mean wind speed U (m/s), with averaging period T (min) at height z (m) above sea level, is determined as follows:

$$U(T,z) = U_{10}(1 + 0.137 \cdot ln\frac{z}{h} - 0.047 \cdot ln\frac{T}{T_{10}}) \tag{2.1}$$

where U_{10} is the 10 minute mean wind speed, $h = 10\ m$ and $T_{10} = 10\ min$.

ASCE (1990)[23] provides specific wind velocity informations for a given geographical area in the United States, while Sachs (1978)[24] obtained data for a 5 minutes period obtained by a cup anemometer. Indicative average speed values for heights of 165 m, 69 m and 13 m are respectively 95 km/h, 80 km/h and 60 km/h.
API (1993) proposes the following formula for a wind-generated force (N):

$$F = \frac{w}{2g} \cdot U^2 C_g A \tag{2.2}$$

where w (N/m^3) is the weight density of air, g (m/s^2) the gravitational acceleration, C_g a shape coefficient - 1.5 for beams, 1 for cylindrical sections - and A (m^2) the area of object.
According to AASHTO (1992)[25], resulting loads applied to bridge structures have values typically comprised between 3.6 kPa and 2.4 kPa.

2.4.3.2 Wave

As studied by Clausen et al. (1975)[26], the first gravity platform in the North Sea was the Ekofisk oil storage tank, installed in June 1973. Here, in addition to a 24 m maximum wave, the foundation had to withstand forces from a large number of other waves in the storm, which may generate excess pore pressure and degrade the soil prior to the impact of the maximum wave.
For offshore structures, the factors to be considered are in fact wave height and period, marine growth and hydrodynamic coefficients for wave forces. As a result, wave statistics are to be used as a basis for representation of wave conditions. As proposed by DNV (2010)[13], a short term 3- or 6-hour sea state, during which stationary conditions prevail, may be represented by a wave spectrum: for example, the power spectral density function of the sea elevation process, $S(f)$, expresses how the energy of the sea elevation is distributed between various frequencies. It can be expressed as function of the significant wave height H_s and the peak period T_p. Appropriate distributions must be accounted in long-term conditions.
Recalling data of storm-induced waves in ocean collected in Australia [22], with a 100 m water depth and a 100-year storm, for a given period, ranging from 5.8 sec and 10.6 sec, H_s varies from 3.6 m to 12 m, and the wave height spectrum is controlled by the Rayleigh equation:

$$P_r(H) = \frac{4H}{H_s^2} e^{-2(\frac{H}{H_s})^2} \tag{2.3}$$

Most pile-supported structures are here considered as slender members, meeting the condition $D/L \leq 0.05$, being D (m) the effective diameter (cylindrical sections) or the width (non-cylindrical) and L (m) the length of design wave. Hence, the resulting forces from non-breaking waves can be computed with the superposition method[17], which identifies as main contributions the drag force and inertia force, represented by the corresponding vector per unit length acting normal to the member axis in the member axis plane p_D and p_M:

$$p = C_D \cdot \frac{\gamma_w}{2g} \cdot D \cdot u|u| + C_M \cdot \frac{\gamma_w}{g} \cdot \frac{D^2\pi}{4} \cdot \frac{\partial u}{\partial t} \tag{2.4}$$

where p (kN/m) is the unitary hydrodynamic force vector normally acting to the member axis, $C_{D/M}$ the drag/inertia coefficient, γ_w (kN/m^3) the unit weight of water, g (m/s^2) the acceleration of gravity, u (m/s) and $\partial u\ \partial t$ (m/s^2) the components normal to the member axis respectively of velocity and acceleration.

2.4.3.3 Other environmental loads

While current effects must be included especially in the design of foundations for bridges [22], the presence of ice plays an important role in all kind of offshore structures: Andersen et al. (1991)[27], analysing typical scenarios of oil and gas production in arctic areas, reported that ice loading can cause cyclic loads on structures placed in the sea, as the breaking of the ice sheets would cause an impulse that would set the bridge piers in motion with a frequency determined by their resonance periods.
AASHTO (1992) suggests a simple equation to compute the horizontal force F (kN) resulting from pressure of moving ice:

$$F = C_n \cdot p \cdot t \cdot w \tag{2.5}$$

where p is the effective ice strength, ranging from 700 kPa to 3 MPa, t (m) the thickness of ice in contact with pier, w (m) the width/diameter, C_n a coefficient accounting for the inclination of nose to vertical - 1.00, 0.75 or 0.50 for an inclination range respectively of 0° to 15°, 15° to 30° or 30° to 45°.

Scour is the result of erosion of soil particles at and near a foundation. It is caused by waves and current and can create important instabilities, as the lack of supporting soil can lead to increased deflections and bending moments. While the informal approach in offshore structures design is to assume a 1.5-to-2 m minimum amount of erosion, a more complex and proper system for scour prediction must be applied, especially when dealing with cohesionless soils.

2.4.4 Deformation loads

Deformation loads are due to inflicted deformations such as temperature loads, built-in deformations and settlement of foundations. In particular, extreme sea/air temperature gradients must be accounted in the design, as well as the contribution of solar radiation - an intensity of 1000 W/m^2 is usually considered.

2.5 Conclusions

The expansion of the offshore wind energy industry is resulting in the increasing number of technological solutions in terms of substructures; nonetheless, monopiles still represents the most popular solution.
A correct evaluation of the dynamics of the overall structure - substructure and upper structure - starts with an accurate evaluation of load and load effects acting on the system. When dealing with offshore turbines, the analysis has especially to take into account additional effects related to the environment, such as wind and wave.

Chapter 3

Design of Foundations for Offshore Wind Turbines

3.1 Introduction

As stated by DNV (2010, p.18)[13],

> Structures and structural elements shall be designed to: sustain loads liable to occur during all temporary, operating and damaged conditions if required; ensure acceptable safety of structure during the design life of the structure; maintain acceptable safety for personnel and environment; have adequate durability against deterioration during the design life of the structure.

In this standard, structural safety must be ensured by use of a safety class methodology. Based on the failure consequence, the structure to be designed is classified into a safety class, which is reflected in different requirements to load factors.
For structures in offshore wind farms, considering different levels of risk in matter of personal injuries, human life, pollution and economical consequences, three safety classes are defined: low (LSC), normal (NSC) and high safety classes (HSC). Support structures and foundations for wind turbines, which are normally unmanned, are usually to be designed to the normal safety class ([13], guidance note, p 18): in this case, failures of the structure imply some risk for personal injuries, pollution or minor societal losses, or possibly significant economic consequences.
In addition, for each class, a target safety level is defined in terms of a nominal annual probability of failure: in our case of study - foundation of OWT, NSC - a nominal annual probability of failure of 10^{-4} is considered.

Specific criteria have been developed in order to provide a robust methodology for the design of these structures. Nonetheless, the principles are to be found in the theory of the limit states and in specific design approaches, valuable and applied in several domains of engineering.

3.2 Design Principles

3.2.1 Limit states

A limit state is a condition beyond which a structure or structural component will no longer satisfy the design requirements (DNV, 2010). We distinguish:

- Ultimate limit states (ULS), corresponding to the maximum loadcarrying resistance;
- Fatigue limit states (FLS), corresponding to failure due to the effect of cyclic loading;
- Accidental limit state (ALS), corresponding to damage to components due to an accidental event or operational failure;

- Serviceability limit states (SLS), correspond to tolerance criteria applicable to normal use.

3.2.2 Partial Safety Factor Method

According to this design method, the safety level of a structure or a structural component is considered to be satisfactory when the design load effect S_d - typically stresses, deformations, displacements - does not exceed the design resistance R_d. Hence, the design inequality criterion is written as:

$$S_d \leq R_d \tag{3.1}$$

As remarked in the Eurocode 7 [28], here the safety criterion is based on a semi-probabilistic concept: the parameters used are considered as stochastic variables and the design value is determined by the combination of a characteristic value and a partial safety factor.
In case of support structures and foundations, where load effects in the tower are usually applied as a boundary condition, the design load effect S_{di} is obtained from a structural analysis for the design load F_{di}, which is obtained by multiplication of the characteristic load F_{ki} by a specified load factor γ_{fi}:

$$S_{di} = \gamma_{fi} \cdot F_{ki} \tag{3.2}$$

This approach is especially suitable when a proper representation of non-linear material behaviour is the prime concern, e.g. the soil interacting with a foundation.
The design load effect S_d is defined as the most unfavourable combined load effect resulting from the simultaneous occurrence of n loads F_i, $i = 1, ...n$, and can be express as summation of each design load effect corresponding to the characteristic load:

$$S_d = \sum_{i=1}^{n} S_{di}(F_{ki}) \tag{3.3}$$

When a linear relationship exists between the load F_i and its associated load effect S_i,

$$S_d = \sum_{i=1}^{n} \gamma_{fi} S_{ki} \qquad (a), \qquad\qquad S_k = \sum_{i=1}^{n} S_{ki} \qquad (b) \tag{3.4}$$

where S_k is the characteristic combined load effect.
A characteristic value of a variable is defined as its principle representative value. In this standard, design in the ULS is either based on a characteristic combined load effect S_k defined as the 98% quantile in the distribution of the annual maximum combined load effect, or on a characteristic load F_k defined as the 98% quantile in the distribution of the annual maximum of the combined load. The result is a combined load or a combined load effect whose return period is 50 years.
This is valuable for all the geotechnical parameters, whose definition in case of gaussian distribution is given in Figure 3.1. Note that here the threshold is fixed at 5%.
In addition to imperfections in the modelling, a partial safety coefficient covers the unfavourable deviation with respect to the characteristic values. For the operational design conditions, the basis for selection of characteristic loads and load effects specified in Table 3.1.

The resistance R against a particular load effect S is, in general, a function of parameters such as geometry, material properties, environment, and load effects themselves, the latter through interaction effects such as degradation.
The design resistance R_d can be obtained either by dividing the characteristic resistance R_k by a specified material factor γ_m (eq. 3.5.a) or from the design material strength σ_d by a capacity analysis (eq. 3.5.b). As mentioned, characteristic resistance R_k and material strength σ_k are obtained as a specific quantile in the corresponding probability distribution or by testing.

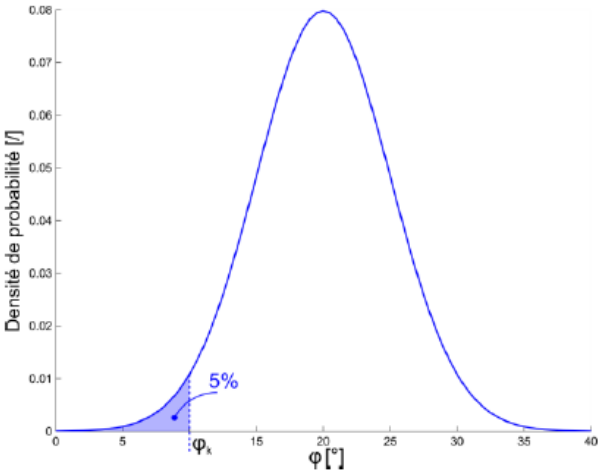

Figure 3.1: Example of definition of characteristic value for a gaussian distributed geotechnical parameter [9].

	Limit states – operational design conditions		
Load category	ULS	FSL	SLS
Permanent (G)	Expected value		
Variable (Q)	Specified value		
Environmental (E)	98% quantile in distribution of annual maximum load or load effect (Load or load effect with return period 50 years)	Expected load history or expected load effect history	Specified value
Abnormal wind turbine loads	Specified value		
Deformation (D)	Expected extreme value		

Table 3.1: selection of characteristic loads and load effects [13].

$$R_d = \frac{R_k}{\gamma_m} \qquad (a), \qquad\qquad R_d = R\left(\sigma_d = \frac{\sigma_k}{\gamma_m}\right) \qquad (b) \tag{3.5}$$

where in equation 3.5.b we assume the functional relationship between material strength and resistance.

3.3 Design of Monopiles

This section aims to introduce important features of monopile foundations design, based on soil behaviour and its interaction with the structure. We provide some general rules and characterization criteria, which can be eventually adapted for more complex support systems.
Pile foundations are subjected to simultaneous axial and lateral loading and, in current practice, they are independently analysed to determine first their bearing capacity and settlement and then the lateral stresses and deflections [29]. In the design, specific geometrical and geotechnical parameters must be taken under consideration: diameter, penetration, wall thickness, spacing, geometry, location, mud line restraint, material strength, installation method and many others. While different analysis methods may be utilized to determine the requirements of a foundation, at a minimum the chosen procedure should properly simulate the non-linear response behaviour of the soil and assure load-deflection compatibility between the structure and the pile-soil system [11].

3.3.1 Axial Capacity

Axial resistance in soils is provided by a combination of axial soil-pile adhesion or load transfer along the sides of the pile and end bearing resistance at the pile tip [12, 32].

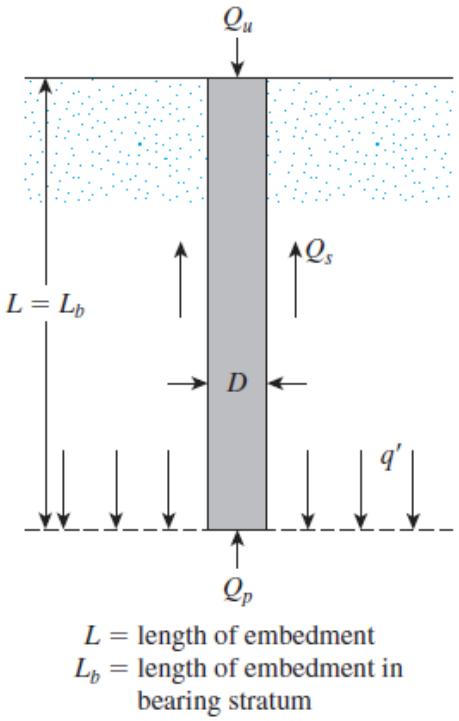

Figure 3.2: Ultimate load-carrying capacity of pile ([32].

In particular, as showed in Figure 3.2, the ultimate bearing capacity of piles under axial loads Q_u (kN) should be determined as sum of the skin friction resistance Q_f (kN) and the total end bearing Q_p (kN):

$$Q_u = Q_f + Q_p = f \cdot A_s + q \cdot A_p \tag{3.6}$$

where f (kPa) is the unit skin (or shaft) friction capacity - acting both inside and outside of the pile - A_s (m^2) the side surface area and A_p (m^2) the gross end area of pile, q (kPa) the unit end bearing capacity.
We remark that equation 3.6 assumes that the maximum skin friction along the pile and the maximum

and bearing are mobilized simultaneously. However, the ultimate skin friction increments along the pile are not necessarily directly additive, nor is the ultimate end bearing necessarily additive to the ultimate skin friction. As a result, in some cases a more explicit consideration of axial pile performance effects on pile capacity may be required.
According to Braja M. Das (2011 [32]), Terzaghi's equations for shallow foundations can be adapted to (deep) piles. Therefore, the unit end bearing capacity can be defined as:

$$q = cN_c + q'N_q \tag{3.7}$$

where we assume the width D (m^2) relatively small, c (kPa) the cohesion, q' (kPa) the effective vertical stress at the level of the pile tip and N_c, N_q bearing capacity factors.
Other similar methods can be used for the estimation of the point bearing capacity q_p, Meyerhof (1976)[33] and Vesic (1977)[34] in particular, either for sand and clay. However, Braja M. Das (2011) remarks that, in the field, for full mobilization of the point resistance Q_p the pile tip must go through a displacement of 10 to 25% of the pile width.
Once defined the ultimate capacity, a reasonable factor of safety should be used to obtain the total allowable load:

$$Q_{all} = Q_d/FS \tag{3.8}$$

For offshore foundations, the estimation of point and frictional resistance is usually based on specific guidelines, such as API (2003) and DNV (2014) standards for clay and sand, here presented.

3.3.1.1 Cohesive Soils

For pipe piles in cohesive soils, the shaft friction f (kPa) at any point along the pile may be calculated, with the total stress method, as function of the undrained shear strength of the soil c (kPa) at the point in question:

$$f = \alpha c \tag{3.9}$$

where the dimensionless factor α ($\leqslant 1$, f should not exceed c) depends on the ratio $\psi = c/p'_0$, where p'_0 (kPa) is the effective overburden pressure at the point in question. In particular,

$$\begin{cases} \alpha = 0.5\psi^{-0.5}, & \psi \leqslant 1 \\ \alpha = 0.5\psi^{-0.25}, & \psi > 1 \end{cases} \tag{3.10}$$

In practice, as proposed by API (2003, commentary 6.4, pp 188,199)[11], for different types of clays the value of f should be chosen in function of eventual plasticity, level of consolidation and application, not exceeding c, for which reference values are 24-48-72 kPa. DNV (2014) includes an additional effective stress-based method, as well as a semi-empirical one. The unit end bearing capacity can be computed as 9 times the cohesion (N_c=9, N_q=0 in equation 3.7).

3.3.1.2 Cohesionless Soils

For pipe piles in cohesionless soils,

$$f = Kp'_0 \tan\delta \leq f_l, \qquad q = p'_0 N_q \leq q_l \tag{3.11}$$

where K is the coefficient of lateral earth pressure, 0.8 (1.0) for open-ended (closed-ended) piles, p'_0 (kPa) is the effective overburden pressure, δ the friction angle between soil and pile wall, N_q ($8 \div 50$) the bearing capacity factor, f_l and q_l limiting values. Further indications concerning typical values can be found in the indicated section of API (2003) as well as in appendix F of DNV (2014).

3.3.1.3 Soil reaction: *t-z curves*

As a general constraint, deflections in axially loaded-piles - either for static and cyclic loads - should be within acceptable serviceability limits and compatible with the structural forces and movements. According to common standards, for deformation and stress analysis, a pile can be modelled as a number of consecutive column elements, supported at nodes by non-linear springs. These springs define - or are defined as - *t-z curves* and represent the axial load-displacement relationship between pile and soil. The stress t is the unitary (per area of pile surface) axial skin friction mobilized by a certain z, the relative axial displacement.
An analytical expression for these curves is proposed, where z and t are related to the maximum skin resistance, the pile radius, the initial shear modulus of the soil and some fitting parameters. This expression results from a curve fitting process; in fact, API (2003) prefers to propose normalized curves where the discretization to apply is presented, for both cohesive and cohesionless soils (Figure 3.3).
In the next section we will remark that this approach is suggested also for the soil lateral reaction (*p-y curves*).

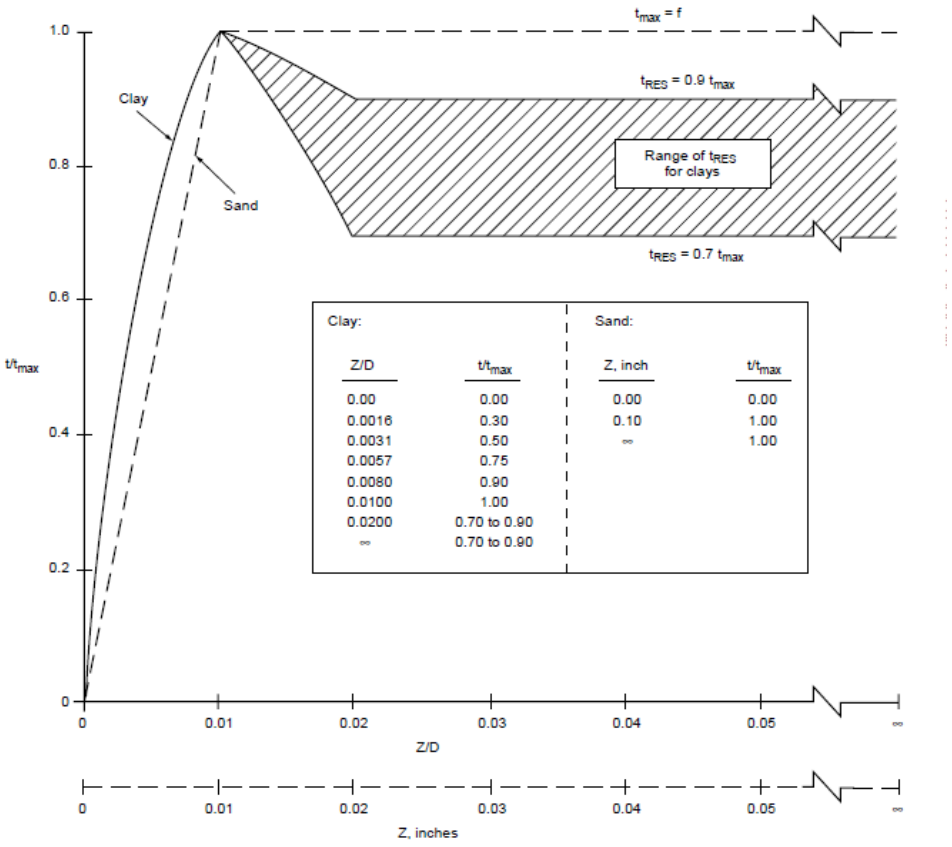

Figure 3.3: Recommended normalized *t-z curves* for non-carbonate soils, where z is the local pile deflection, D the pile diameter, t (kPa) the mobilized soil pile adhesion, t_{max} the maximum soil pile adhesion (or unit skin friction) capacity [11].

Similarly, we can define the *Q-z curve*, the relationship between the mobilized end bearing resistance and axial tip deflection (Figure 3.4). As mentioned, the mobilization of the full end bearing resistance may require large pile tip movement, up to 10% of the diameter.

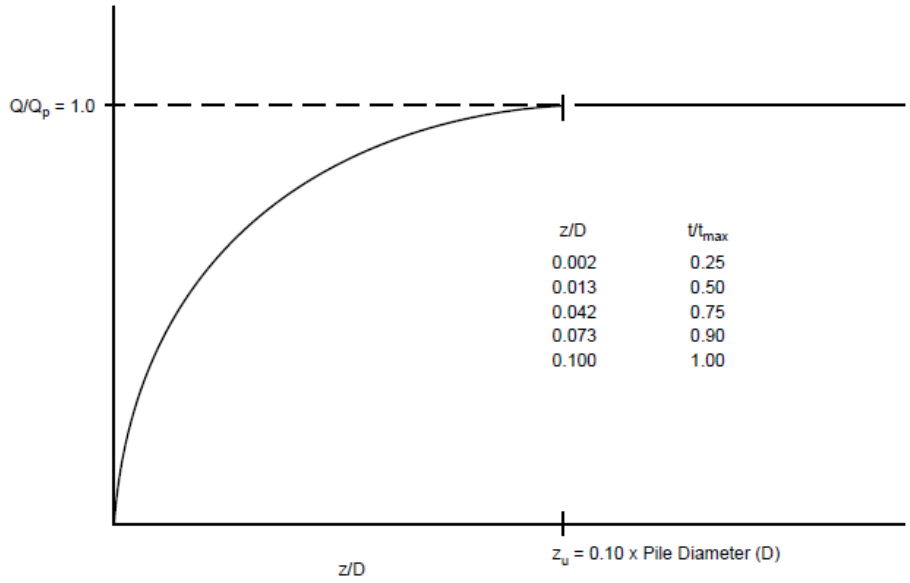

Figure 3.4: Recommended *Q-z curves* for clays and sands, where Q, Q_p (kN) are respectively the mobilized and the total end bearing capacity [11].

3.3.2 Lateral Capacity

The design should consider lateral loads, whether static or cyclic: when subjected to horizontal forces, pile foundations resist by bending, while still supporting the vertical load transmitted by the superstructure. Their mechanical behaviour is such that they resist a lateral load by mobilizing passive pressure in the surrounding soil; the distribution of soil's reaction depends on the stiffness of both pile and soil, as well as on the fixity of the ends of the pile (Figure 3.5).
The typical nature of variation of pile deflection, moment and shear force are showed in Figure 3.6, considering simple cases of rigid/short and elastic/long piles: they are obtained by applying the governing differential equations for the laterally loaded pile problem.
The soil-structure interaction is such that soil reaction depends on pile movement, and the pile movement depends on soil reaction: the solution must satisfy a non-linear differential equation as well as equilibrium and compatibility conditions [35]. With reference to Figure 3.7 and DNV (2014), we obtain:

$$EI\frac{d^4y}{dx^4} + Q_A\frac{d^2y}{dx^2} - p(x) + q = 0 \tag{3.12}$$

with

$$EI\frac{d^3y}{dx^3} + Q_A\frac{dy}{dx} = Q_L\ , \qquad EI\frac{d^2y}{dx^2} = M \tag{3.13}$$

where $p(x)$ (kPa) is the resultant soil resistance force per unit length of pile that occurs when a lateral displacement y (pile-soil deformation, m) occurs into the soil; EI (MN×m^2) is the flexural rigidity of pile (material elastic modulus, MPa, × pile cross section moment of inertia of respect neutral axis, m^4); Q_A, Q_L, M respectively the axial force, the lateral shear force (kN) and the bending moment (kN×m) in the pile; p (kPa) is a distributed load along the pile.

The p-y relationship is non-linear and also varies with depth x: hence, in practice, it is common to solve differential equation 3.12 using numerical methods, typically finite difference or finite element method (FDM, FEM), and by modelling the soil reaction using non-linear *p-y curves*.

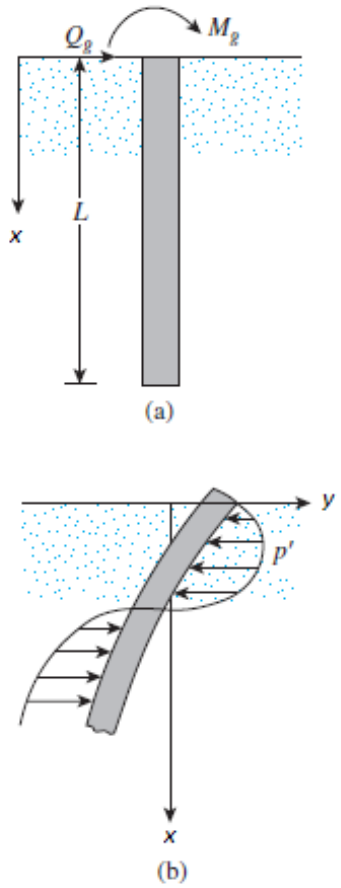

Figure 3.5: (a) Laterally loaded pile; (b) soil resistance on pile caused by lateral load (modified from [32]).

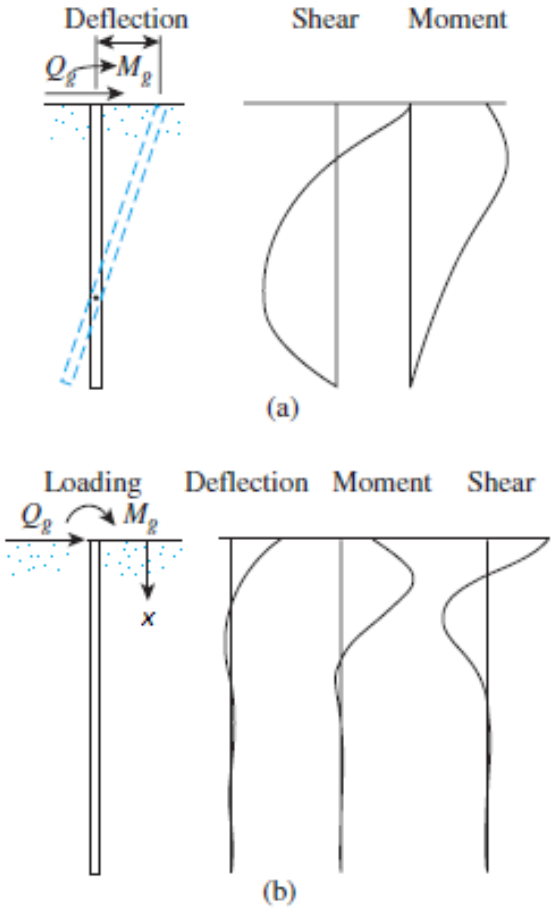

Figure 3.6: Nature of variation of pile deflection, moment, and shear force for (a) a rigid pile and (b) and elastic pile (modified from [32]).

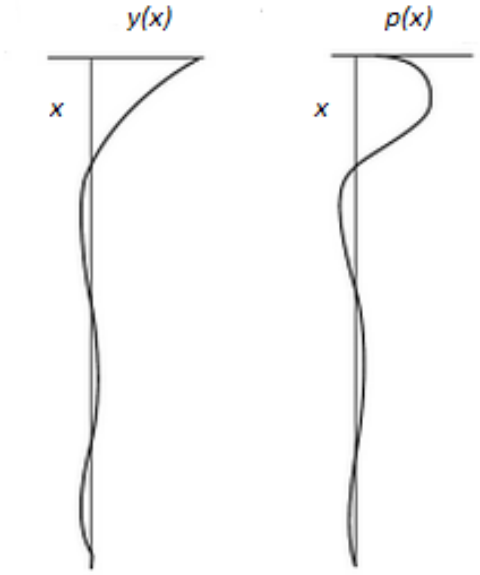

Figure 3.7: Soil-pile deflection (y) and soil resistance (p) in function of depth (x) (modified from [22]).

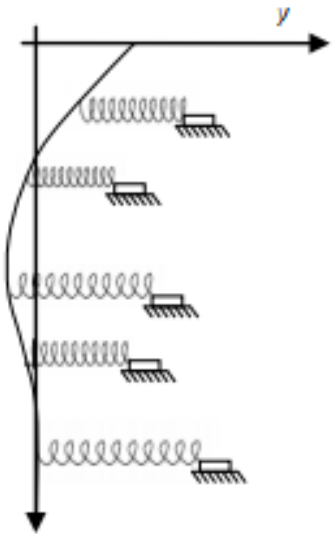

Figure 3.8: Independent non-linear springs applied at nodal points [10].

3.3.2.1 Soil under static loading

The soil reaction can be modelled as a series of independent non-linear springs: the *p-y curves* represent the non-linear behaviour of the soil by relating the soil reaction and pile deflection at points along the pile length. As a result, the pile is modelled as a number of consecutive beam-column elements, each supported by springs applied at nodal points (Figure 3.8).
The distribution of stresses against a cylindrical pile before and after a lateral deflection is showed in Figure 3.9, as proposed by Reese and Van Impe (2011)[22]: assuming the pile installed vertically and without inducing bending, at a certain depth the stresses are uniform and normal to the pile wall; as the pile deflects - once a lateral load p_t is applied - some of the stresses are not perpendicular to the wall due to development of shear stresses at the soil-pile interface. The net soil reaction p_1, obtained by integration of stresses around the pile cross section, is directed opposite to the displacement y_1. Along this direction, the components normal and tangent to the pile section represent respectively a passive/active lateral resistance and a friction action. In other words, the mode of shearing of a soil element depends on its location, e.g. in Figure 3.10 the loading on Soil Element A is similar to triaxial compression, whereas Elements B and C are loaded similar to direct simple shear condition [30, 31].

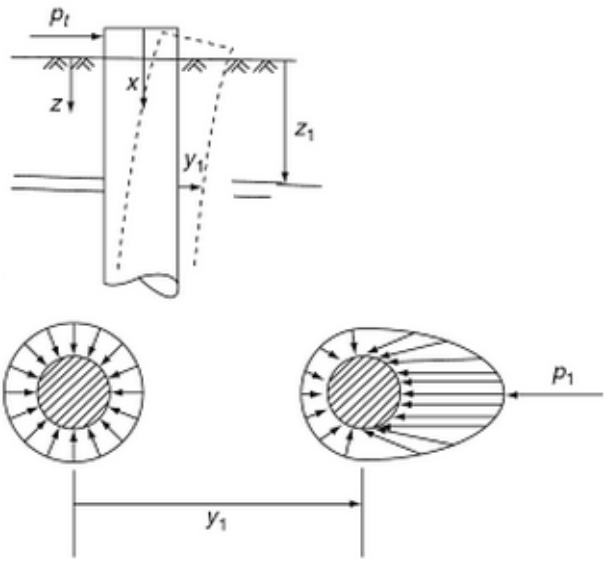

Figure 3.9: Soil-pile deflection (y) and soil resistance (p) in function of depth (x) (modified from [22]).

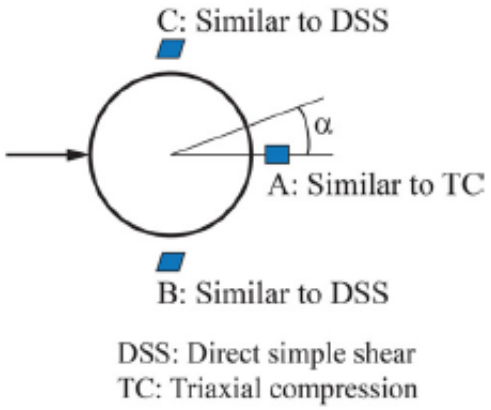

Figure 3.10: Mode of shearing of soil elements under lateral loading [30].

The *p-y curves*

A typical non-linear *p-y curves* for a short-term monotonic loading is showed in Figure 3.11a. From point a to b the resistance increases at a decreasing rate with increasing deflection: many suggestions have been made for predicting this portion of curve, but there is no widely accepted analytical procedure. The straight-line portion after b implies a plastic behaviour of in situ soil, with no loss of resistance for higher values of deflection: hence the ultimate resistance p_{ult} can be determined with analytical models as function of pile geometry and soil properties. The *p-y* relationship at any point is given by the soil modulus E_{py}, representing the slope of the *p-y curve* (Figure 3.11b): this slope is constant for small deflections and particular depth and decreases with increasing deflections. The modulus is related to the Young modulus, but is function of the pile-soil interaction, rather than only of soil properties.

A proper characterization of the curve for small displacements - around the point a - is still a main goal for designers. In fact, as remarked by Kallehave (2015), an accurate evaluation of the pile-soil stiffness would allow a better prediction of turbines fundamental frequency, which governs the performance of dynamically loaded structures. Hence, the focus here is on a serviceability problem

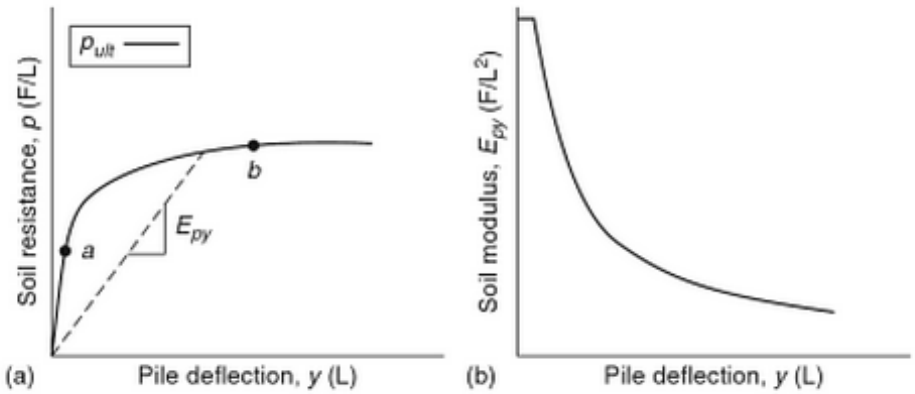

Figure 3.11: Typical *p-y* curve (a) and resulting soil modulus (b) for short-term monotonic loading RVI.

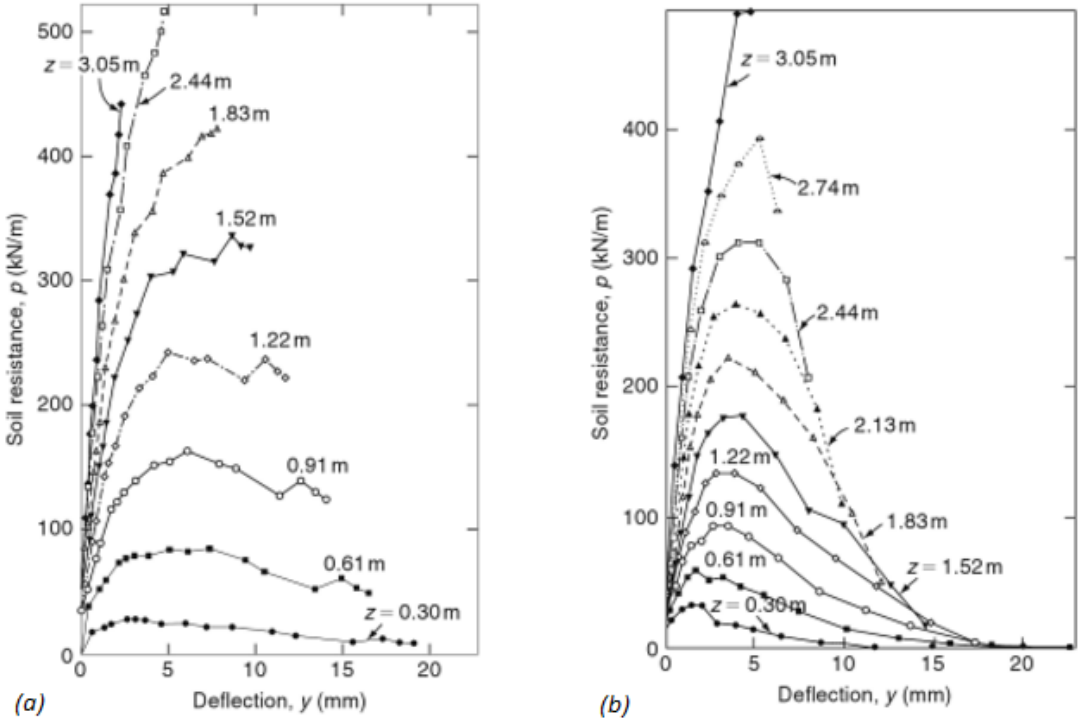

Figure 3.12: *p-y* curves of 641 mm-diameter pile developed from static load tests (a) and from cyclic load test [38].

(SLS), rather than on a failure problem related to ultimate limit states (ULS). Wind energy plants are relatively sensitive to deformations, in particular tilting: to make economic use of offshore wind energy possible, foundation structures with minimum costs, but sufficient stiffness have to be designed, Achmus reports [39].
In the curves of Figure 3.12a, resulting from static loading tests, the influence of depth is evident: for increasing value of depth, the initial stiffness of *p-y curves* increases and the ultimate resistance decreases.

API *p-y curves*

The procedure recommended by the official standards - API and DNV [11, 12] - for constructing the ultimate lateral bearing capacity curves in case of static lateral loads for clays is now presented. The ultimate unit lateral bearing capacity of clay p_u[1] (kPa) can be expressed as follows:

$$\begin{cases} p_u = 3S_u + \left(\gamma + \dfrac{JS_u}{D}\right) X, & 0 < X < X_R \\ p_u = 9S_u, & X \geq X_R \end{cases} \tag{3.14}$$

$$X_R = \frac{6DS_u}{\gamma D + S_u J} \tag{3.15}$$

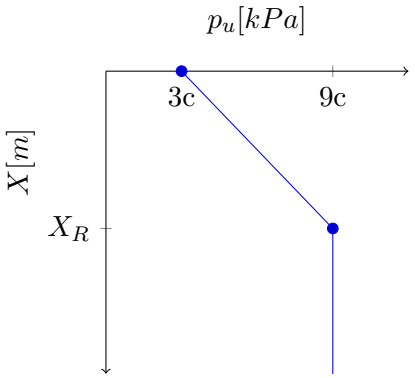

Figure 3.13: Ultimate lateral bearing capacity for clay [11, 12].

where S_u (kPa) is the undrained shear strength for undisturbed clay soil samples, γ' the effective unit weight of soil (MN/m^3), J (0.25÷0.5, 0.5 for soft normally consolidated clay) the dimensionless empirical constant determined by field testing, X (m) the depth below soil surface and X_R (m) the depth below soil surface to bottom of reduced resistance zone, defining the transition point from linear to plastic behaviour, in fact obtained by equalling the two contributions (equation 3.15).

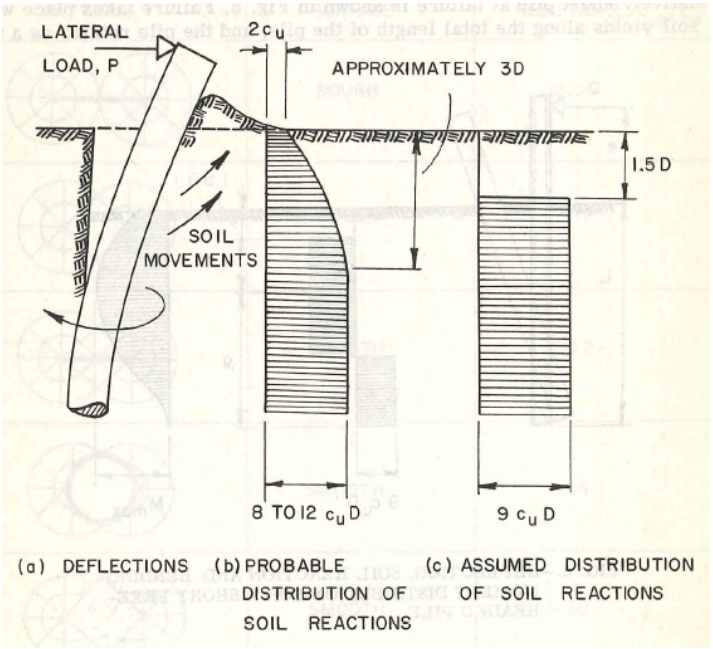

Figure 3.14: Lateral earth pressures along a laterally loaded free-headed pile driven in a cohesive soil - c_u, or S_u, is the undrained shear strength [40].

One of the first justification for such a distribution of p_u can be found in Broms (1964)[40], resumed in Figure 3.14, presenting the failure mechanism and the resulting lateral earth pressures along a laterally loaded free-headed pile driven in a cohesive soil. Note that, close to the ground surface, the

[1]Certain versions of the norms refer to p_u and p as the (ultimate) lateral pressure/resistance, expressed in kN/m, resulting from the integration of the unit value - typically along a pile diameter; later in the paper we will mainly make use of this notation.

soil located in front of the pile tends to move upwards, while the portion at the back side separates from the structure; at some depth, the soil all around the section moves laterally. A probable soil reaction distribution has been theorised, with an initial value of $2S_uD$, decreasing to 8 to $12S_uD$; then this shape has been approximated by a rectangular distribution with constant $9S_uD$ value after a certain depth.

For piles in cohesionless soils:

$$\begin{cases} p_u = (C_1X + C_2D)\gamma' X, & 0 < X < X_R \\ p_u = C_3D\gamma' X, & X \geq X_R \end{cases} \tag{3.16}$$

where C_1, C_2 and C_3 are coefficients depending on the internal friction angle ϕ' as shown in Figure 3.15(a) - X, X_R, γ' and D as previously defined.

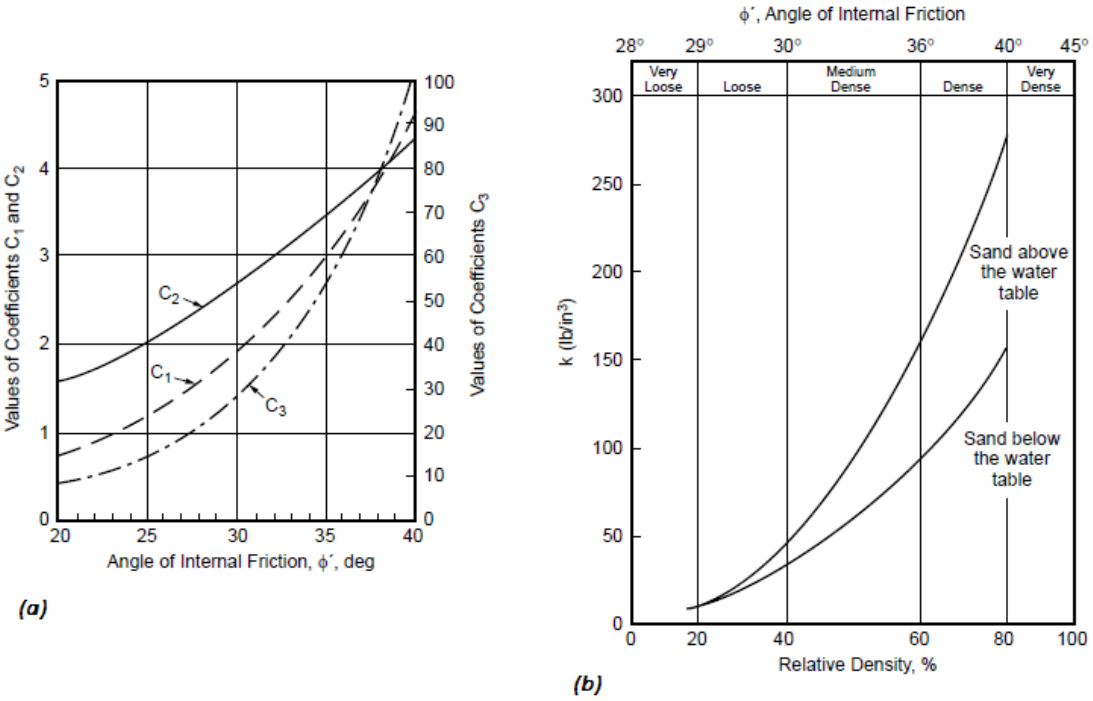

Figure 3.15: Coefficients (a) and initial modulus of subgrade reaction k (b) as function of friction angle os sand [11, 12].

The p-y curve for clays on static loading, being p (kPa) the mobilized unit lateral pressure [1], can be generated according to:

$$\begin{cases} p = \dfrac{p_u}{2}\left(\dfrac{y}{y_c}\right)^{1/3}, & y \leq 8y_c \\ p = p_u, & y > 8y_c \end{cases} \tag{3.17}$$

where $y_c = 2.5\epsilon_{50}D$ (m), in which D (m) is the pile diameter and ϵ_c the strain which occurs at one-half the maximum stress in laboratory undrained compression tests of undisturbed soil samples, equal to S_u/E - E the Young's modulus (MPa). The 1/3-exponential provides the typical decreasing-slope shape of the p-y curve, while for excessive displacements the pressure reaches the value of ultimate resistance.
Similarly to *t-z* soil reaction curves in paragraph 3.3.1.3, equation 3.17 results from a fitting process provided by Matlock (1970)[42] and does not lie on specific physical assumption - the initial stiffness would be infinite, being the expression not derivable in zero. Therefore, API (2003) suggests a family of discretized *p-y curve* (Figure 3.16): note than the stiffness increases along with the ultimate resistance - typically in depth. In addition, only two points corresponding to a displacement lower than y_c are

given - in other versions not even these two; it can be shown that this is a conservative choice with respect to equation 3.17 - a visual comparison is presented in the next paragraph. Nevertheless, a better definition of this area of the curve is required: in fact, an excessive underestimation of the stiffness for low displacements may lead to overdesigned structures and wrong predictions of SLS dynamics of turbines.

$\mathbf{p/p}_u$	$\mathbf{y/y}_c$
0.00	0.0
0.23	0.1
0.33	0.3
0.5	1.0
0.72	3.0
1.00	8.0
1.00	∞

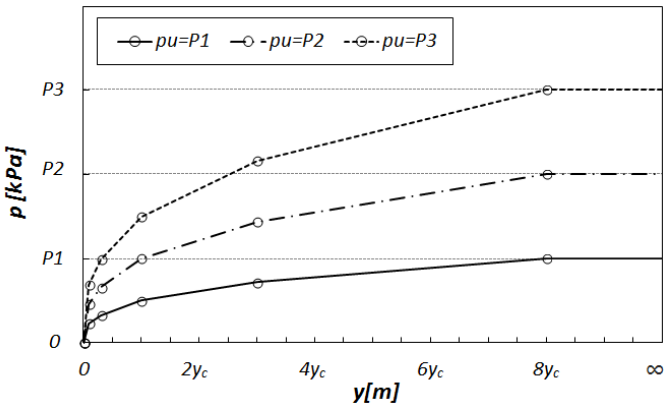

Figure 3.16: Discretized *p-y curve* formula for clays under short-term static loading [11] and corresponding graph different values of ultimate resistance - typically increasing in depth as in Figure 3.13.

For sands on static loading, the *p-y curve* can be generated according to:

$$p = Ap_u tanh\left(\frac{kX}{Ap_u}y\right), \qquad A = \left(3 - 0.8\frac{X}{D}\right) \geq 0.9 \tag{3.18}$$

where A is a factor accounting for static loading conditions and k (kN/m^3) is the initial modulus of subgrade reaction, depending on the internal friction angle ϕ' as shown in Figure 3.15(b) - X, y and D as previously defined. The hyperbolic tangent provides the typical decreasing-slope shape of the *p-y curves*, down to a residual value of resistance which decreases in depth.

Jeanjean (2009) *p-y curves*

As reported by Gilbert (2015)[41], Jeanjean (2009) believed that the *p-y curves* recommended by API (2003) and Matlock (1970) underestimated the lateral soil resistance on offshore oil well conductors. He modeled conductors as vertical steel pipes, so the results of his study are considered equally valid for laterally loaded piles.
In particular he carried out lateral load tests on model piles in a centrifuge to re-assess the *p-y curves* for soft clays. Two changes to the API-Matlock (1970) curves were proposed: first, the range of the lateral bearing capacity factor (N_p) and its variation versus depth were modified as follows:

$$\begin{cases} p_u = N_p S_u \\ N_p = 12 - 4e^{-\varepsilon z/D} \end{cases} \qquad \varepsilon = \begin{cases} 0.25 + 0.05\lambda & \lambda < 6 \\ 0.55 & \lambda \geq 6 \end{cases} \qquad \lambda = \frac{S_{u0}}{S_{u1}D} \tag{3.19}$$

where S_{u0} is the undrained shear strength at the mud line, S_{u1} the rate of increase of undrained shear strength with depth, D the pile diameter and z the depth of interest. The curve is reported in Figure 3.17: note that it is similar to the probable distribution theorised by Broms (1964) (Figure 3.14) and the ultimate pressure exceeds the value of $9S_u$ given by API/Matlock.

Secondly, the shape of the *p-y curves* was changed to a hyperbolic form, as follows:

$$p = p_u tanh\left[\frac{G_{max}}{100S_u}\left(\frac{y}{D}\right)^{0.5}\right] \tag{3.20}$$

where G_{max} is the maximum shear modulus. It depends on the overconsolidation ratio and the index of plasticity; for soft clay with ε_{50}=1% Gilbert (2015) suggests the use of G_{max}/S_u varying between 400 and 550.

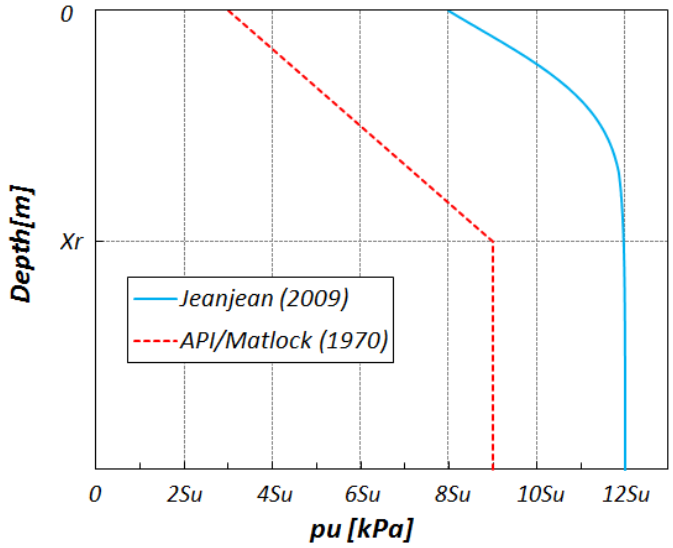

Figure 3.17: Variation in depth of ultimate lateral soil pressure after API/Matlock (1970) and Jeanjean (2009) - here undrained strength constant in depth.

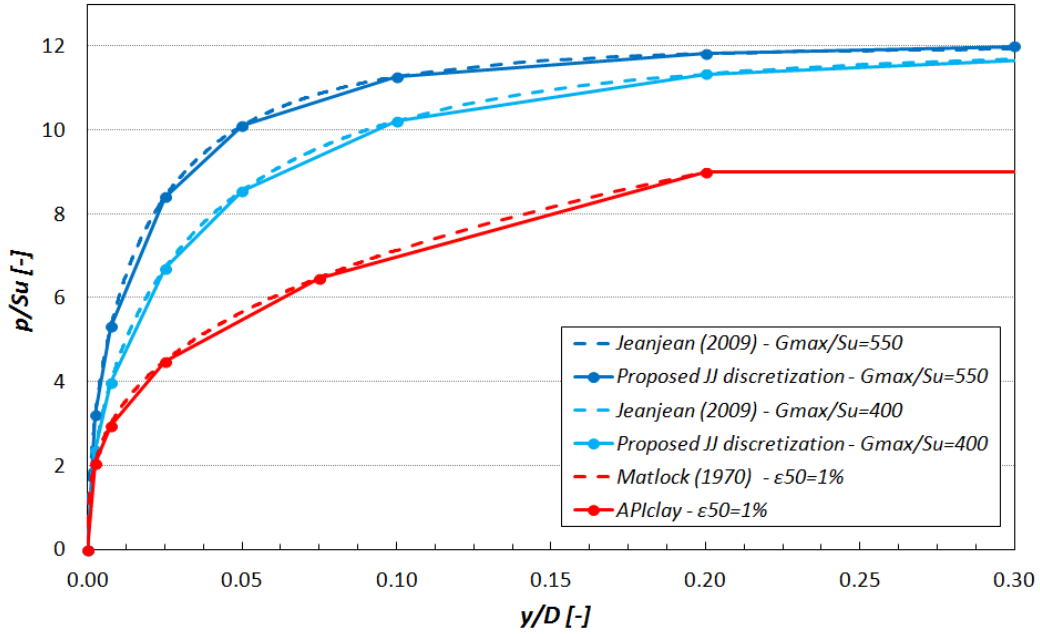

Figure 3.18: Normalized p-y curves after API, Matlock (1970), Jeanjean (2009) - full form and proposed discretization. Here ultimate pressure at $9S_u$ for API/Matlock, $12S_u$ for Jeanjean.

(a)

p/p_u	y/D
0.00	0.0
0.27	0.0025
0.44	0.0075
0.70	0.025
0.84	0.05
0.94	0.1
0.99	0.2
1.00	0.3
1.00	∞

(b)

p/p_u	y/D
0.00	0.0
0.20	0.0025
0.33	0.0075
0.56	0.025
0.71	0.05
0.85	0.1
0.95	0.2
1.00	0.4
1.00	∞

Table 3.2: Proposed discretization for normalized Jeanjean (2009) p-y curves - G_{max}/S_u equal to 550 (a) or 400 (b).

A comparison with the API/Matclock formulation in terms of normalized curve is reported in Figure 3.18: note that Jeanjean (2009) assumes a stiffer response of the soil, especially at low displacements. Nonetheless, the analytical formula proposed contains an exponential functions, then it is not derivable in zero: therefore, taking inspiration from the discretized API formula, we propose two discretized forms of Jeanjean (2009) (Table 3.2), one for a given G_{max}-on-S_u ratio. Its *role* is mainly related to numerical reasons: in fact it will be used in the 1D modelling, as we believe it provides a more stable solution.

3.3.2.2 Soil under cyclic loading

It is now interesting to analyse how the models proposed change considering cyclic loading scenarios. API (2003) remarks that repetitive loadings can cause a temporary or permanent decrease in load-carrying resistance, and/or an accumulation of deformation, commonly defined as fatigue. A comparison between Figures 3.12a and 3.12b of paragraph 3.3.2.1 demonstrates the influence of cyclic loads: at low magnitudes of deflection, the initial stiffnesses are only moderately affected, while at large magnitudes, the resistance values decrease considerably, as well as p_{ult}.
Similarly to the static load case for clays, the standards recommend equation 3.21 and 3.22 respectively for deep ($X > X_R$) and shallow ($X \leq X_R$) portions of soil. The corresponding discretized normalized curves are showed in Table 3.3.

$$\begin{cases} p = \frac{p_u}{2}\left(\frac{y}{y_c}\right)^{1/3}, & y \leq 3y_c \\ p = 0.72p_u, & y > 3y_c \end{cases} \tag{3.21}$$

$$\begin{cases} p = \frac{p_u}{2}\left(\frac{y}{y_c}\right)^{1/3}, & y \leq 3y_c \\ p = 0.72p_u\left(1 - \left(1 - \frac{X}{X_R}\right)\frac{y - 3y_c}{12y_c}\right), & 3y_c < y \leq 15y_c \\ p = 0.72p_u, & y > 15y_c \end{cases} \tag{3.22}$$

$(a)\ X < X_R$	
$\mathbf{p/p}_u$	$\mathbf{y/y}_c$
0.00	0.0
0.50	0.1
0.72	3.0
$0.72\frac{X}{X_R}$	15.0
$0.72\frac{X}{X_R}$	∞

$(b)\ X > X_R$	
$\mathbf{p/p}_u$	$\mathbf{y/y}_c$
0.00	0.0
0.50	0.1
0.72	3.0
0.72	∞

Table 3.3: Discretized normalized *p-y curves* for clays under cyclic loading, at shallow (a) and large depth (b) [11].

As mentioned, the effects of fatigue are such that the value of the ultimate lateral bearing capacity previously defined (equation 3.14) is never reached. In addition, the stiffness suddenly drops to zero for a much lower displacement ($3y_c$); afterwards, the plasticity is maintained only at certain depths, whereas at shallow depths a softening behaviour is assumed, followed by a plastic zone where the residual resistance decreases down to a null value in surface.

For sands, in equation 3.18 a value of $A = 0.9$ accounts for cycling loading conditions. As for clays, this results in an attenuation of the resistance properties, by lowering the impact of p_u.

3.4 Conclusions

The design of monopiles must be based on an accurate evaluation of both axial and lateral capacity, as well as accounting for different types of soil in different conditions of the structure.
As far as the characterization of the soil lateral reaction in concerned, a different approach must be adopted in case of cyclic or monotonic loads. For these lasts, the API standards proposes a family of *p-y curves* which is well established as a reference in the domain; nonetheless, as it has been established that this formulation does not provide accurate predictions, many studies have been conducted in order to improve the curves. In particular, Jeanjean (2009) proposes a different formula for soft clays, based on the ratio between the maximum shear modulus and the undrained shear strength.

Chapter 4

1D Finite Element Analysis

4.1 Introduction

In the previous chapters we have highlighted the main features of the existing design methods for monopiles, especially under lateral loading. In addition, we have remarked how the laws which currently characterize the soil-structure interaction require an improvement: this problem is typically tackled by means of 3D models and field measurements. Parallel to this, 1D models are typically realised: once calibrated, they provide an easy way to apply a given design method. As a result, in 1D analysis the selection of adequate characteristic laws, such as the *p-y curves*, is the most crucial problem [22].
While in the next chapter we will present a 3D finite elements analysis, now the focus is on a 1D finite elements *Python* code for a monopile under monotonic lateral loads: it has been realised during an internship at Cathie Associates[6], under the supervision of the Project Engineer Hendrik Versteele. At first, the lateral reaction of the soil has been implemented according to a standard uncoupled non-linear springs formulation, with the pile modelled as an Euler-Bernoulli beam. Secondly, additional functions have been tested, useful especially for short-large piles: in fact, recent studies suggest that these structures require an higher level of complexity in the modelling, resulting, at least, in the use of a Timoshenko beam and additional resistance effects at the pile base [5]. A cross-validation has then been conducted, by comparing the code results with the ones produced by *OPILE*, a 1D finite difference software developed by Cathie Associates.

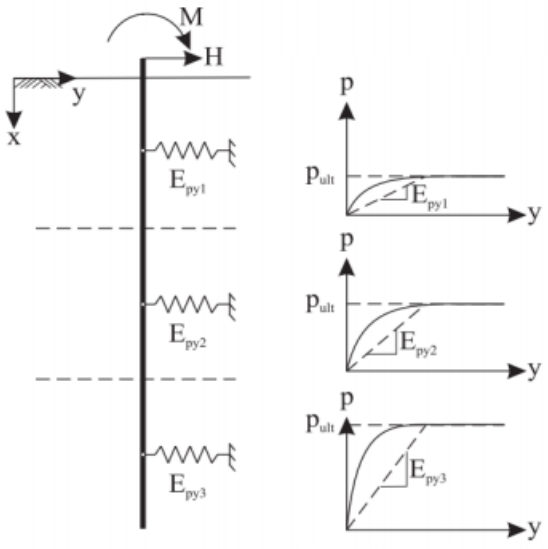

Figure 4.1: 1D model for laterally loaded monopile - soil as horizontal uncoupled springs and governing *p-y curves*[43].

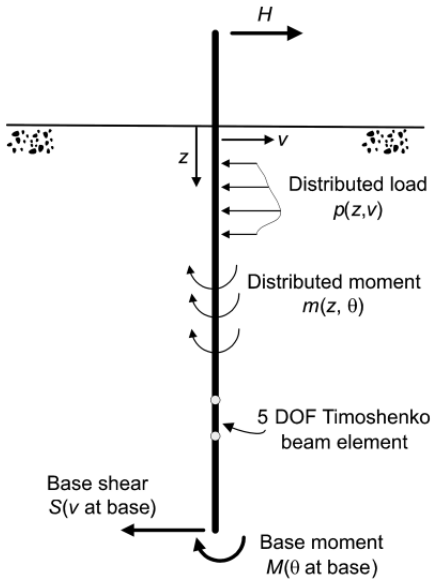

Figure 4.2: Framework for a 1D finite model for monopile foundations as proposed by the PISA project [5].

4.2 The Model

According to the finite elements method (FEM, [7]), a monopile is modelled as a discretized 1D beam under lateral loading and moments. The governing differential equation to apply depends on the mechanical and kinematic formulation: in our model the Euler-Bernoulli theory has initially been considered. As reported in paragraph 3.3.2, to represent the soil response the standard API-based method recommends the use of a series of horizontal uncoupled springs, reproducing a non-linear stress-deformation relationship defined by the *p-y curves* (Figure 4.1).
On the other hand, researchers suggest that the design of monopiles for offshore wind turbines should account for more effects in order to better reproduce all the mechanical phenomena. In Figure 4.2 we present a framework for the 1D finite model proposed by the PISA project, highlighting the additional effects to be included: among them, in our study we focused on the use of 2 degrees of freedom (DOF) Timoshenko beam elements and the resistance at the base in terms of moment and shear force.

In the next sections we report the main features of the model formulation.

4.2.1 Beam formulation

4.2.1.1 Euler-Bernoulli theory

The Euler-Bernoulli theory is based on the kinematic assumption that material points on the normal to the midline remain on the normal during a deformation [8]. It is usually suitable for slender piles (L/D<5), for which the shear deformations can be neglected - shear modulus $G \to \infty$. With reference to Figure 4.3, for small deflections the slope β of the midline can be expressed as function of the normal displacement u_3:

$$\beta = \frac{\partial u_3}{\partial x_1} = u_{3,1} \tag{4.1}$$

$$\begin{aligned} \epsilon_{11} &= u_{1,1} = -\beta_{,1} x_3 \\ &= -u_{3,11} x_3 = \kappa x_3 \end{aligned} \tag{4.2}$$

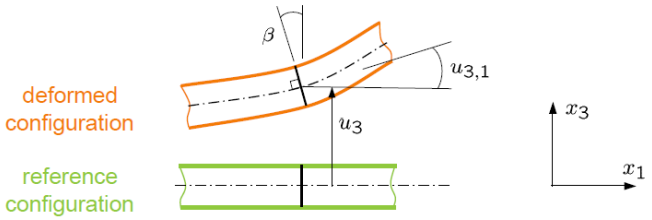

Figure 4.3: Assumed displacements during loading, for Euler-Bernoulli beam [8]

The axial strains ϵ_{11} are assumed to vary linearly across the thickness - equation 4.2, where u_1 is the axial displacement and κ is the curvature - while the other strain components are null.

4.2.1.2 Timoshenko theory

$$u_{3,1} = \beta + \gamma \tag{4.3}$$

$$\epsilon_{13} = \frac{1}{2}(-\beta + u_{3,1}) = \frac{1}{2}\gamma$$

$$\epsilon_{11} = -\beta_{,1} x_3 = \kappa x_3 \tag{4.4}$$

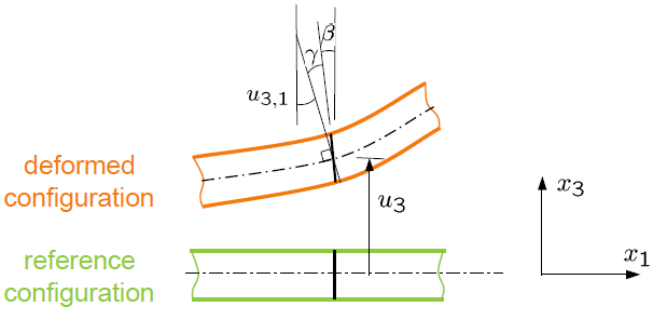

Figure 4.4: Assumed displacements during loading, for Timoshenko beam [8].

The Timoshenko theory is based on the kinematic assumption that a plane section originally normal to the centroid remains plane, but in addition also shear deformations occur. It is usually suitable for short piles (L/D>5), for which shear strains contribute significantly to the strain energy. With reference to Figure 4.4, for small rotations, the slope of the midline $u_{3,1}$ is expressed as function of the rotation angle of the normal β and the angle of shearing γ (equation 4.3); the axial strains ϵ_{11} vary linearly across the thickness, while the shear strains ϵ_{13} are constant (equation 4.4).

For both the theories, the resulting weak form and the stiffness matrix formulation are detailed in Appendix A (paragraph A.1.1).

4.2.2 Soil formulation

4.2.2.1 Lateral response

Each horizontal springs is applied to different beam nodes, reproducing the stress-deformation relationship inside the soil. The response to solicitations is then governed by the stiffness: for each beam element we can obtain the soil elementary stiffness matrix K^s_{el} by applying specific shape functions N_i. In particular the general element of the matrix is computed as:

$$K^s_{el,ij} = \int_0^l N_i k^s N_j dx = \int_0^l N_i \left(k^s_1 + \frac{k^s_2 - k^s_1}{l} x \right) N_j dx \tag{4.5}$$

where the element response k^s results from an interpolation of the (two) nodal responses $k^s_{1/2}$. In case of linear behaviour, the nodal response would be the same everywhere and k^s would be constant. On the other hand, when imposing a non-linear law - e.g. the *p-y curves* - the soil reaction depends on the beam displacements, hence an iterative resolution is necessary to back-calculate at each node the correct stiffness. The resulting soil stiffness matrices are reported in Appendix A (paragraph A.2).
The adopted law for the soil lateral response is based on the *p-y curves*: in particular we implemented the APIclay formulas and the proposed discretization of Jeanjean (2009) for monotonic loading, as presented in paragraph 3.3.2.1.
Once defined the soil response, the vector of solicitations g_{el} on the single beam element is modelled as nodal moments and shear forces, descending from the integration of shape functions applied to pressures back-calculated from the displacements and interpolated.
Similarly to equation 4.5, we obtain:

$$g_{el,i} = \int_0^l N_i p dx = \int_0^l N_i \left(\sigma_1 + \frac{\sigma_2 - \sigma_1}{l} x \right) dx \tag{4.6}$$

The resulting soil solicitation vector is reported in Appendix A.2.

4.2.2.2 Base response

For a pile under lateral loads, an additional resistance is mobilized at the tip. This resistance, resulting in a shear force V_b (N) and an overturning moment M_b (Nm), is said to contribute consistently in large-short piles, in which the diameter dimension is comparable to the pile length. The detailed finite element formulation is reported in Appendix A.2.
In terms of mechanical behaviour, the norms do not propose standards for the determination of these terms. At Cathie Associates they suggest an hyperbolic tangent function, as it provides a typical decreasing-slope shape, down to a residual value of resistance, while avoiding problems of derivability at zero displacement. Basically we assume a gradual decrease of the stiff response, down to a ultimate value of resistance $V_{b,ult}$ ($M_{b,ult}$) which is reached once a certain mobilization distance y_b (rotation θ_b) is registered. In particular:

$$\begin{cases} V_b = V_{ult,b} \tanh\left(\dfrac{y}{y_b}\right) \\ V_{ult,b} = \eta S_u A_b \end{cases} \tag{4.7}$$

$$\begin{cases} M_b = M_{ult,b} \tanh\left(\dfrac{\theta}{\theta_b}\right) \\ M_{ult,b} = \chi q_c \dfrac{A_b}{2} \dfrac{D}{4} \end{cases} \tag{4.8}$$

For the ultimate values, we assume: an undrained shear strength acting on the base section A_b (m^2), reduced by a coefficient η accounting for the contact between different materials - soil with concrete or steel; a maximal vertical pressure, equal to the end bearing capacity q_c, acting on half section and providing an overturning moment. According to field measurements, starting values for y_b and θ_b may be $0.01 \div 0.02$ m and $0.1°$.

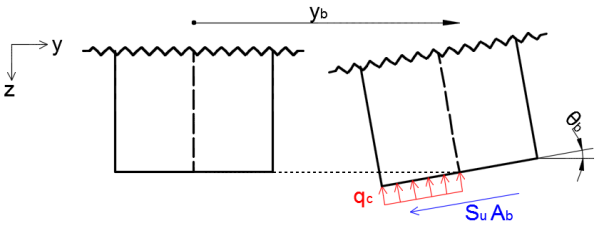

Figure 4.5: Horizontal displacement and rotation at pile base and resulting mobilized resistances.

However, we remark that this characterization is a first attempt, mostly resulting from *good sense*; it is clear that an accurate calibration of equations and values is required, e.g. with a 3D finite element analysis.

4.2.3 Code structure

The detailed structure of the code is reported in Appendix A.3.
Here we remark that the presence of a non-linear law requires the application of an iterative resolution method. In the *Python* code we implemented the Newton-Raphson method, based on the notion of internal, external and out-of-balance forces, as well as a displacement-governed convergence control. In every iteration the main linear system is resolved by means of the Gaussian Elimination - the inversion of the stiffness matrix is not recommended, as we deal with very sparse matrices which may *suffer* of ill-conditioning.[36]

4.3 Results

4.3.1 Beam theories comparison

At first, the two beam formulations have been separately validated. For Euler-Bernoulli (EB), assuming a linear-elastic soil around the beam, the results obtained from numerical simulations in *Python* have been compared with similar cases in *OPILE* and with the analytical solution resulting from the Winkler theory of beam on elastic foundation [14]. For a simple case of a clamped large-short pile deflected at the top - no soil included - the Timoshenko formulation has been compared to the corresponding analytical solution.
With reference to offshore monopile foundations, it is important to investigate in which specific cases the classic EB beam is not sufficiently representative of reality and the Timoshenko theory must then be adopted. At this purpose the two beams have been directly compared in *Python*. We considered a free steel pile - Young's modulus of 205 GPa - with hollow section and two different geometries: a slender 25×2 m (length×diameter) and a large-short 24×8 m, respectively with a 2 cm and 8 cm wall thickness. The soil has been modelled according to the APIclay *p-y curves*, with a typical cohesion of 100 kPa, then artificially increased to 5 MPa (rock-type) to generate bending in the pile. The comparison has been based on the computed displacements and beam potential energy, as defined in Appendix A.
In Table 4.1 we resume the results for three cases. Note that for the first pile case, for which a typical bending behaviour has been registered - as in Figure 3.6, paragraph 3.3.2.1 - the variation in the mud line deflection is negligible, as well as in the shear potential energy: therefore we conclude that for slender piles ($L/D < 5$) the use of the simplified Euler beam theory is justified, as shear phenomena are negligible - end of equation A.3 validated. Nonetheless, the change of geometry alone does not bring evident differences in the displacement (second case in Table 4.1): in fact, even if the shear energy is not negligible any more, the pile behaves in a rigid way, not showing enough bending (Figure 4.6).

Geom	S_u (kPa)	V (MN)	Beam	U_b (kJ)	U_s (kJ)	U_{tot} (kJ)	y_{ml} (m)	y_{tip} (m)
25×2 m	100	6	Euler	345	0	345	0.299	-0.0041
			Timo	343	11 (3%)[a]	354	0.301 (+0.7%)[b]	-0.0043
24×8 m	100	20	Euler	18	0	18	0.689	-0.2481
			Timo	18	8 (31%)	26	0.690 (+0.2%)	-0.2479
24×8 m	5000	400	Euler	4950	0	4950	0.116	-0.0221
			Timo	4680	2380 (34%)	7060	0.131 (+13%)	-0.0220

Table 4.1: Resume of the three main simluations. From left to right: geometry, cohesion, lateral load at the mud line, beam type, bending-shear-total beam energy, displacement at mud line and tip.

[a]Contribution of shear energy in the total energy. [b] Variation with respect to EB

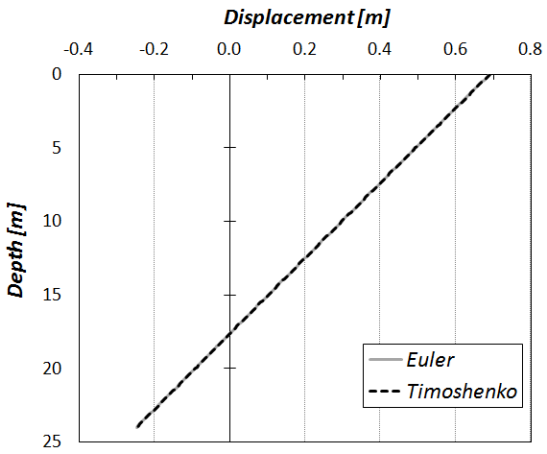

Figure 4.6: Free large-short pile under lateral load at mud line: comparison Euler/Timoshenko beam displacement - clay-type cohesive soil.

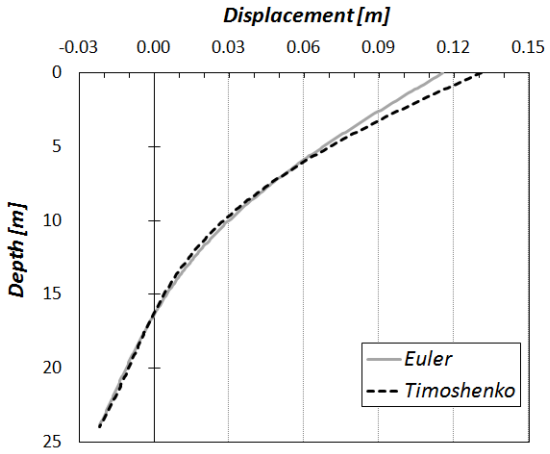

Figure 4.7: Free large-short pile under lateral load at mud line: comparison Euler/Timoshenko beam displacement - rock-type cohesive soil.

The increase of the cohesion (third case) simulates a rock-type soil: note that, as remarked in paragraph 3.3.2.1 (Figure 3.16), in the APIclay formula a higher value of undrained cohesion - therefore of ultimate resistance - results in a higher stiffness response. As a result, the relative rigidity of soil and pile in such that the steel large pile bends (Figure 4.7). As expected, the shear energy energy is not negligible and, in addition, a differential of 13% in registered for the displacement at the mud line. We conclude that for clay-like materials the Euler formulation is still applicable even with large-short piles, without the risk of excessive underestimation of the mud line deflection - a similar indication is given by Augustesen (2009)[37]. As we move towards very stiff soils the Timoshenko beam is recommended for large-short piles.

4.3.2 Cross-validation

4.3.2.1 Lateral response

The iterative resolution method implemented in *Python*, has been validated by comparison with *OPILE* of main variables in three relevant cases. The parameters for soil and pile are resumed in Table 4.2 and 4.3.

S_u (kPa)	γ_s (kN/m3)	$\varepsilon_{50,s}$ (%)	E_P (GPa)	ν_P (-)
100	16	1	205	0.3

Table 4.2: Constant parameters. From left to right: soil undrained strength, voumic weight and half-failure deformation; pile Young's modulus and Poisson's ratio.

case	$L \times D$ (m×m)	wall thickness (cm)	Load (MN)
Short	8×2	2	0.6
Slender	25×2	2	9
Large	24×8	8	9

Table 4.3: Variable parameters.

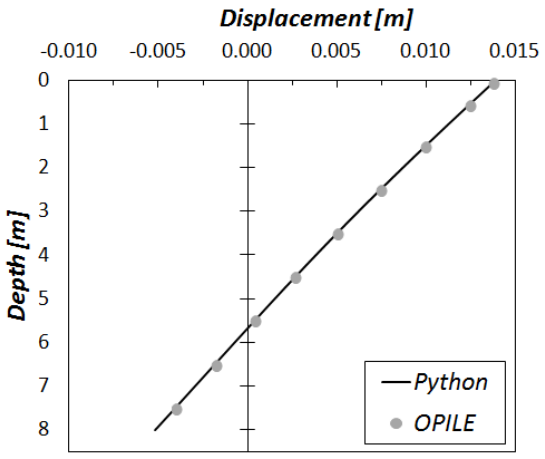

(a) Displacement depth profile.

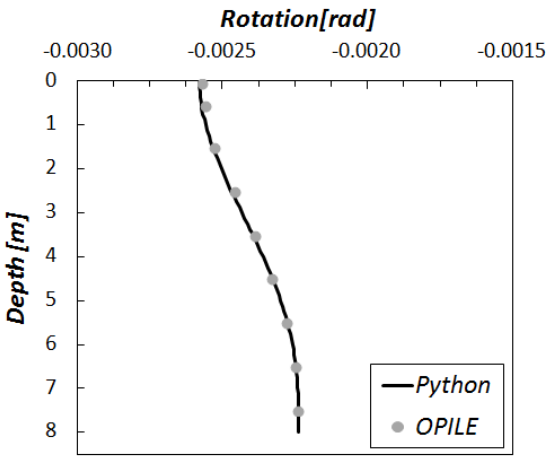

(b) Rotation depth profile.

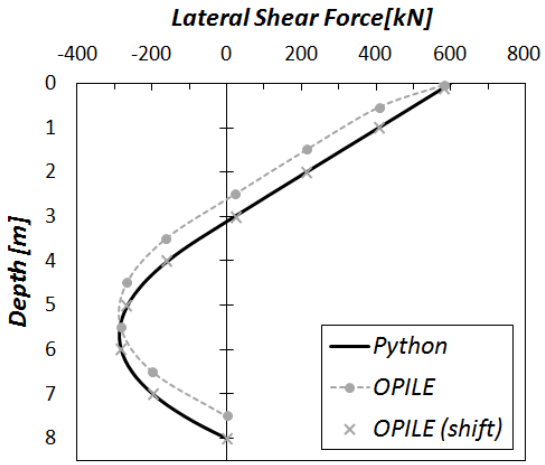

(c) Shear force depth profile.

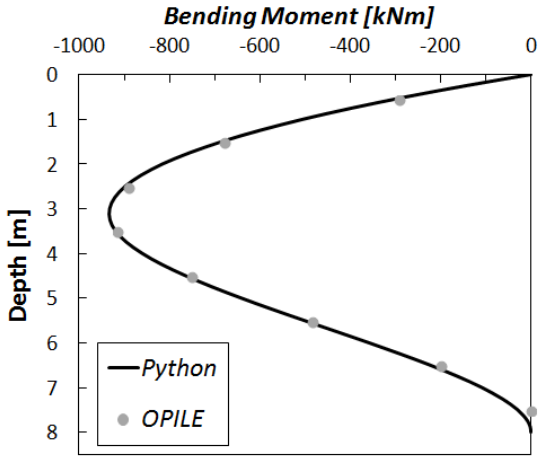

(d) Bending moment depth profile.

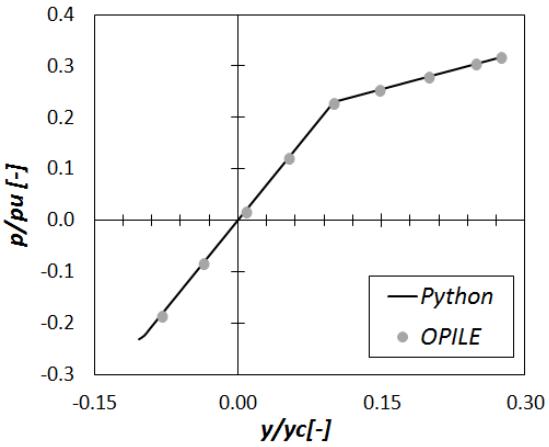

(e) Normalized *p-y curve*.

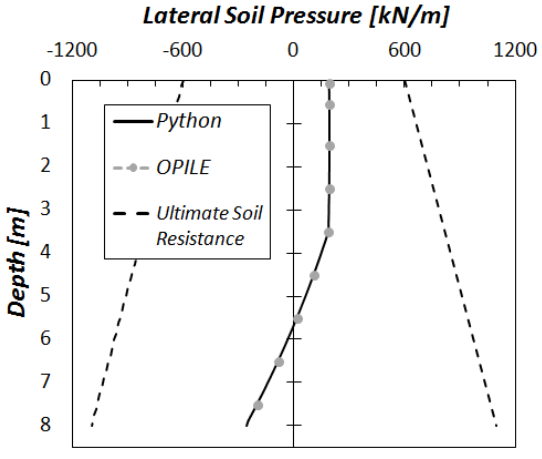

(f) Lateral pressure depth profile.

Figure 4.8: Short pile under lateral load at mud line: cross-validation with *OPILE*.

In *Python* we made use of the Timoshenko beam formulation, the discretized API-clay *p-y curves* and a vertical discretization of 0.125 m; in OPILE the discretization is 0.1 at the mudline, while 1 m elsewhere. The results for the short pile case are presented in Figure 4.8. The fit is perfect for almost all the main variables - displacement (4.8a), rotation (4.8b), bending moment (4.8d), soil pressure (4.8e) and *p-y curve* (4.8f). In the shear force profile (4.8c) the OPILE curve results to be shifted

upward of half element length, which is 0.5 m (0.05 at mud line): in fact, the same curve shifted *downward* ends to fit very well with *Python*. At Cathie Associated they believe this being due to a post-processing bug: a typical coding error in this cases is the wrong indexing inside a loop, e.g. starting from index 0 instead of 1. Probably OPILE, instead of returning the value of a certain cell at its centre, it returns the value at the top of the cell. This is confirmed by the fact that the null moment condition at the pile base is wrongly imposed at 7.5 m rather than at 8 m.

Similar results have been obtained for the slender pile - we do not include the graphs.

4.3.2.2 Base response

The large pile case of Table 4.3 is considered, with and without an additional term of base resistance: the shear force as defined in equation 4.7, with η=0.8 and y_b=0.01 m. Since *OPILE* does not have an integrated function to provide base resistance, this is simulated by adding manually the contribution resulting from *Python* to the *p-y curve* of the last element - a similar procedure for moment resistance is less evident instead. The new curve results then in a stiffer response and a larger mobilizable resistance (Figure 4.9).
The results are reported in Figure 4.10.

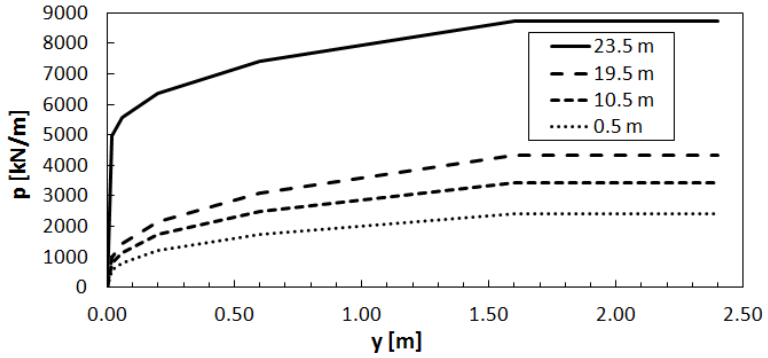

Figure 4.9: Large pile with base shear resistance: *p-y curves* at some locations in OPILE, including at last element (23.5 m depth).

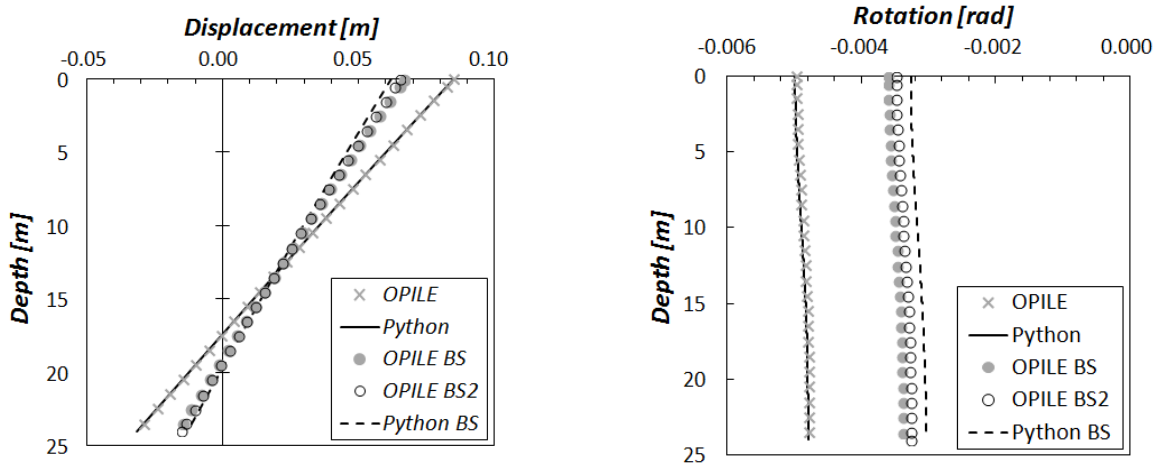

(a) Displacement depth profile.

(b) Rotation depth profile.

Figure 4.10: Large pile under lateral load at mud line: cross-validation with *OPILE*. With and without base shear (*BS*) resistance; * for a denser discretization at base (last element of 0.1 m instead of 1 m).

A focus on *Python* and *OPILE* solution without base shear resistance leads to the same conclusions of paragraph 4.3.2.1 - good fit, post-processing bug - hence we show only the shifted curves in 4.11a. Once introduced, the base resistance limits the deflection at the base as well as at the mud line, due to the rigid rotation; the internal forces increase, and the lateral force at the base corresponds to the base resistance value (3479 kN in *Python*) - close to the ultimate value, since the mobilized distance

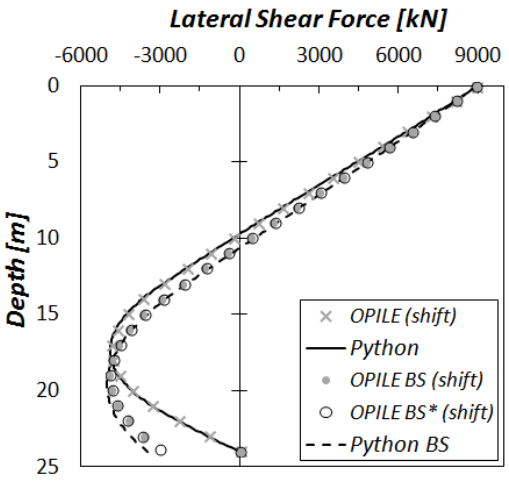

(a) Shear force depth profile. *Shift* for curve shifted downward of half element length.

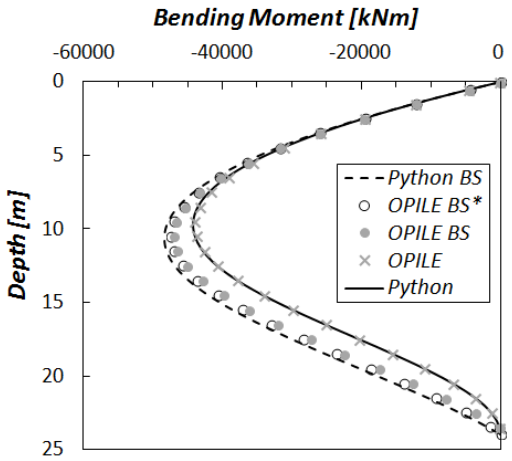

(b) Bending moment depth profile.

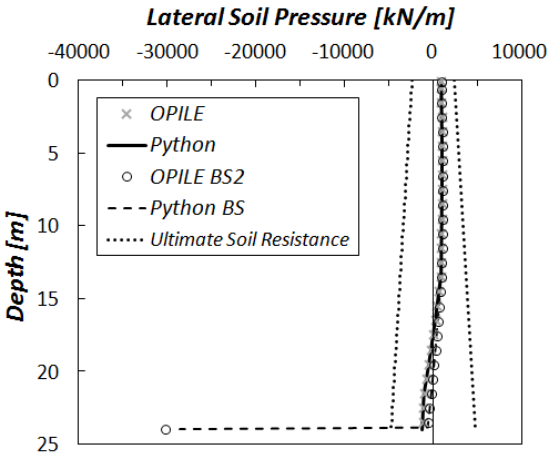

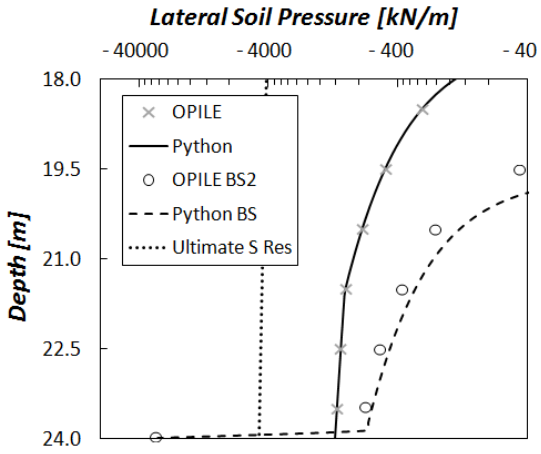

(c) Displacement depth profile.

Figure 4.11: Large pile under lateral load at mud line: cross-validation with *OPILE*. With and without base shear (*BS*) resistance; * for a denser discretization at base (last element of 0.1 m instead of 1 m).

is of 0.013 m ($> y_b$).
The fit between OPILE and *Python* improves as a denser discretization at the base is applied in OPILE - from 1 m to 0.1 m: this is logic as the finite differences method returns values at the centre of each element, therefore, if this (last) element becomes shorted, the condition tends towards a nodal one in a finite elements model.

4.4 Conclusions

We conclude that the inclusion of this term is recommended, in order to avoid an overestimation of the pile displacement. The 1D code in PYTHON has successfully been validated with the finite difference program OPILE, identifying a post-processing issue in this last. It has been showed that in some cases the standard method based on Euler-Bernoulli (EB) beam and lateral springs requires some improvements: at first, the Timoshenko beam provides a better prediction of pile deflection and internal forces for short piles presenting enough bending, therefore in very stiff and hard soil. In presence of a rigid behaviour and for slender piles, the EB formulation is still valid.
Moreover, additional moment and shear base resistance terms have been implemented, representing a rotational and lateral spring at the pile tip: while the first one has not been validated - still, we believe that the formulation can be taken as a reference - the presence of base shear can limit the pile deflection, either at the base and at the mud line.

Chapter 5

3D Finite Element Analysis

5.1 Introduction

In this chapter we present the 3D finite element analysis conducted by means of LAGAMINE. As mentioned, 3D modelling is widely applied in continuum mechanics with the aim to re-asses existing laws: in fact, the continuous nature of the material - in this case the soil - is explicitly modelled and, starting from base parameters, typically defining elastic and resistance behaviour, the overall response is observed and analysed with reference to specific variables.
In our study the focus is on the response of the pile-soil system under lateral loads, which is characterized by means of extracted *p-y curves*. While in a 1D model the curves are imposed as an input, therefore the results are very sensitive to their selection, in a 3D model they represent the output, as they are re-built proceeding backward.
In the next section we present the approach used in the model, which will be applied later on.

5.2 The Model

5.2.1 Geometry and boundary conditions

In Figure 5.1 we provide a scheme of the pile-soil system. Later in the chapter different meshes will be used, for each of which we refer to this paragraph, as far as general geometry and boundary conditions are concerned - the variations will concern the type of pile section, the pile dimensions and the presence (or not) of the soil all around the pile.
Note that only half of pile and soil are modelled - symmetry with respect to y-z plane. The applied boundary conditions (Figure 5.1) are null displacements on the lower surface along the z-axis, on the symmetry plane along x and on the curved lateral surface along x and y.

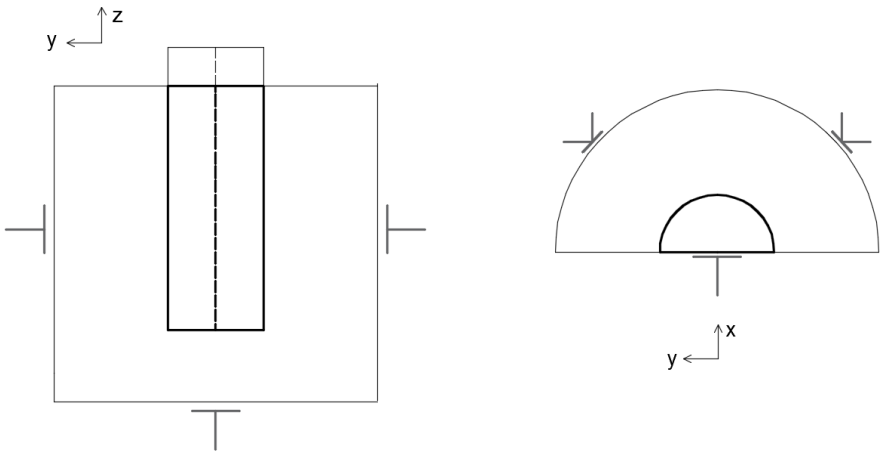

Figure 5.1: scheme of a monopile with surrounding soil, additional element at the head and boundary conditions.

Two types of solicitation will be used: a lateral rigid displacement and a deflection at the mud line. While in the first case the coordinates of all the pile nodes are imposed, the second solicitation is applied by realising alternatively an embedded head or a hinge. The schemes are presented in Figure 5.2, in which the targeted point are nodes of the additional element at the pile head.

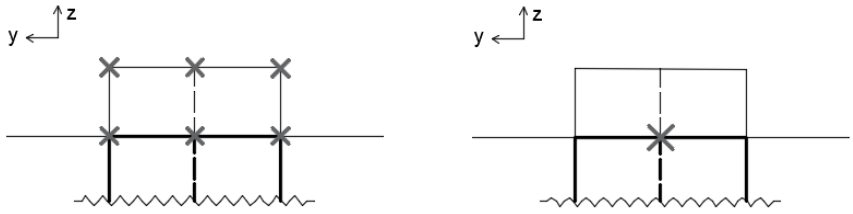

Figure 5.2: scheme of imposed conditions for a mud line deflection - embedded pile head (left) and hinge (right).

As the model does not include complex geometries, the gravity is simply imposed by defining vertical and horizontal stresses. For numerical reasons, an interface element is implemented to realise the contact between soil and pile: a certain penetration must be allowed, defined by the penalization factor K_p. Its value will be constant for all the simulations (10^9 Pa) - studies of sensitivity have established that in our models, with the considered stiffness parameters, it does not affect the results. Similarly, the dimensions of the proposed meshes guarantee a smooth variation of the variables from the centre to the boundaries of the models.

5.2.2 Processing and post-processing

The resolution method is such that for every iteration a certain number of sub-steps provide the local convergence. The convergence criteria are based on the norm of displacements and stresses. The time of a complete simulation varies between 1 and 20 hours.

Once completed, each simulation provides output files. These files are post-processed by means of Matlab routine, able to isolate specific groups of data.
Wolf (2013)[44] reports some indications for the extraction of the *p-y curves*. In our work, the extraction of the pressure component along y has been realised by targeting specific integration points all around the pile.

5.2.3 Structure of the analysis

In the analysis two different geometries are investigated, a slender and a large pile. For the first pile, a simplified model provides a sensitivity analysis aimed to identify all the phenomena contributing to the soil-pile response; for the second pile, the simplified model is useful to highlight the effect of a lower slenderness. Then, for both geometries, full models reproduce more realistic conditions.

5.3 Slender Pile

5.3.1 Rigid displacement

A sensitivity analysis has been performed while applying an homogeneous rigid displacement to a 25×2 m (length×diameter) slender pile. The mesh is showed in Figure 5.3. Note that an interface element surrounds the solid section and no soil is included at the base - the focus is specifically on the pure lateral response and base effects are to be avoided; the additional 1 m long element emerging from the soil provides an additional rigidity at the pile head, so that the displacements are more easily imposed in this area, and it helps to maintain the contact with the soil, which here is expected to move upward and create a *bump*. A model of only half of soil and pile is supposed to be representative of the whole phenomenon - symmetry with respect to plane *y-z* - and the mesh is refined around the pile. The boundary conditions are the ones previously detailed.

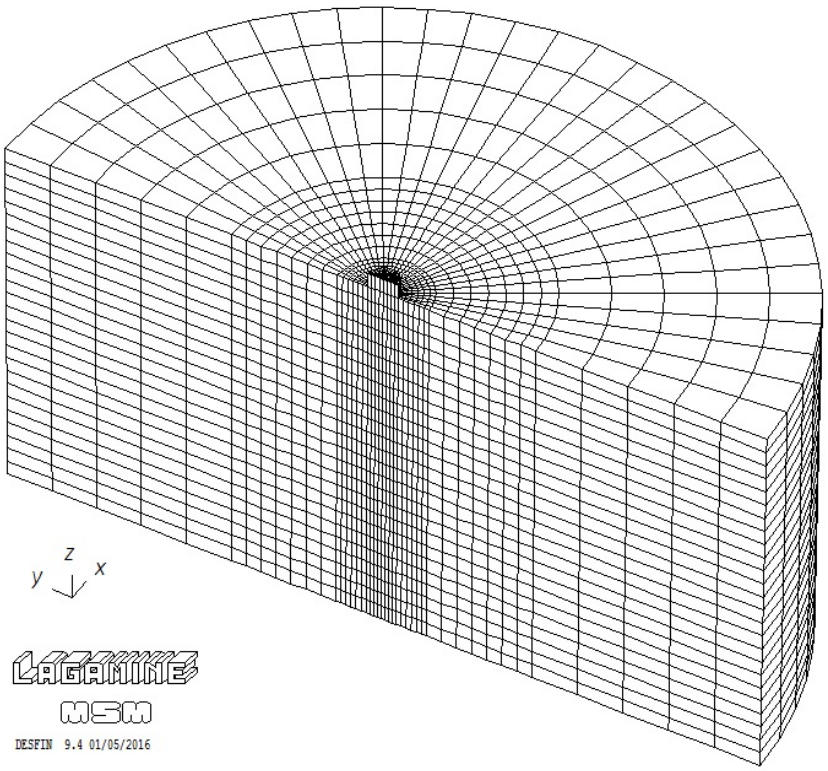

Figure 5.3: Mesh for a circular 25×2 m slender, solid concrete section with lateral soil and interface element.

We made use of three different soil constitutive laws, providing a gradual increase of complexity; the main parameters have been tested in order to evaluate their impact on the resulting *p-y curves*. Note that, rather than an all-inclusive soil characterization, in this phase a solid understanding of the curves in terms of the main contributions is the main goal. Therefore the choice of the parameters is meant mainly to highlight the different physical phenomena rather than to represent a specific soil material.
In Table 5.1 we present the main cases: as mentioned, we pass from simple infinite elasticity (E1, E2, E3), eventually with friction at the interface (E3-f1/2), to an elasto-perfectly plastic law (EP1), to elasto-plasticity with hardening (H1). The main parameters are the Young's Modulus E, the friction angle ϕ_{int} at the pile-soil lateral interface, the initial and final undrained strength $S_{u,I/F}$; the unvaried parameters are listed in Table 5.2. A single homogeneous soil layer is considered, assuming the soil saturated in terms of volumic weight; on the other hand pore water pressures are neglected (we work in total stresses) and a volumic compressibility is still included. An undrained Poisson's ratio will be used only in the latter phases of analysis, as it is usually makes the simulations more time-consuming.

The applied solicitation, common for all the cases, is showed in Figure 5.4. The displacement-

Case	E (MPa)	ϕ_{int} (°)	$S_{u,I}$ (kPa)	$S_{u,F}$ (kPa)
E1	2	-	∞	∞
E2	20	-	∞	∞
E3	200	-	∞	∞
E3-f1	200	30	∞	∞
E3-f2	20	35	∞	∞
EP1	2	-	100	100
EP2	20	-	100	100
H2	20	-	10	100

Table 5.1: main cases and respective main soil parameters.

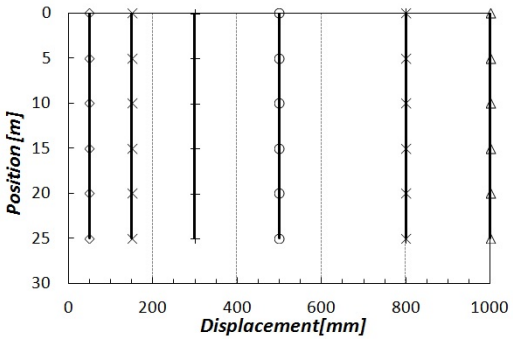

Figure 5.4: main steps of the displacement-controlled path applied to each case. The position is relative to the pile main fibre, in the direction of the y-axe in Figure 5.3.

ν_s (-)	γ_s (N/m$_3$)	K_0 (-)	B_c (-)	κ_p (Pa)	$(L \times D)_P$ (m×m)	E_P (GPa)	ν_P (-)
0.3	20725	1	0.001	10^9	25×2	20	0.3

Table 5.2: unvariant parameters. From left to right: soil Poisson's ratio and volumic weight, coefficient of lateral pressure, hardening gradient, interface penalization factor, pile dimensions, Young's modulus and Poisson's ratio.

controlled path has a limited physical meaning, since in reality solicitations on piles are usually load-related; on the other hand, these lasts, in presence of plastic laws, may lead to missed convergence for big loads. Furthermore, a rigid displacement allows the mobilization of the soil reaction all along the pile, hence providing complete *p-y curves* at all depths (Wolf 2013).
In the next paragraph, for the different cases, we will analyse the main variables present in *Desfin* (cite Lagamine) - displacements, stresses, deformations, cohesion, contact pressure and specific state variables - and the pressure profiles extracted with the Matlab routine.

5.3.1.1 Elasticity

Soft soil

At first, case E1 is analysed, representative for a soft material. The rigid displacement of the pile results in a lateral confinement of the soil in front of the pile and a de-confinement behind (Figure 5.6a): the de-confinement leads to the generation of a *gap*, spreading downward step by step. The distribution of the pressure at the interface for high displacements (0.75 m) shows this detachment at the back (5.6b), which is almost complete - still a residual contact at the pile base. The resulting mean stress state (5.6c) shows that the initial stress state (ISS) distribution has been perturbed by the imposed solicitation, especially around the pile, while the values are still typical of a geostatic regime ($<$ 600 kPa). In Figure 5.6d the gap is visible and a slight concentration of the deviatoric stress at the mud line is registered, the reason for which will be clarified later on.

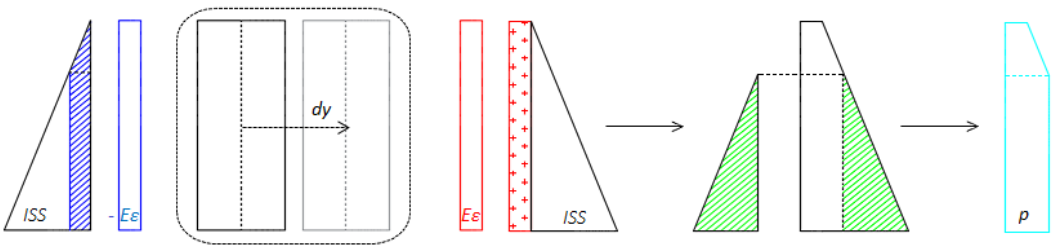

Figure 5.5: evolution of the stress state for pile under homogeneous lateral deformation: de-confinement at left, confinement at right. Resulting lateral pressure distribution, with gap extension.

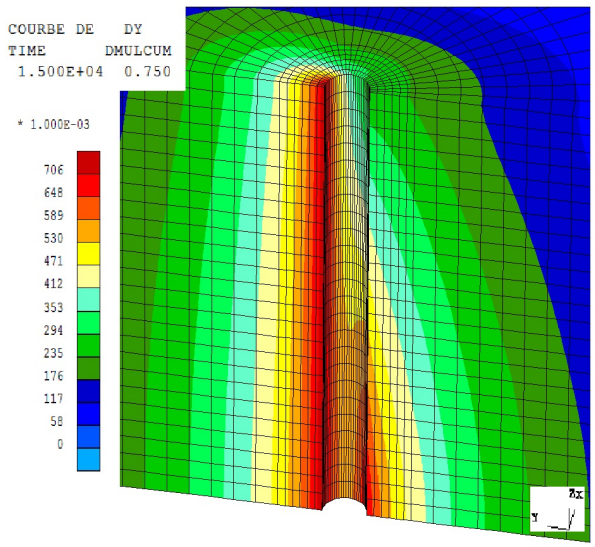

(a) Soil lateral displacement along y (m)[1]

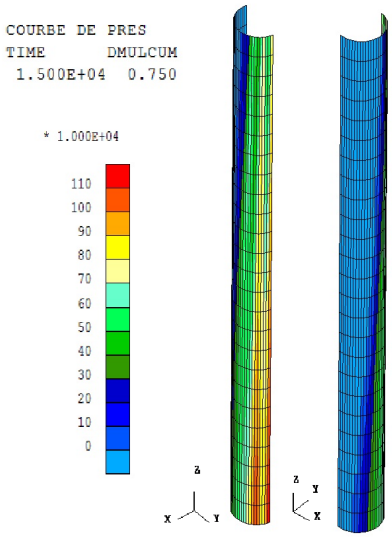

(b) Contact pressure at the soil-pile interface (Pa).

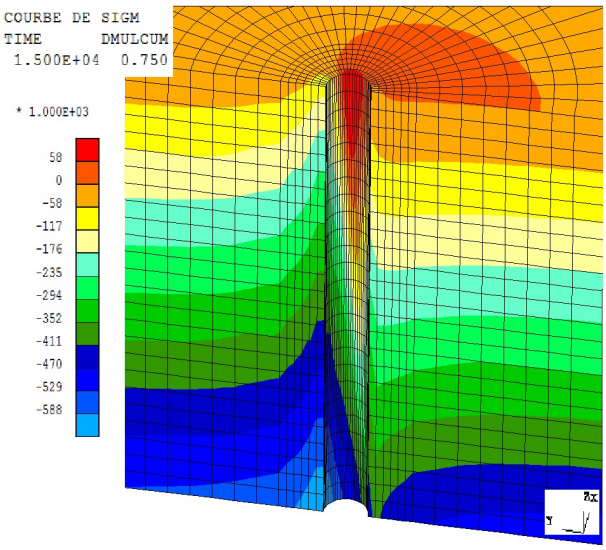

(c) Mean stress (Pa).

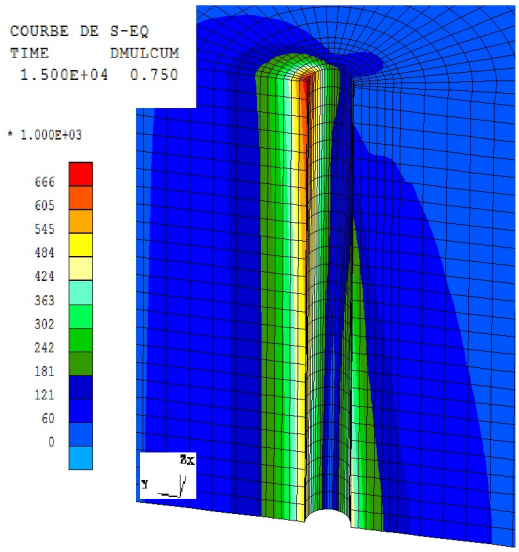

(d) Equivalent stress of Von Mises (Pa).

Figure 5.6: case E1 - main variables for a 0.75 m pile rigid displacement.

The evolution of the stress state is explained in Figure 5.5, where we just consider the two opposite side of the pile. We suppose that the rigid displacement results in a constant-in-depth lateral deformation along the pile, generating a stress by means of the soil elastic stiffness - here simply E-related; the ISS is then modified by the confinement (de-confinement), generating a trapezoidal (triangular) distribution. The lateral pressure of the *p-y curves* results from the integration around the pile of all the contributions, in this case the difference between the two distributions: in the final trapezoid the gap extension is clearly visible.
For case E1, the depth profile of p, the mobilized lateral pressure towards the displacement direction at a given depth, is showed for different phases in Figure 5.7 - note the similarities with Figure 5.5. The gap propagates gradually and, at high displacements, it reaches the base: the profile is linear along the pile, meaning that the ISS is still comparable to the solicitation - soft soil - while we detect a slight mud line effect, related to the stress concentration close to the surface. The *p-y curves* at different locations in depth are presented in Figure 5.8, characterized by bi-linearity. The slope of the first part (in blue) is governed only by the solicitation: in fact it represents the locations where the soil is still in contact all around the pile, therefore the ISS does not contribute - the integral is null. The

[1]In every image extracted from *Desfin* we report the simulation time step, the cumulative displacement multiplier and the scale; where not specified, only the soil is showed - no pile nor interface element.

second slope (in red), estimated at ca 0.75 MPa, is governed by the solicitation and the *frontal* ISS, as at the back the detachment has annulled the initial linear contribution. The break points between the two slopes represent the gap, occurring immediately at the mud line while later in depth.

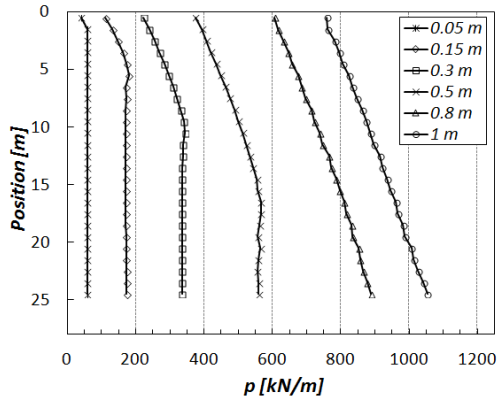

Figure 5.7: case E1 - *p-z* profile for different rigid pile displacements.

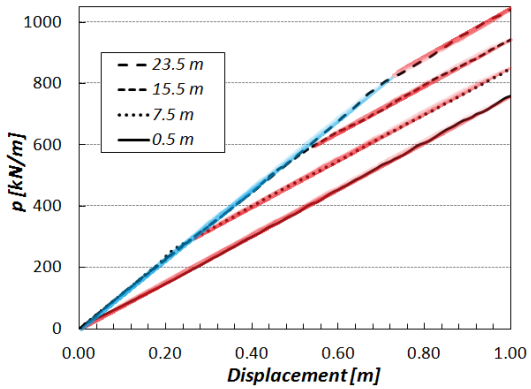

Figure 5.8: case E1 - *p-y curves* at some locations.

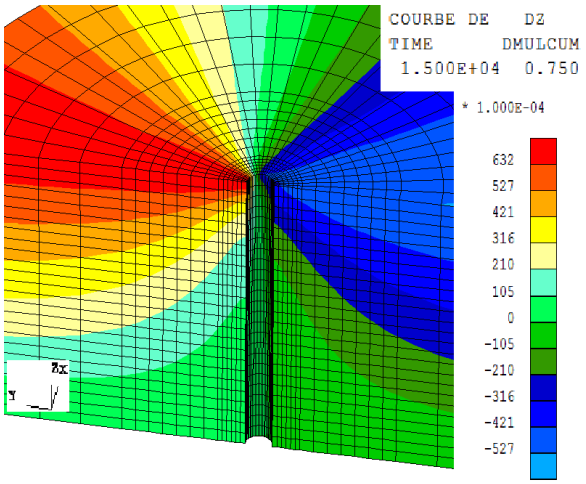

(a) soil vertical displacement along z (m) for a 75 cm displacement.

Hard soil

For case E3 the Young's Modulus has been increased to 200 MPa. In Figure 5.9a the deconfined soil moves downward and generates the gap, while the confinement leads to an accumulation of soil, creating a bump in front of the pile - phenomenon detected but almost negligible for the soft soil. Assuming the displacement-generated deformation constant along the pile, the higher stiffness is such that the ISS is perturbed even at low displacements (5 mm, Figure 5.9b); then, as the solicitation increases, the mean stress passes from a linear to a constant distribution in depth, up to a maximum values of 15 MPa around the pile (1 m).

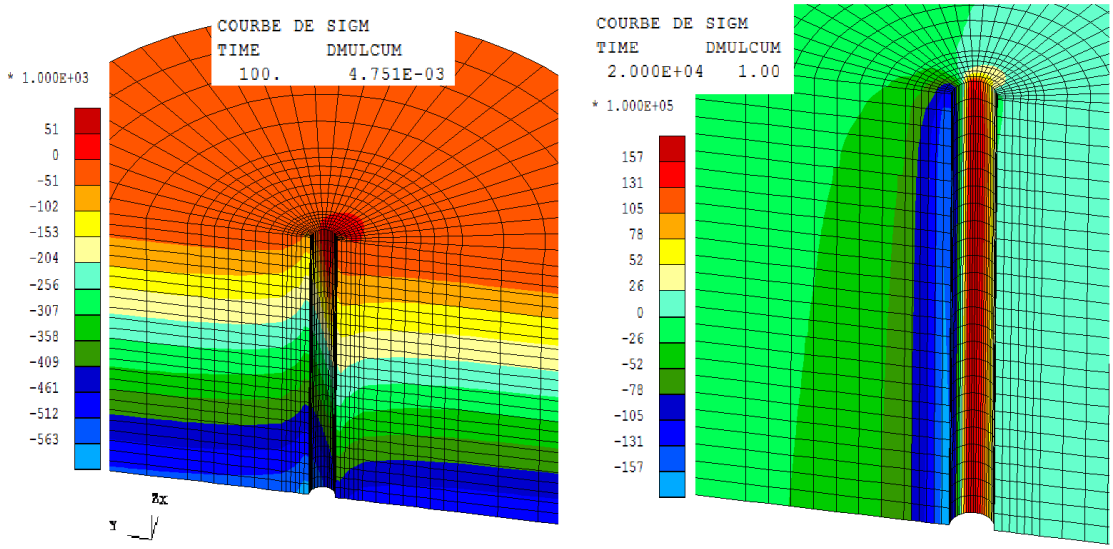

(b) Mean stress (Pa) for a displacement of 5 mm (left) and 1 m (right).

Figure 5.9: case E3 - main variables at different pile rigid displacements.

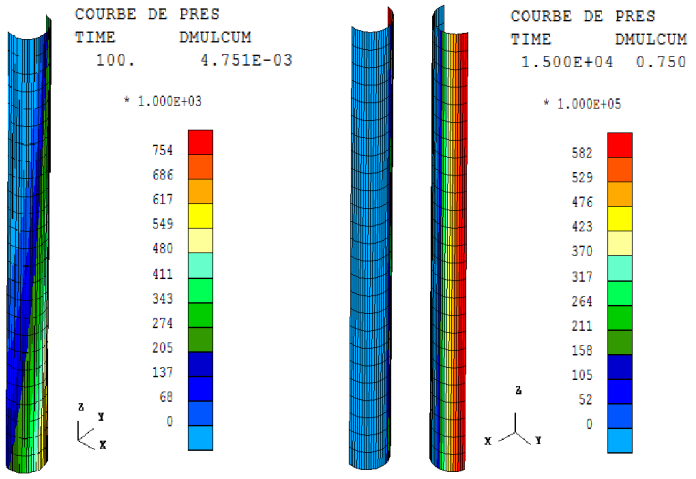

(a) Contact pressure at the soil-pile interface (Pa) for a displacement of 5 mm (left) and 75 cm (right).

In addition, since a lower amount of deformation is sufficient to de-confine, the detachment is *quicker* (Figure 5.10a) - gap well developed at 5 mm - and at 75 cm of rigid displacement the loss of contact at the back is complete; the contact pressure is applied homogeneously in depth and has a maximum at the front. Here the bump leads to an important concentration of deformations, therefore of deviatoric stresses, even at low displacements (Figure 5.6d) - in section, the pick is on the upper intersection between the interface and the y axe.

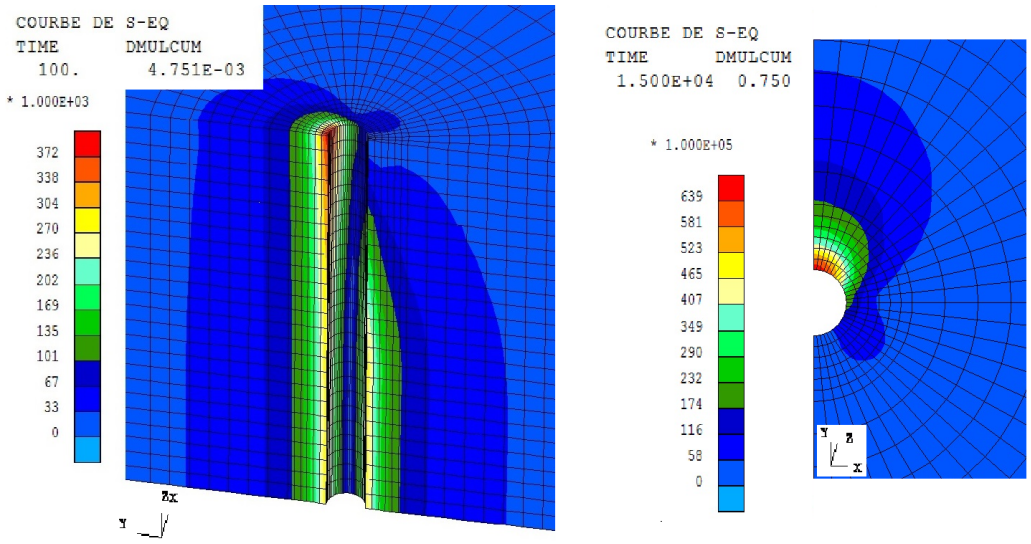

(b) Equivalent stress of Von Mises (Pa) for a displacement of 5 mm (left, standard perspective) and 75 cm (right, horizontal section at pile head).

Figure 5.10: case E3 - main variables at different pile rigid displacements.

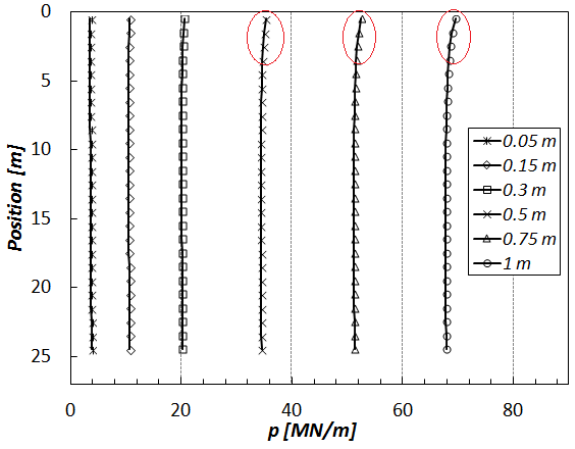

Figure 5.11: case E3 - p-z profile for different rigid pile displacements.

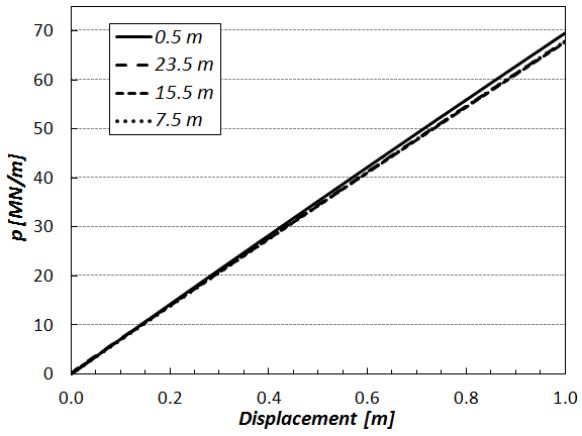

Figure 5.12: case E3 - *p-y curves* at some locations.

The extracted profile of pressure in depth (p-z) is reported in Figure 5.11. Note that, due to the *quick* detachment, the propagation of the gap is not visible any more and the profiles are almost constant, being the solicitation much higher than the ISS. For the same reasons, the corresponding p-y *curves* consists only of one slope (Figure 5.12): comparing to Figure 5.8, the first slope is not visible and almost all the locations in depth follow the same path. Only the mud line curve is detected as slightly stiffer, because of the mentioned bump-related stress concentration - effect highlighted in the p-z profile.
Note that between the two cases the final slope has passed from ca 0.75 MPa to ca 70 MPa, confirming our hypothesis of dependence on the solicitation, which increased as the Young's modulus increased 100 times.

Medium stiff soil

For case E2 an in-between value for the Young's modulus has been included, resulting in an in-between behaviour. The p-z profile is reported in Figure 5.13: the gap propagation is detected in the very first curves, then for higher pile displacements the ISS contribution is visible - linear profile - as well as the mud line effect. In the corresponding p-y *curves* (Figure 5.14) the bi-linearity is weak but visible, as well as the stiffer mud line curve. The final slope in estimated at ca 7.5 Mpa, consistent with the previous cases.

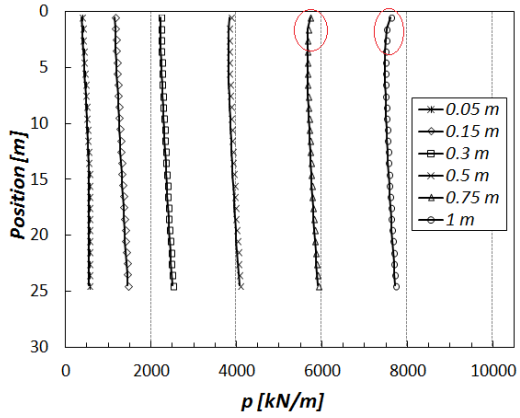

Figure 5.13: case E2 - p-z profile for different rigid pile displacements.

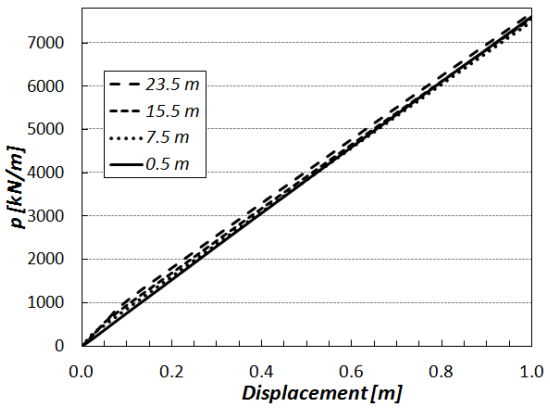

Figure 5.14: case E2 - p-y *curves* at some locations.

Hard soil with friction at interface

For case E3-f1, friction (30°) is assumed to act at the interface between the pile and a stiff soil.

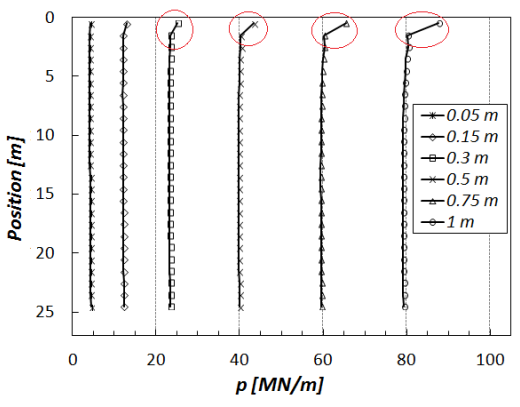

Figure 5.15: case E3-f1 - p-z profile for different rigid pile displacements.

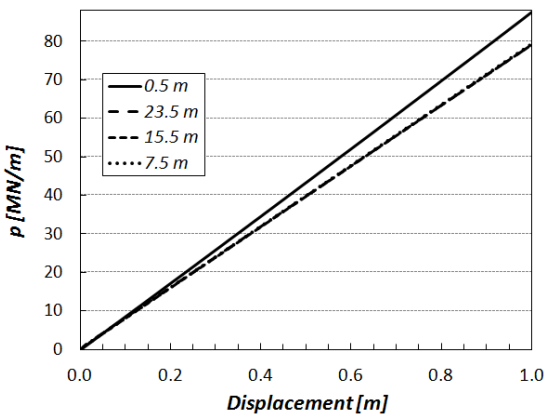

Figure 5.16: case E3-f1 - p-y *curves* at some locations.

This results in the mobilization of an additional resistance at a given pile displacement: comparing to case E3 (Figure 5.11), the *p-z* constant profiles in Figure 5.15 are *shifted* to the right and the *p-y curves* are stiffer (5.16) - final slope ca 80 MPa, governed by ISS, Young's modulus and friction angle. The mudline effect is enhanced and the solicitation at the interface is redistributed laterally due to shear stresses, with the deviator pick point moving farther from the main displacement direction (Figure 5.17a). The gap propagation/detachment and the constant-in-depth final solicitation can be seen in the evolution of the contact shear stress (Figure 5.17b). These effects are enhanced - therefore confirmed - when introducing an higher friction angle (case E3-f2).

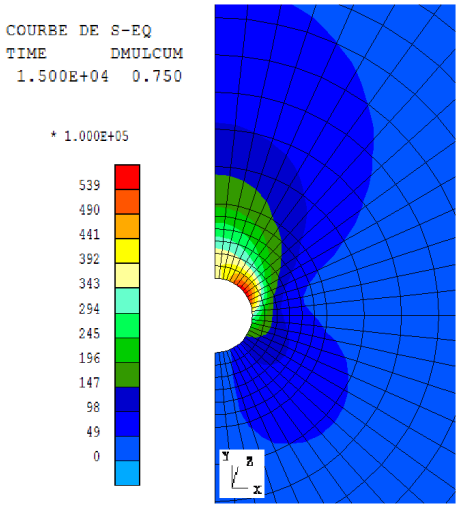

(a) Equivalent stress of Von Mises (Pa) in horizontal section at pile head for a 75 cm pile rigid displacement.

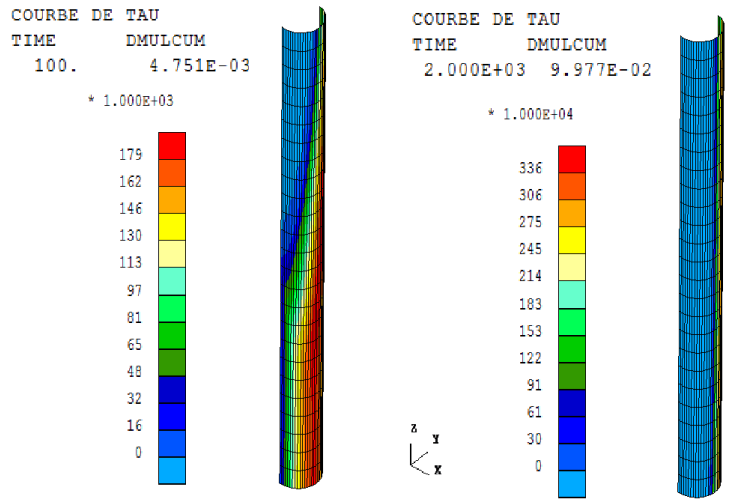

(b) Contact shear stress at the back interface (Pa) for a pile displacement of 5 mm (left) and 10 cm (right).

Figure 5.17: case E3-f1 - main variables at different pile rigid displacements.

5.3.1.2 Elastic response: coefficient of subgrade reaction

Before including soil cohesion, therefore plasticity, we can draw some conclusions on the calculated elastic response of the soil-pile system under static loading[2]. The focus is on what we previously called the *second* slope - in case E3, the only one, apart from the mud line - assumed to be more representative for the response, especially at shallow depths. Its value divided by the diameter can be compared with the coefficient of subgrade reaction k_s (MPa/m), which can be estimated according to a number of analytical methods, mainly based on the Winkler approach[46] and listed in equations 5.1.

$$k_s = \frac{0.95E_0}{D(1-\nu_s^2)}\left[\frac{D^4E_0}{(1-\nu_s^2)EI}\right]^{0.108} \textit{(Biot)} \qquad k_s = \frac{0.65E_0}{D(1-\nu_s^2)} \textit{(Selvadurai)}$$

$$k_s = \frac{E_0}{D(1-\nu_0^2)} \textit{(Meyerhof\&Baike)} \qquad k_s = \frac{2E_0}{D(1+\nu_s)} \textit{(Klopple\&Glock)} \tag{5.1}$$

$$k_s = \frac{0.65E_0}{D(1-\nu_s^2)}\left[\frac{D^4E_0}{EI}\right]^{1/12} \textit{(Vesic)}$$

where D (m) and ν are the soil diameter and Poisson's ratio, while in some methods the flexural rigidity EI of the pile (MPa×m^4) is included. Note that the soil Young's modulus required would be the small-strain one E_0 (MPa), as these methods are meant to investigate the initial stiffness of the p-y curves: this modulus is usually higher than the large-strain one, but in this phase for cases E1 to

[2]The Poisson's ratio, as elastic parameter, will be tested later in the analysis: as expected, tending towards undrained conditions ($\nu \rightarrow 0.5$) - null volumic deformations - the response will be stiffer.

E3-f2 we can suppose $E = E_0$. Later in the paper an *ad hoc* modulus will be introduced to simulate a stiffer initial response as well as some stiffness degradation. In Table 5.3 we present the results of the comparison, where from the 3DFEA the slope has been divided by the diameter of the (half) model (1 m) and we considered separately mud line and a location at 10 m of depth. A better view is provided by Figure 5.18, where the values are normalized by the 3DFEA result at 10 m depth. Note that, as mentioned, the mud line effect increases with friction; in addition, we conclude that the 3D simulation have returned quite consistent results and the best fit is with Selvadurai formula. However, for a better comprehension of the presented analytical methods and their main assumptions, we refer to Prendergast and Gavin (2016).

Case	Biot	M&B	Vesic	Selvadurai	K&G	3DFE-ml	3DFE-10m
E1	0.54	1.10	0.43	0.714	1.54	0.76	0.75
E2	6.93	10.99	5.16	7.143	15.38	7.54	7.32
E3	88.81	109.89	62.56	71.429	153.85	68.74	67.03
E3-f1	88.81	109.89	62.56	71.429	153.85	88.30	78.81
E3-f2	88.81	109.89	62.56	71.429	153.85	91.07	80.84

Table 5.3: coefficient of subgrade reaction (MPa/m): comparison between analytical methods and 3DFEA. Data from Table 5.1 and 5.2.

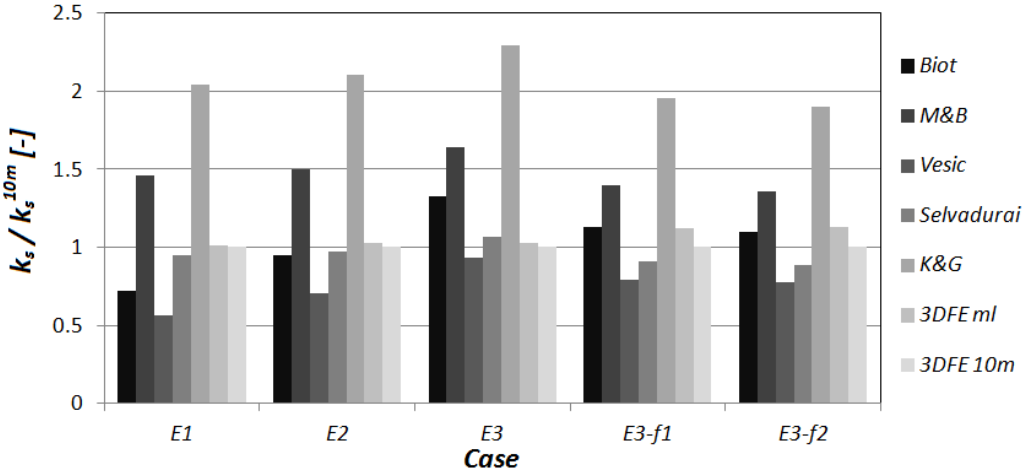

Figure 5.18: coefficient of subgrade reaction, normalized by 3DFEA results extracted at 10 m depth: comparison between analytical methods and 3DFEA

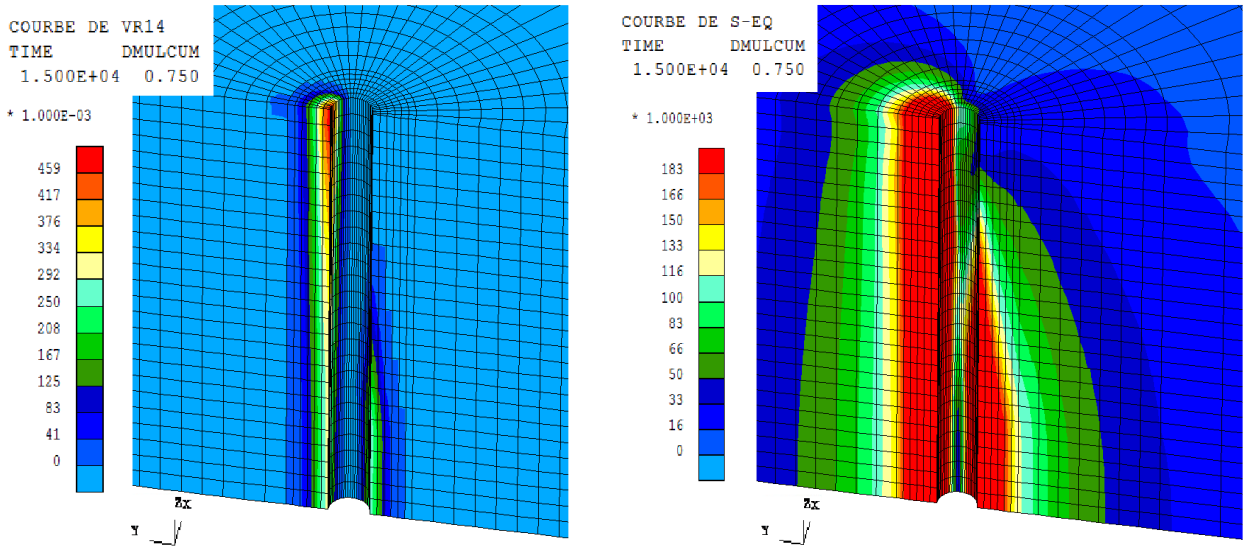

(a) Plastic deformation (-). (b) Equivalent stress of Von Mises (Pa).

Figure 5.19: case EP1 - main variables for a 75 cm rigid pile displacement.

5.3.2 Elasto-plasticity

Cohesive soft soil

Plasticity has been introduced by means of a 100 kPa undrained shear strength.
In case EP1 the stress concentration is such that the plastification begins at the mud line (Figure 5.19a). For high displacements, the confinement/de-confinement is stopped - once at the plateau, the deviator cannot increase any more - and, where the pile is still in contact with the soil, a plastic zone develops (Figure 5.19b). As mentioned in paragraph 3.3.2.1, Figure 3.10, the in-contact soil right in front (back) of the pile can be considered under triaxial compression (decompression): in fact the peak of the deviator is close to the triaxial failure value ($2 \times S_u$ =200 kPa). The *stopped* detachment at the back is showed in Figure 5.20.

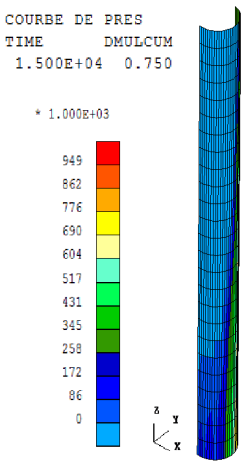

Figure 5.20: case EP1 - contact pressure at the back soil-pile interface (Pa) for a 75 cm displacement.

The same conclusions can be drawn for *p-y curves* and *p-z* profiles (Figure5.21,5.22), where in some curves we clearly observe a tri-linear behaviour - break points representing the plastification and the gap propagation.

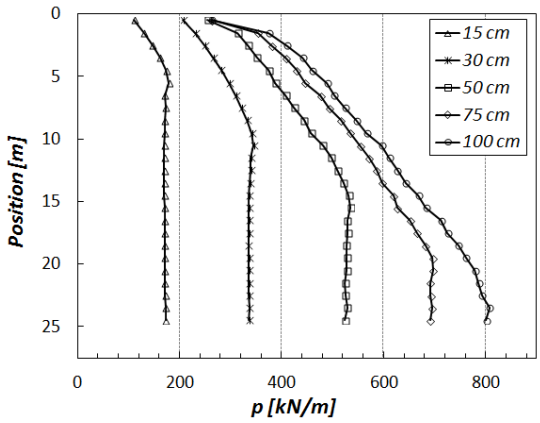

Figure 5.21: case EP1 - *p-z* profile for different rigid pile displacements.

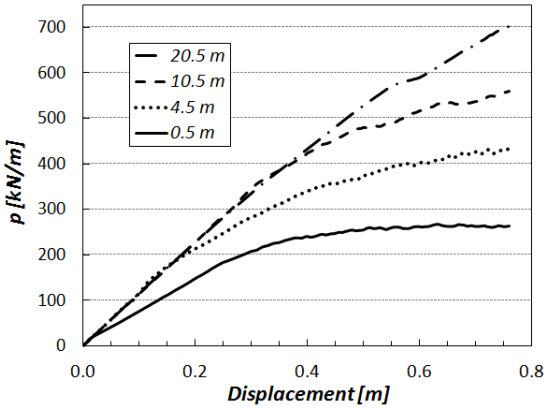

Figure 5.22: case EP1 - *p-y curves* at some locations.

Cohesive medium-stiff soil

With a stiffer soil (case EP2) the plastification is *quicker* - at a given pile rigid displacement the resulting solicitation is higher. Therefore at 75 cm the plastic zone is more extended and in the soil under under triaxial compression the deviator reaches 200 kPa. The *p-y curves* and *p-z* profiles are reported in Figure 5.24 and 5.25: in addition to the observations previously made, note that a pressure stabilisation for large displacements is registered only at shallow depths - here we show only the mud line - while in-depth locations follow parallel paths, keeping mobilizing resistance. This behaviour would require further analysis, e.g. by tracing the stress path in the deviatoric plane for relevant locations.

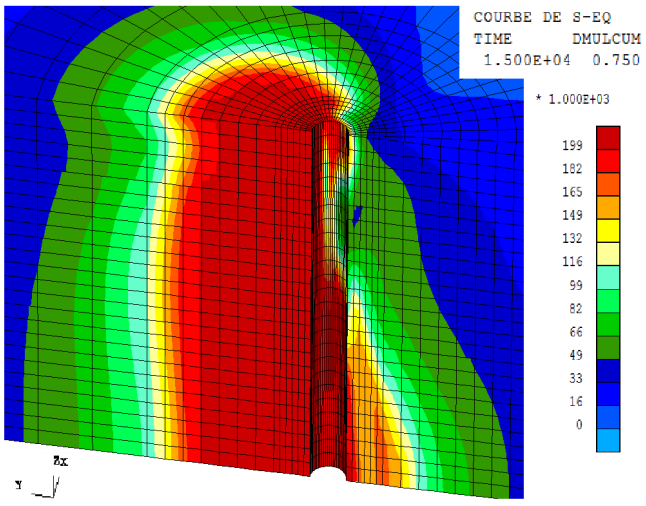

Figure 5.23: case EP2: equivalent stress of Von Mises (Pa) for a 75 cm rigid pile displacement.

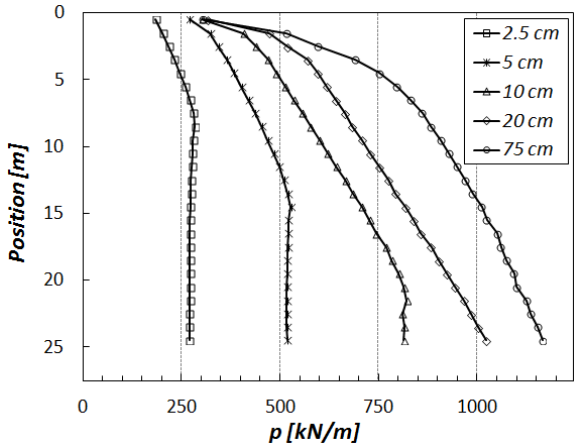

Figure 5.24: case EP3 - *p-z* profile for different rigid pile displacements.

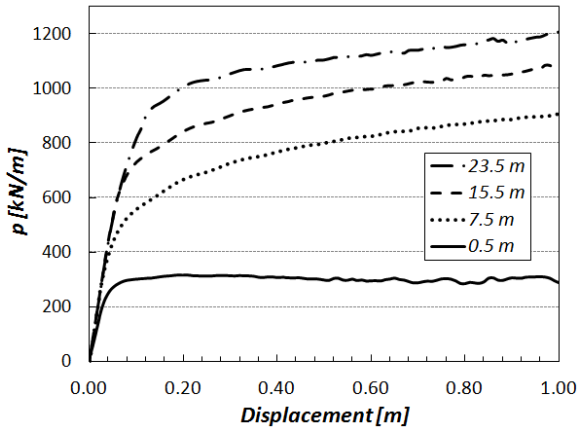

Figure 5.25: case EP3 - *p-y curves* at some locations.

Medium-stiff soil with hardening

For case H2 hardening has been introduced, with a starting cohesion of 10 kPa. As a results the plastification begins at much lower rates of confinement/de-confinement; on the other hand, the deviator keeps increasing even during plasticity, but with reduced rate comparing with the initial elastic regime. This phenomenon can be detected by tracking the distribution of the cohesion - in Figure 5.26 the final value is reached in the most solicited locations.
The tri-linear shape of the *p-z* profile is maintained (Figure 5.27), while the mobilized resistance is lower comparing to case EP3. The p-y curves are showed in Figure 5.28, where a plateau is clearly reached only at shallow depths.

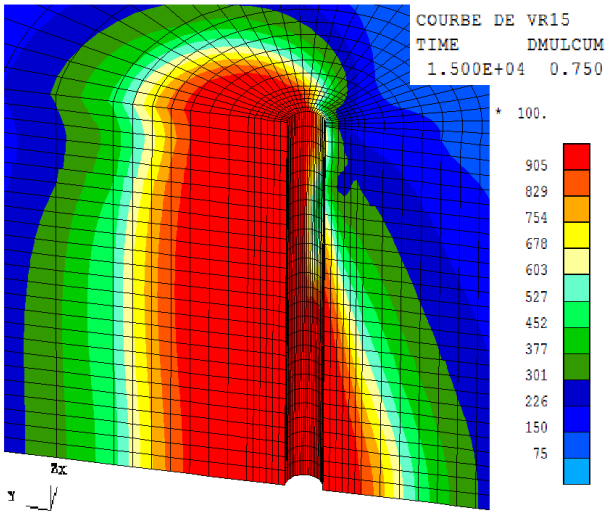

Figure 5.26: case H2 - actualized cohesion value (Pa).

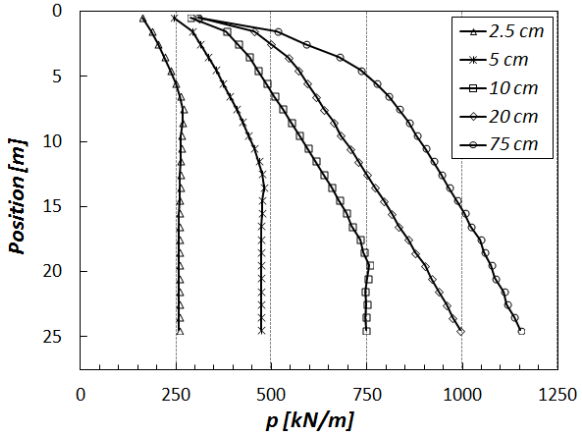

Figure 5.27: case H2 - *p-z* profile for different rigid pile displacements.

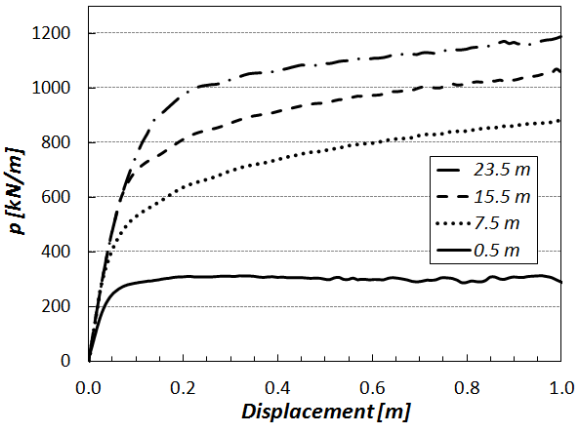

Figure 5.28: case H2 - *p-y curves* at some locations.

A specific analysis on the ultimate lateral resistance will be presented in the next chapter, once defined a full model including hardening, friction and undrained parameters. We will make use of the p-y curves resulting from a rigid displacement as they allow investigating the resistance mobilization at large displacements.

5.3.3 Deflection at the pile head

In the previous section the aim was a solid understanding of the main contributions and physical phenomena appearing in the *p-y curves*. Now the focus moves to a more realistic scenario of a slender monopile charged laterally at its head: this type of model is considered the best for a comparison with existing API-based *p-y curves* formulations - as reported in paragraph 3.3.2.1. The mesh is showed in Figure 5.29 - note that the soil is present also at the base of the structure; soil and pile properties are the same used in the previous mesh (Table 5.2).

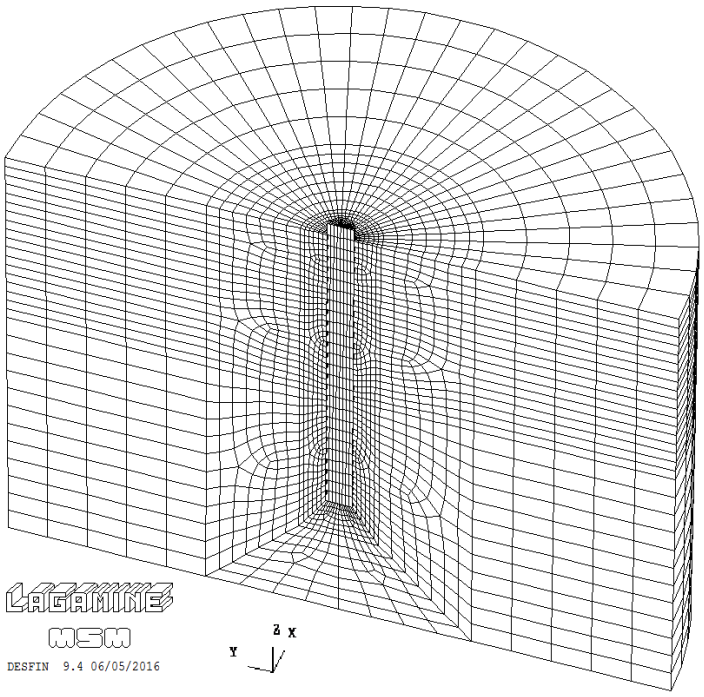

Figure 5.29: mesh for a circular 25×2 m slender pile, solid concrete section with lateral and base soil and interface element.

To simulate a lateral force acting at the mud line, a progressive lateral displacement has been imposed at this location. In particular, for all the nodes part of the 0.5 m-long additional element emerging from the soil (Figure 5.30) we have fixed the y-z coordinates (constant z, increasing y); while this conditions might be not consistent - the head is embedded, as rotations are impeded - we will see that for a slender geometry it does not affect the mechanical behaviour of the system.

The resulting displacement profile is a typical one for slender piles: it is governed mainly by bending, the displacement at the tip is limited and opposite to the solicitation, the rotational point moves downwards for increasing displacements.

We consider case EP2 as presented in paragraph 5.3.1 (E = 20 Mpa, S_u = 100 kPa) - it provides enough complexity to draw further conclusions.

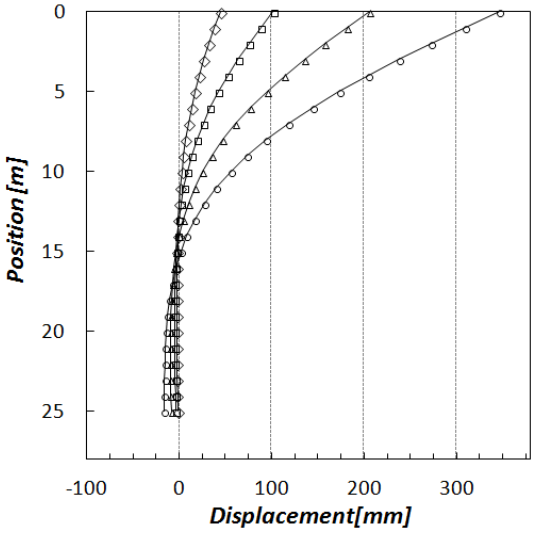

Figure 5.30: main steps of the displacement-controlled path. The position is relative to the pile main fibre, in the direction of the y axe in Figure 5.29.

In Figure 5.31 the deviator distribution shows four different zones of interest, appearing progressively for an increasing mud line deflection: at 2.6 cm the solicitation is concentrated in front of the pile at the mud line and the gap develops; at 23 cm these effects are enhanced and at the base - front and back - two additional zones are detected; the trend is confirmed for a 49 cm deflection. Note that on each side the rotational point is located between the two zones.

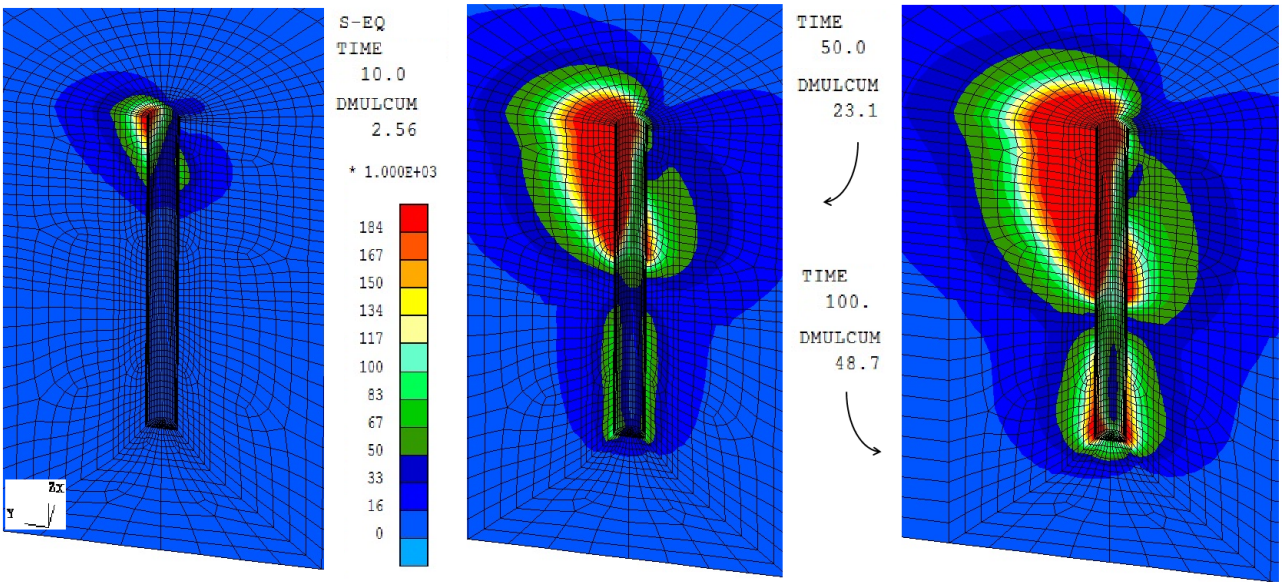

Figure 5.31: case EP2 - equivalent stress of Von Mises (Pa) for a deflection at the mud line of 2.6 cm (left), 23 cm (center) and 49 cm (right).

Similarly, the distribution of the contact pressure at the back interface (Figure 5.32) shows the gap propagation and a concentration at the base; at the front a de-confinement is instead generated, therefore a detachment.

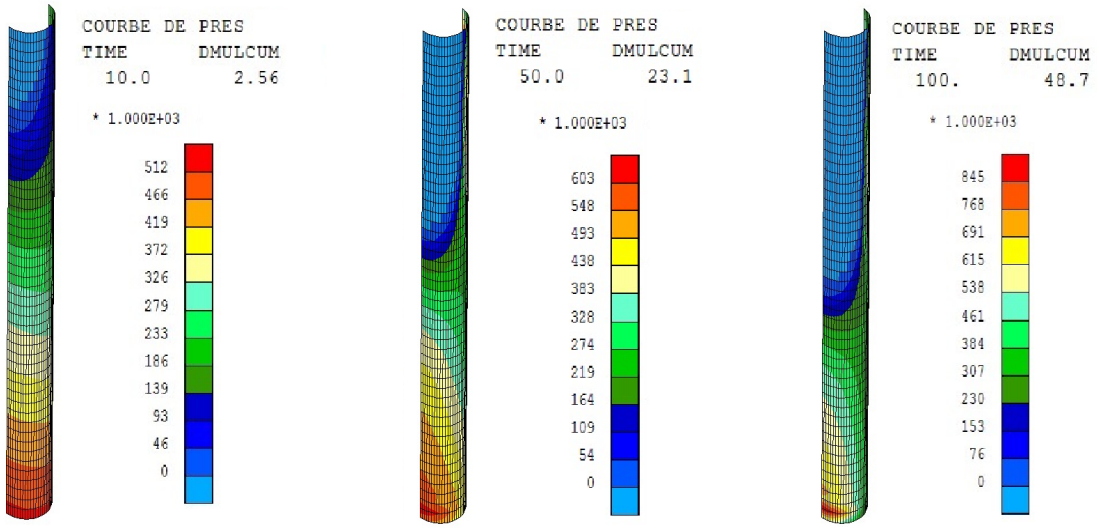

Figure 5.32: case EP2 - contact pressure (Pa) at the back interface for a deflection at the mud line of 2.6 cm (left), 23 cm (center) and 49 cm (right).

Basically, taking the rotational point as reference, in the zone above and below gap and detachment develop in the form of a *chasm* - top front (back) similar to bottom back (front). Therefore, as in Figure 5.5 of paragraph 5.3.1.1, we may simplify the solicitation and the evolution of the stress state as presented in Figure 5.33. Note the similarities with the resulting p-z profile of Figure 5.34a.

Nonetheless some perturbations are detected, due at first to the geometrical simplifications on the deformation distribution - in Figure 5.30 the perfect triangular shape can be assumed only for low

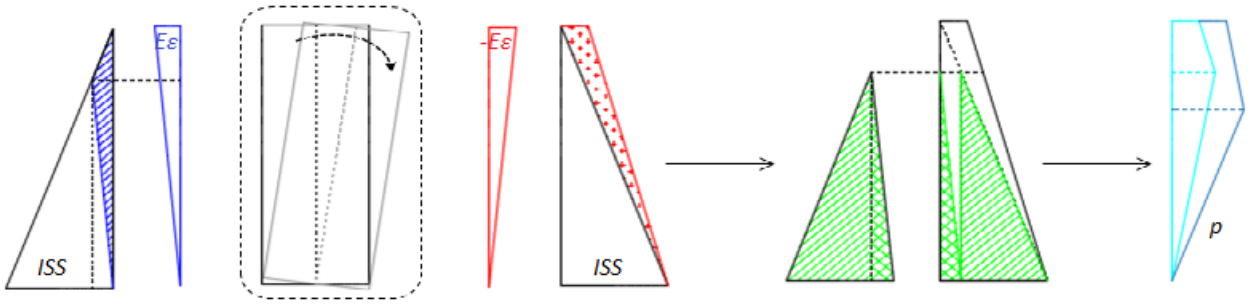

Figure 5.33: evolution of the stress state for a rotated pile - tip as rotational point: de-confinement at left, confinement at right. Resulting lateral pressure distribution, with gap extension, for two different solicitations.

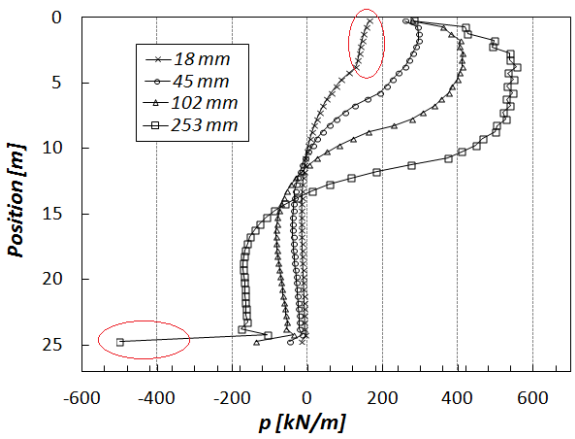

(a) *p-z* profile for different mud line displacements.

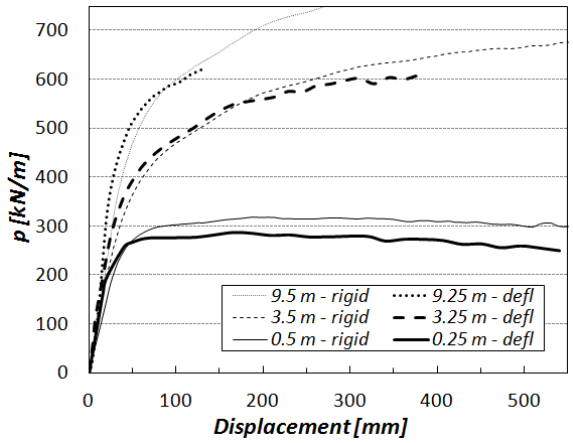

(b) *p-y curves* at shallow depths, for pile rigid displacement and mud line deflection.

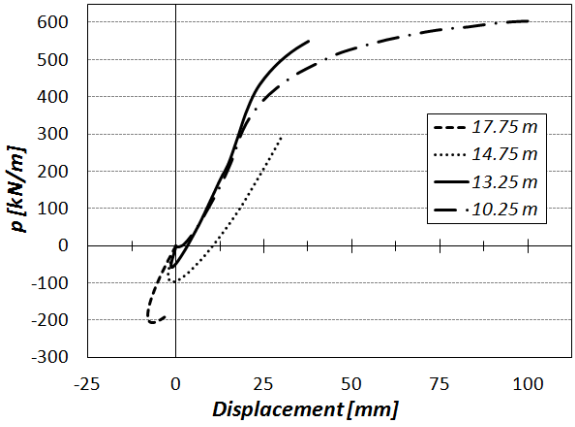

(c) *p-y curves* at medium depths.

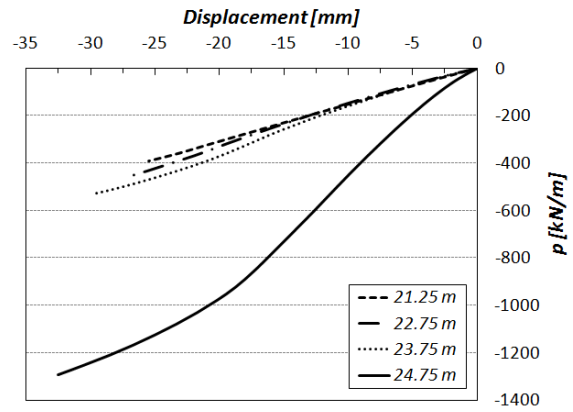

(d) *p-y curves* around pile tip and base.

Figure 5.34: case EP2 - profiles of pressure and *p-y curves* (where not specified, for mud line deflections).

deflections; in addition, a slight mud line effect (at 18 mm) and plastification are detected; below the rotational point the distribution is *pretty much* maintained, while the peak at the pile tip represents the additional base resistance.

As expected, the resistance is not homogeneously mobilized all along the pile. In terms of *p-y curves* (Figure 5.46) we identify three characteristic zones in depth: at shallow depths (< 10 m) a *classic* elasto-plastic response is detected, very similar to the rigid displacement case; around the rotational point (10-to-20 m) the curves are perturbed - not monotonic and/or with marked change of concavity; around the pile tip (> 20 m) the response is consistent within the different locations and mainly elastic, while elasto-plastic at the base. This last curve may be exploited by calibrating the 1D model, e.g. by fitting an hyperbolic tangent function.

In the final chapter a more complex soil constitutive law will be included, in order to compare the 3DFEA results with the models by API/Matlock (1970) and Jeanjean (2009) props. When possible, a preliminary comparison will be based on the *p-y curves* extracted close to the mud line and at the pile base, while a full characterization of the system response will be provided by the applied lateral force as function of the resulting mud line lateral displacement.

In Figure 5.35 the applied head condition (embedded pile) is compared in terms of *p-y curves* with a hinge-like condition. In this second case, at the emerging element we have fixed the y-z coordinates only of nodes resting on the radial plane parallel to the x-axe; this is more consistent with the real case of laterally loaded pile for offshore wind turbines, as at the mud line the structure withstands both rotations and lateral displacements.
Note that the curves correspond almost perfectly. Further analysis have established that the embedded head model results, as expected, in an overestimation of the mobilized resistance; however, this effect is very slight and detected only for very large deflections, therefore negligible.
On the other hand, this is not the case for large piles, for which their tendency to avoid bending, due to the important inertia, is such that the hinge condition must be preferred.

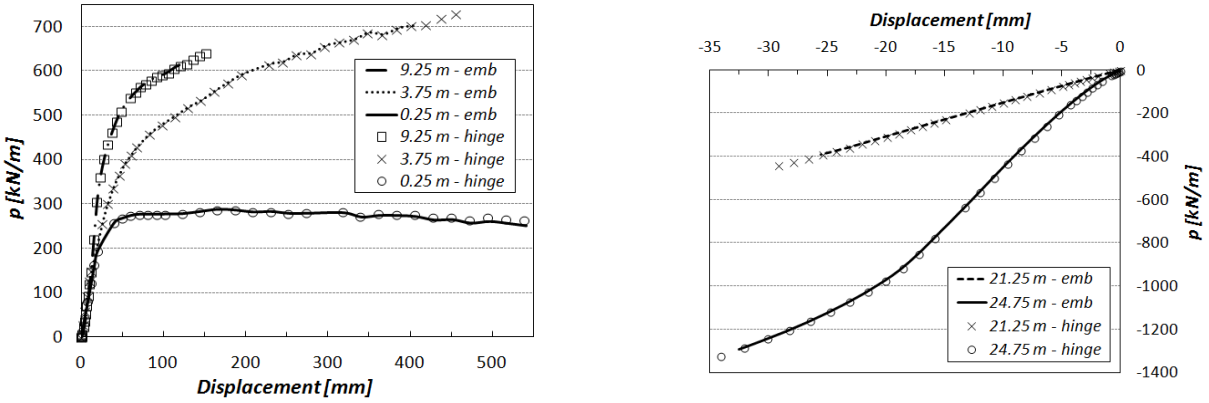

Figure 5.35: case EP2 - *p-y curves* for increasing mud line deflections, with embedded head or hinge, at shallow (left) at large depth (right).

5.3.4 Conclusions

The sensitivity analysis conducted with a simplified model - rigid displacements and no soil at base - has highlighted the main phenomena contributing to the lateral response of the soil: effects of the initial stress state, detachment and gap propagation at the pile back, bump at the front (mud line effect). In addition, the initial slope of the *p-y curves* results to depend on the elastic parameters of the soil and on interface friction: it can be evaluated (and validated) in terms of coefficient of subgrade reaction by means of analytical solutions.
Then, plasticity provides the typical shape to the curves; on the other hand, while at some locations - soil under triaxial (de)compression - we have recognize ultimate conditions, the overall ultimate behaviour requires further studies. In fact the plateau in the curves has been detected only in some cases at shallow depths, while elsewhere the mobilized resistance keeps increasing at large displacements and depends on elastic parameters; therefore there is no clear evidence of a ultimate resistance value. An advanced analysis can be based on the stress state investigation at relevant locations.

The full model - soil at the base, deflection at the mud line - has highlighted the typical bending behaviour of slender piles and, even if limited, the additional component of resistance at the base. Due to the different solicitation, the *p-y curves* are more perturbed, in particular at medium depths. Still, at the base they are suited for a calibration and at shallow depths for comparisons with standard formulas still.
Finally, the two boundary conditions at the pile head - hinge and embedded pile - provide very similar results, due to the behaviour mainly governed by bending.

5.4 Large Pile

In this section we consider a family of piles whose slenderness (L/D) is lower than 5, commonly defined short or large piles. In terms of *p-y curves*, the phenomena observed for the slender pile are generally detected with this new geometry as well; nonetheless additional effects can be identified.
Similarly to the slender pile case, we present a model for a large pile deflected at the mud line, with a hinge condition at the pile head. At first only the lateral soil response is investigated, then the soil at the base is included as well. Simple elasticity coupled with friction at the interface helps to highlight phenomena typical of short piles, while the proposed constitutive law with hardening is assumed valid for clays. The soil parameters for the different cases are reported in Table 5.4 and 5.5 - note that we tend towards an undrained Poisson's ratio.
The pile is modelled as a caisson, with a large tubular section. This technological solution is definitely the most common for piles with large diameters: it is usually made of steel, with a wall thickness equal to ca 1% of the diameter. The parameters are reported in Table 5.6: note that the material is concrete, unrealistic for hollow sections. The choice was obliged, as a high Young's modulus caused non-convergence issues in LAGAMINE, especially when coupled with a high Poisson's ratio, which we were not able to fix. However, we will see that this does not compromise the modelling.

ν (-)	B_c (-)	γ_s (N/m$_3$)	K_0 (-)
0.4	0.001	20725	1

Table 5.4: invariant soil parameters - from left to right: Poisson's ratio, hardening coefficient, volumic weight, coefficient of lateral pressure.

case	E (MPa)	$S_{u,I}$ (kPa)	$S_{u,F}$ (kPa)	ϕ ($^\cdot$)
ESt	20	∞	∞	0
ESt-F	20	∞	∞	20
ESo-F	2	∞	∞	20
H-F	20	10	100	20

Table 5.5: soil parameters for each case - from left to right: Young's modulus, initial and final undrained shear strength, friction angle at the interface.

$L\times D$ (m×m)	t (cm)	E (GPa)	ν (-)	κ_P (Pa)
24×8	8	20	0.3	10^9

Table 5.6: pile parameters - from left: lenght, diameter, wall thickness, Young's modulus, Poisson's ratio, interface penalization factor.

5.4.1 Lateral soil response

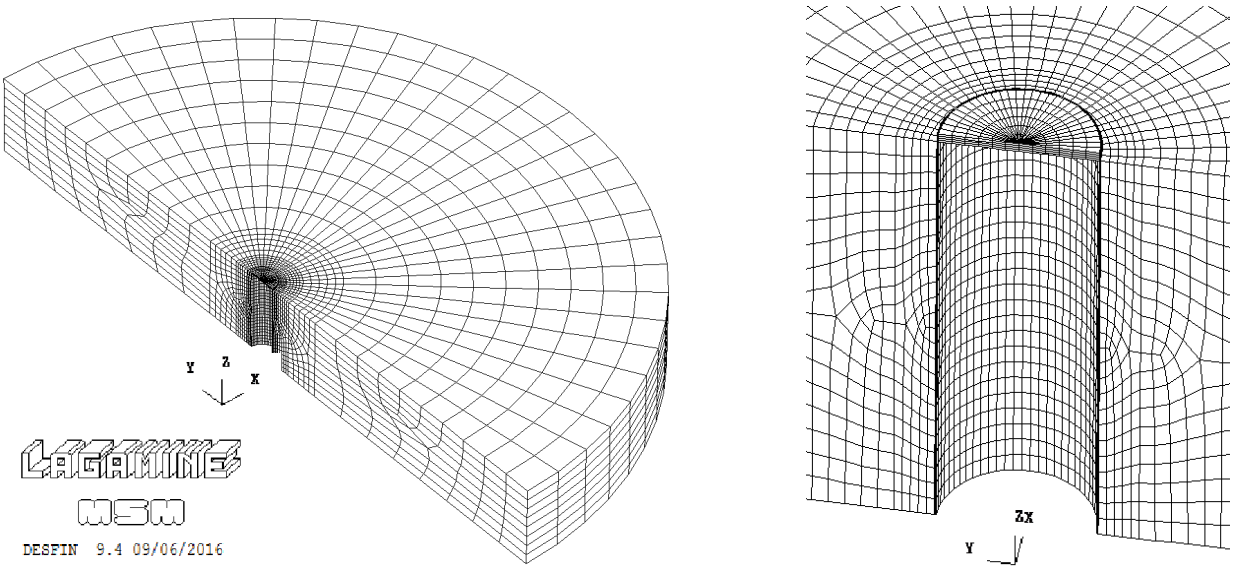

Figure 5.36: mesh for a circular 24×8 m large pile, hollow concrete section with lateral soil and interface element.

The first mesh is showed in Figure 5.36, where only a lateral homogeneous soil layer is included - no inner and base soil - and the emerging additional element. Half of pile and soil are modelled, assuming symmetry with respect to plane y-z.

5.4.1.1 Medium-stiff soil

The increasing deflection at the mud line is realised by means of the hinge condition at the head - fixed y-z coordinates of the nodes resting on the radial plane parallel to the x-axe. For case ESt - elastic, medium-stiff soil - this results in the deformed pile of Figure 5.37.
The high flexural rigidity, due to the large section, is such that the pile undergoes an almost rigid rotation, whose rotational point is located in the second half of the pile and the lower portion moves backward, *kicking*. The profile of pressure is showed in Figure 5.38: note the similarities with the distribution of Figure 5.33 - gap propagation - in particular for small deflections. Moreover, along with the mud line effect - additional resistance mobilized at shallow depths, already detected for the slender pile (paragraph 5.3.1.1) - we register a concentration of deformations at the pile back close to tip, with the mobilization of further resistance. Both the effects increase with the solicitation.
In elasticity the *p-y curves* are perturbed and do not show further features of interest; they are presented once hardening is included.

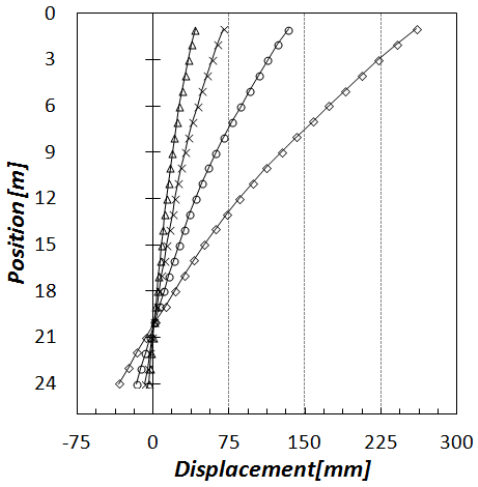

Figure 5.37: large pile profile for increasing head deflection, case ESt - position relative to the pile main fibre, in the direction of the y axe in Figure 5.36.

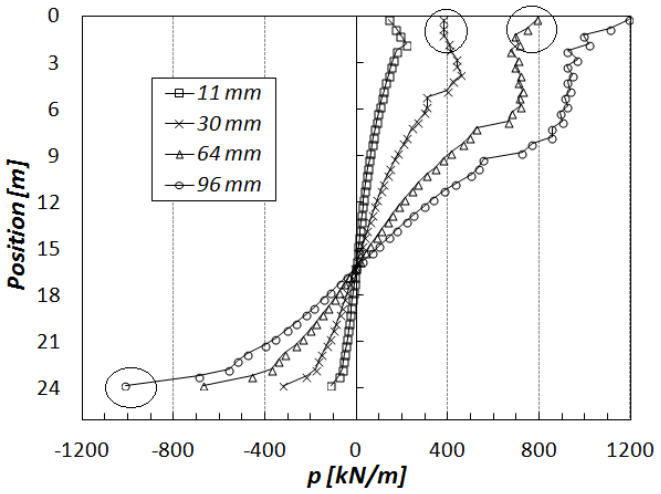

Figure 5.38: large pile, case ESt - p-z profile for different mud line deflections. Effects at mud line and tip highlighted.

5.4.1.2 Soft soil with interface friction

A comparison between case ESt, ESt-F and ESo-F is now presented, to analyse the effects of soil stiffness and friction at the interface. For a mud line deflection of 98 mm, the three deformed profiles are showed in Figure 5.39: note that, once friction is introduced (ESt-F), in absence of base resistance limiting the base lateral movement the pile tip withstands positive displacements. With a softer soil (ES0-F), the rigid behaviour of the pile is enhanced, but the base is still *dragged* and it is identified as the rotational point.
In other words, while, as expected, the relative flexural stiffness of soil and pile provides (or not) the rigid behaviour, the mobilized friction at the pile lateral surface resists to the lower pile portion tending to move upward - the *kick*. The same effect appears in the upper portion as well, in terms of resistance (Figure 5.40): in fact, for case ESt-F, along with an enhanced mud line effect, the pile moving downward mobilizes additional friction resistance. This can be seen in the distribution of shear stresses at the interface (Figure 5.41a). Furthermore, note that in case ESt-F and ESo-F at the lower portion the mobilized pressure is negative even if the displacement is positive, meaning that here the pile pushes back more than the soil resists at the front (Figure 5.41b).

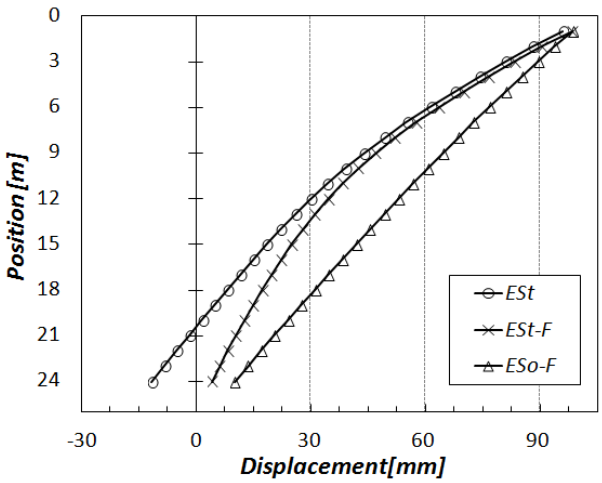

Figure 5.39: large pile profile for a 98 mm mud line deflection, three elastic cases.

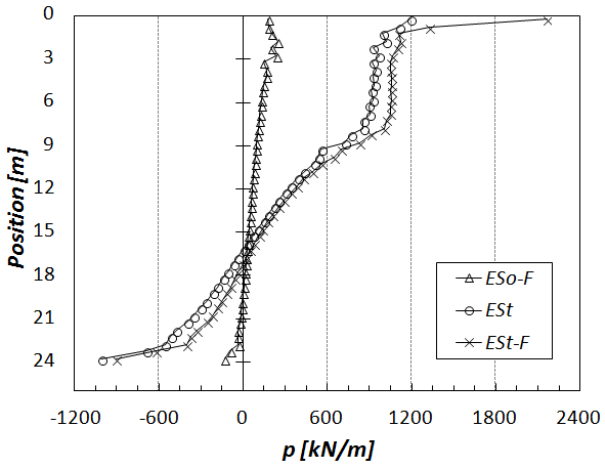

Figure 5.40: large pile, three elastic cases - p-z profile for a 98 mm mud line deflection.

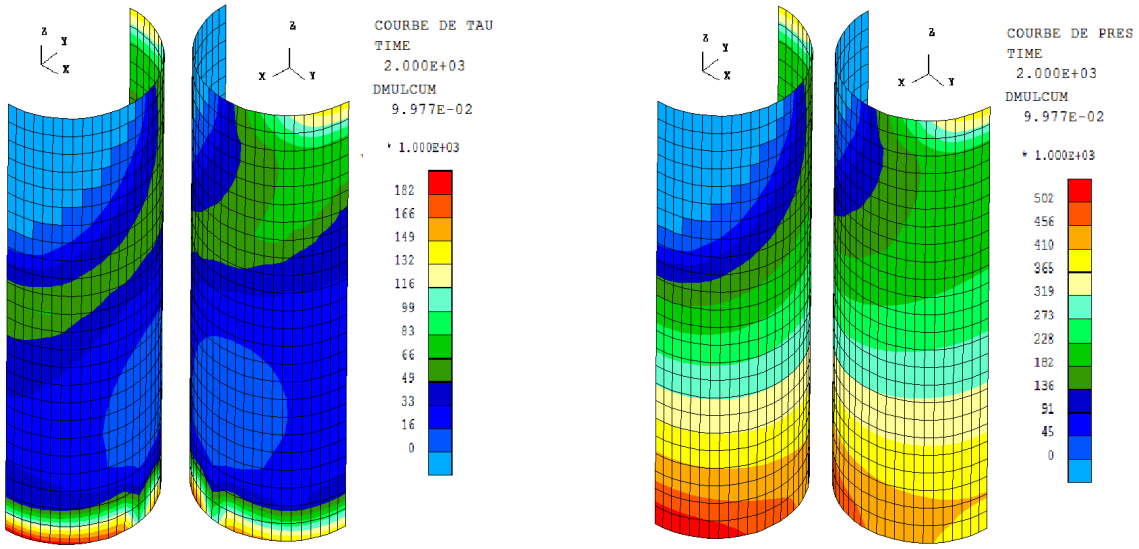

(a) Shear stress (Pa) at back (left) and front (right) (b) Normal pressure (Pa) at back (left) and front (right)

Figure 5.41: large pile - variables at the soil-pile interface for a 10 cm mud line deflection

This phenomenon can be taken into account in a 1D model by applying some modifications to the standard model of chapter 4 (Figure 4.1): in fact, the horizontal springs represent the soil stiff lateral response - along with the components of friction in the horizontal plane - and resist (only) to lateral movements; additional elements could be added in order to limit the vertical displacements[3]. As in 1D the vertical dimension is not included, in alternative we may make use of a series of rotational springs all along the pile, as proposed in Figure 4.2.

Further simulations with the slender pile showed these effects having a lower impact, at least in the lower portion of pile, as the overall behaviour is governed mainly by bending; in addition, note that with larger sections the lateral pile surface increases, with friction playing a bigger role. For these reasons, we believe that rotational springs may be required especially for short-large piles.

[3]Note that if we consider simply a lateral rigid displacement, no component of friction is mobilized in the plan y-z; similarly, if the displacement is purely vertical, friction in the only resisting component.

5.4.2 Lateral and base soil response

Starting from mesh of Figure 5.36, soil at base and inside the caisson are added, obtaining a geometry very close to large piles adopted in reality (Figure 5.42). Pile and soil parameters are the same as for the previous model (Table 5.4 and 5.6) and we consider case H-F of Table 5.5, representing a hardening law for a medium-stiff clay.

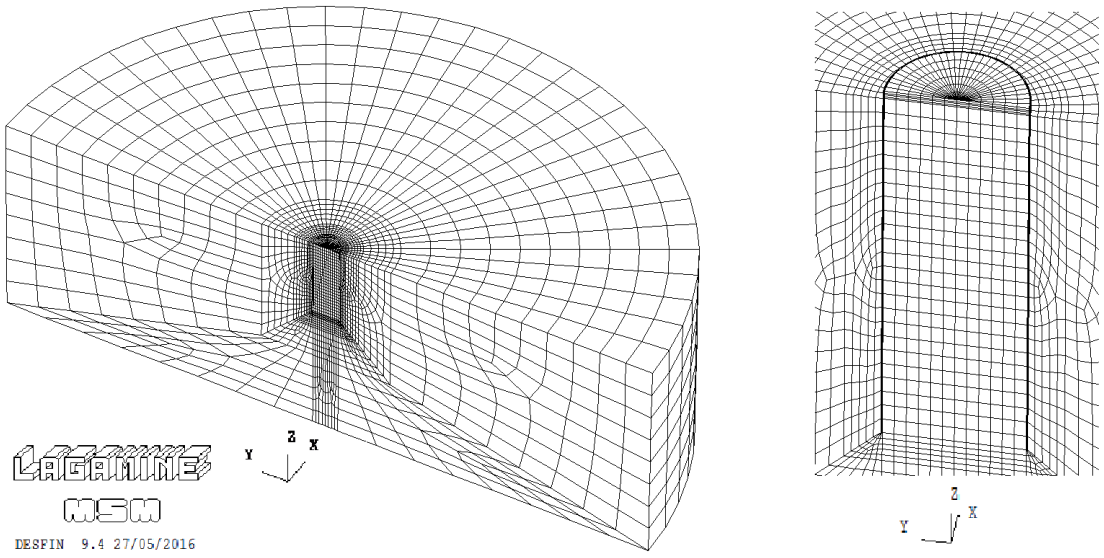

Figure 5.42: mesh for a circular 24×8 m large pile, hollow concrete section with lateral, base and inner soil and interface element.

An increasing deflection at the mud line is applied by means of a hinge condition at the pile head; the resulting deformed profile is showed in Figure 5.43, presenting the typical (almost) rigid rotation with the *toe-kick*.

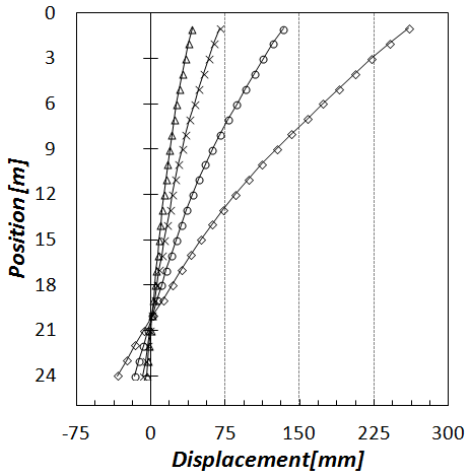

Figure 5.43: large pile profile for increasing head deflection. The position is relative to the pile main fibre, in the direction of the y axe in Figure 5.42.

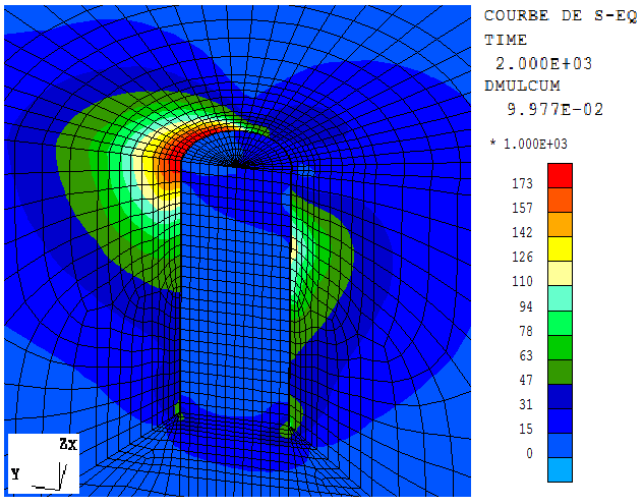

Figure 5.44: large pile under a 10 cm mud line deflection - equivalent stress of Von Mises.

The results from *Desfin* are then presented. The observations made for the slender case in paragraph 5.3.3 are still valid - 4 zones of solicitation in the outer soil and pressure concentration at the base (Figure 5.44). In addition, the inner soil displacement highlights the plane of rotation (Figure 5.45a), which corresponds to the mean fiber as long as the behaviour is rigid; the outer lateral soil moves downward (upward) as is pushed by the first (second) portion of pile - as mentioned, this

mobilizes a component of friction in the plane *y-z*. Finally, the soil at the base, working as a plug, withstands important solicitations, mainly shear-related (Figure 5.45b).

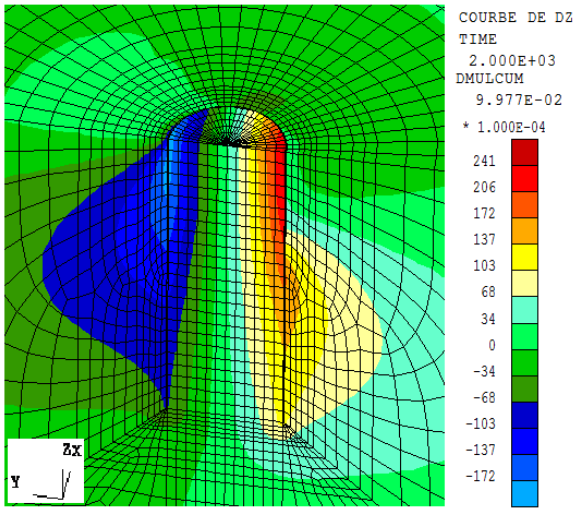

(a) Vertical soil displacement - inner and outer.

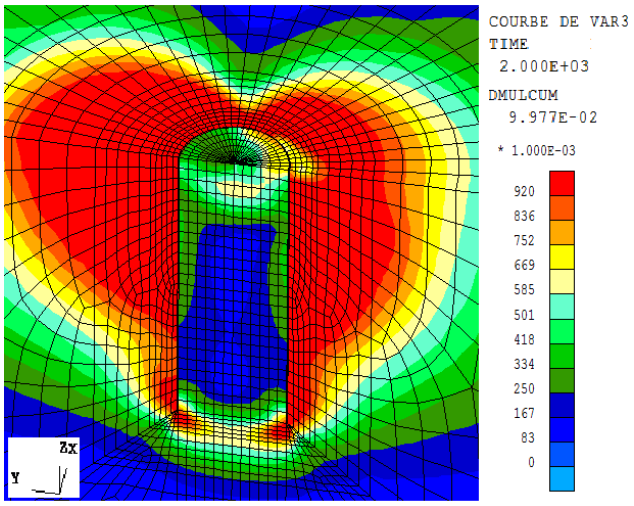

(b) Plasticity rate.

Figure 5.45: main variables for large pile under a 10 cm mud line deflection.

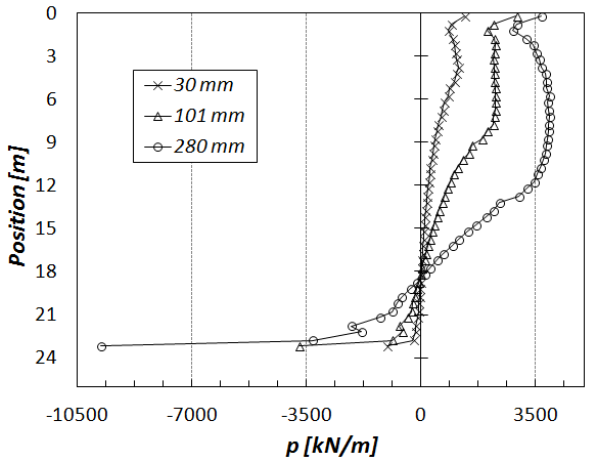

(a) *p-z* profile for different mud line displacements.

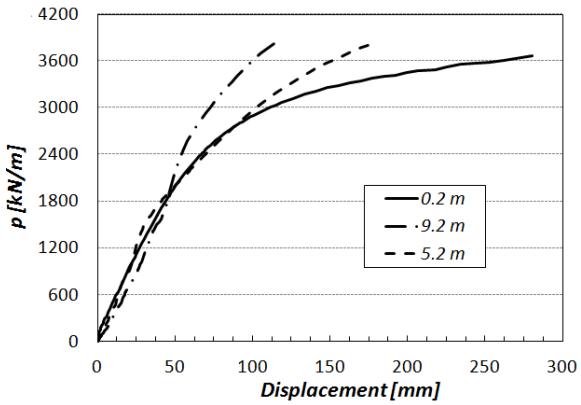

(b) *p-y curves* at shallow depths, for pile rigid displacement and mud line deflection.

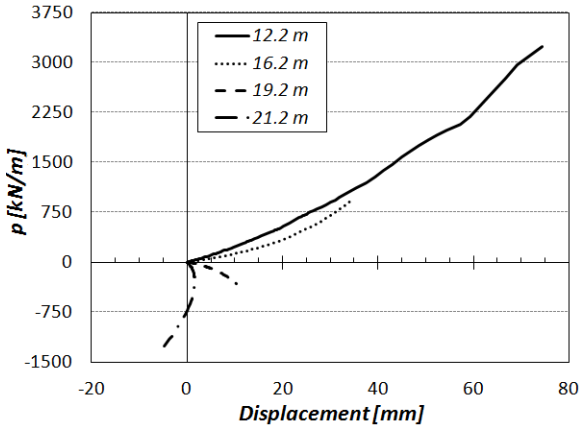

(c) *p-y curves* at medium depths.

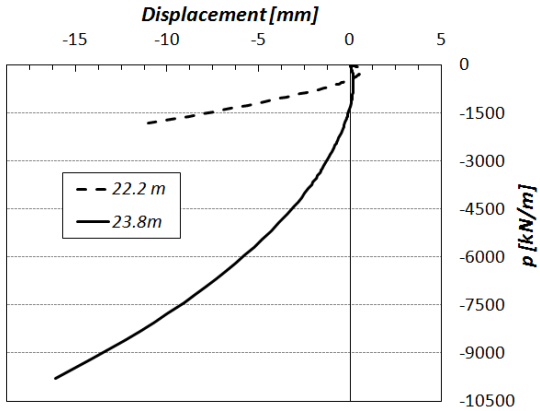

(d) *p-y curves* around pile tip and base.

Figure 5.46: large pile - profiles of pressure and *p-y curves* (where not specified, for mud line deflections).

The *p-z* profiles are reported in Figure 5.46a: we identify many of the phenomena described so far - gap propagation leading to a distribution as in Figure 5.33 for small deflections, while plasticity appears at large; additional resistance at shallow depths (mud line effect) and at the base (plug).
As for the slender pile deflected at its head, the *p-y curves* are perturbed at medium-to-large depths, while showing the typical decreasing slope at shallow depths - above 10 m - and at the tip. In particular, the curve extracted at 23.8 m could be the starting point for the calibrated base resistance function (*B-y curve*).

5.4.3 Conclusions

Many of the effects detected for the slender pile have been identified for the large pile as well, while in this second case a (mainly) rigid behaviour characterizes the structure. In addition, the simplified model - no soil at the base and inside the caisson - have remarked the coupled effects of relative flexural rigidity and friction: e.g. the pile tip tends to move simultaneously backward and upward (*toe-kick*), with the soil reacting both vertically and laterally. We believe that this coupling is particularly enhanced in large piles, as the lateral surface is larger.
With the full model we have observed the effect of the plug, resulting in a well-shaped *B-y curve*, suited for calibration.

In the end, with reference to the standard model of chapter 4, we believe that the lateral springs alone do not suffice to properly represent the overall soil response: in particular, along with the mentioned and already implemented base shear term, rotational springs are required to traduce the vertical resistance all along the pile.

-

Chapter 6

P-Y Curves for Monopiles in Soft Clay

6.1 Introduction

In this final phase of analysis, we proceed to study a realistic case of a monopile under lateral monotonic loading in soft clay. The aim is to compare the existing method of characterization of the lateral response with the 3D results based on the models previously introduced. At first, we focus on the evaluation of the API/Matlock (1970) method (paragraph 3.3.2.1), which currently is the main reference when designing offshore foundations; on the other hand, as we expect this method to have some limitations - underestimation of the soil stiffness response - we also consider the *p-y curves* proposed by Jeanjean (2009), in particular in the proposed discretized form. This curves are thought to be good candidates to replace the API ones and might be the base for updated norms, which, in the near future, may provide new guidelines for the offshore industry, resulting in important technological improvements. Although the main goal of the paper is not the formulation of *our own* curves, nonetheless we will provide some useful indications based on the 3D simulations, mainly as proposals for further analysis.
The comparison is conducted by means of the curves extracted from the 3D models of chapter 5 and the calibrated 1D model of chapter 4, in terms of *p-y curves* and evolution of the lateral force at the mud line, for both a slender and a large pile.

6.2 Soil Properties

The existing methods - API/Matlock (1970), Jeanjean (2009) - propose families of p-y curves to be used ideally with soft clay, defined as those soils with an undrained shear strength less than 100 kPa [41]. Therefore we will investigate two cases, respectively with a 100 kPa and 50 kPa cohesion. In addition, we will assume undrained conditions, while neglecting pore water pressures; a typical half-failure deformation ε_{50} of 1%; a hardening law. In particular this law will be adjusted to simulate both the large-strain and small-strain behaviour.
In Table 6.1 and 6.2 we report respectively the common parameters and the variant parameters for the two cases.

ν (-)	B_c (-)	$B_{c,0}$ (-)	γ (N/m$_3$)	K_0 (-)
0.45	0.001	0.007	20725	1

Table 6.1: soil common parameters - from left to right: Poisson's ratio, hardening coefficient for large and small-strain strain, volumic weight, coefficient of lateral pressure.

case	E (MPa)	E_0 (MPa)	$S_{u,I}$ (kPa)	$S_{u,F}$ (kPa)
SC1	10	50	10	100
SC2	5	25	5	50

Table 6.2: soil parameters for each case - from left to right: Young's modulus for large and small-strain, initial and final undrained cohesion.

6.3 Slender Pile

The parameters for a solid section, slender pile are reported in Table 6.3. The Young's modulus value is adjusted to simulate a hollow steel section 2 cm thick.

$L \times D$ (m×m)	E (GPa)	ν (-)	ϕ_{intf} (^{o})	κ_P (Pa)
25×2	8.1	0.3	20	10^9

Table 6.3: pile parameters - from left to right: lenght, diameter, Poisson's ratio, Young's modulus, interface friction angle and penalization factor.

In the next paragraphs we present the analysis, in which both the rigid and the deflected models (Figure 6.1) are to be used, as they provide interesting 3D results in terms of ultimate resistance and stiffness response. Note that the presented values of resistance and lateral force have been multiplied by two, as the models of chapter 5 account for only half of soil and pile.

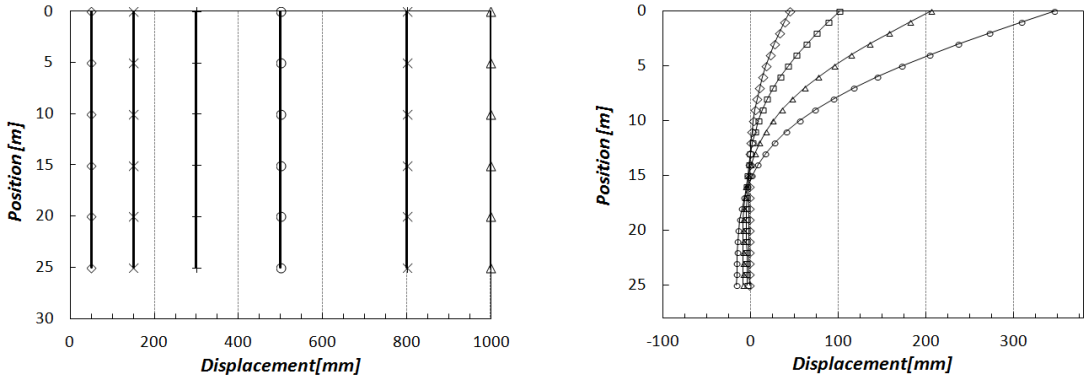

Figure 6.1: slender pile - typical phases of pile rigid displacement (left) and deflection at mud line (right), this last obtained with hinge condition at the pile head.

6.3.1 Ultimate resistance

The curves for a pile rigid displacement in case SC1 are showed in Figure 6.2: as mentioned in pararaph 5.3.3 (Figure 5.34b), these curves are similar to the ones resulting from a deflected pile for similar displacement paths; in addition, they allow to register homogeneously the resistance mobilization in depth, therefore introducing the notion of ultimate resistance.

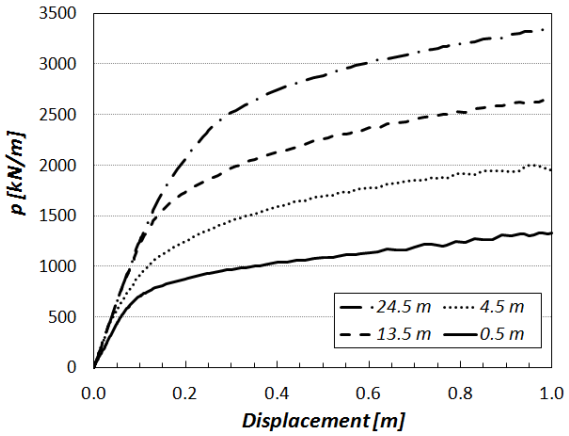

Figure 6.2: slender pile, case SC1 - *p-y curves* for different pile rigid displacement.

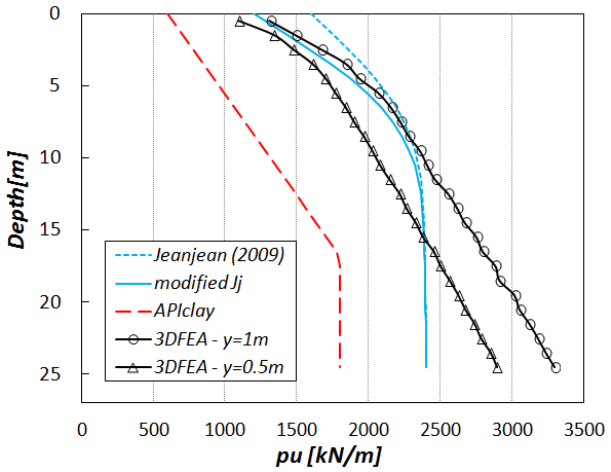

Figure 6.3: slender pile, case SC1 - depth profile of ultimate soil resistance after API/Matlock (1970), 3DFEA, Jeanjean (2009) and proposed modification.

Even if a plastic plateau is not reached, we may identify its value by targeting a displacement assumed *very large*, e.g. 0.5 m or 1 m - equal to 10 or 20 times y_c =0.05 m.
By comparing the resulting distribution at 1 m of displacement with the lateral bearing capacity profile after API/Matlock (1970) (Figure 6.3), we conclude that the norm underestimates the soil capacity. On the other hand, although a slight overestimation at shallow depths, Jeanjean (2009) provides a more accurate prediction - more in depth we assume it on the safe side rather than underestimating. In this approach, we propose a modification to the lateral bearing capacity factor of equation 3.19, obtaining:

$$N_p = 12 - 6e^{-\varepsilon z/D} \tag{6.1}$$

Basically we maintain the given shape, while assuming at the mud line a minimum value of resistance of 6 times the cohesion - times D - instead of 8. The modification fits good also for case SC2 (Figure 6.4 and 6.5).

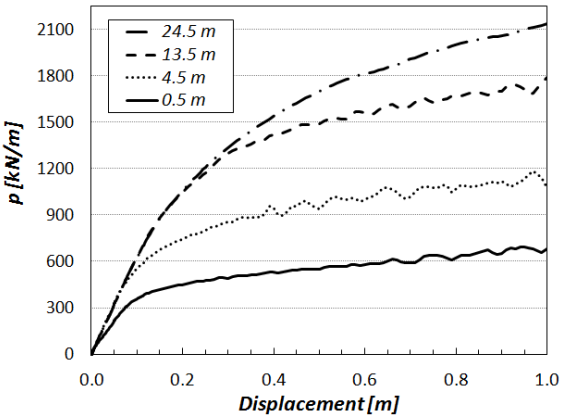

Figure 6.4: slender pile, case SC2 - *p-y curves* for different pile rigid displacement.

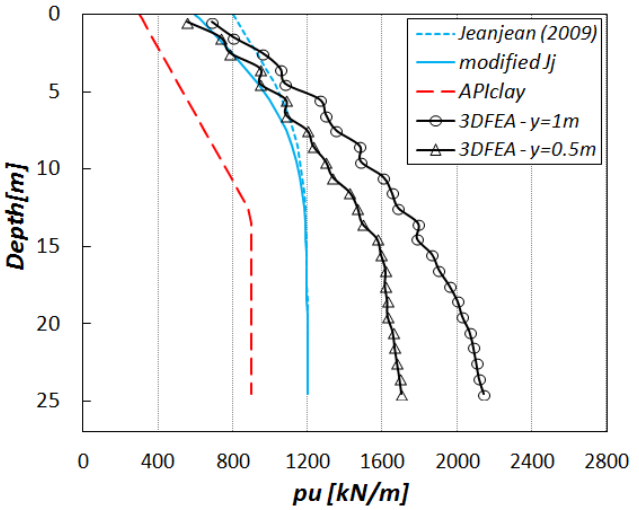

Figure 6.5: slender pile, case SC2 - depth profile of ultimate soil resistance after API/Matlock (1970), 3DFEA, Jeanjean (2009) and proposed modification.

However this formulation is a first attempt and requires further analysis - the assumption of ultimate conditions at 1 m is indeed to be confirmed; in addition, note that neither the soil at the base nor a deformed pile are taken into account. Still, it allows to evaluate in a more direct way the stiffness response predicted by Jeanjean (2009).

6.3.2 Stiffness response

Large-strain behaviour

We consider case SC1, with a large-strain Young's modulus of 10 MPa and a standard hardening coefficient of 0.001. The *p-y curves* for deflections at the mud line are showed in Figure 6.6: as expected, they are well shaped above 10 m, perturbed below - here highlighted the locations at shallow depths and close the pile tip.

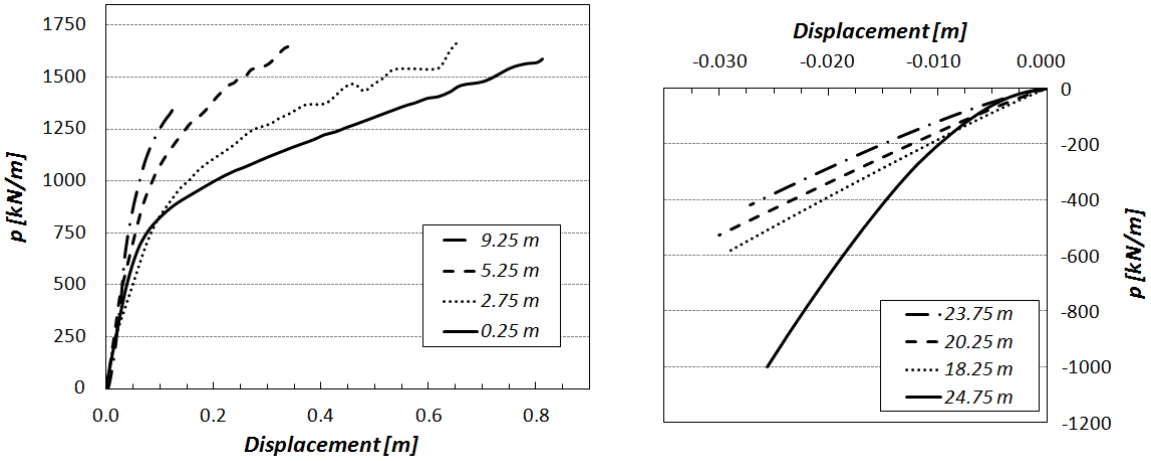

Figure 6.6: slender pile, case SC1 - *p-y curves* for different mud line deflections at different locations.

A comparison based on the curves at the mud line is presented in Figure 6.7: note that for medium-to-large displacements - larger than 0.02 m, corresponding to ε=0.16% - the API formula underestimates the stiffness response, while the modified Jeanjean (2009) curve with G_{max}/S_u=400 fits good for y >0.05 m (ε=ε_{50}=1%). On the other hand, for small displacements the 3D simulation underestimates the response: in particular we remark that API and Jeanjean curves are such that the first slope of the discretized form - first two points (y=0 m and 0.05 m) - results to be much stiffer than our prediction. We believe this is due to the fact that we have not included a small-strain stiffness component in the constitutive law. Similar conclusions have been drawn for case SC2 as well.

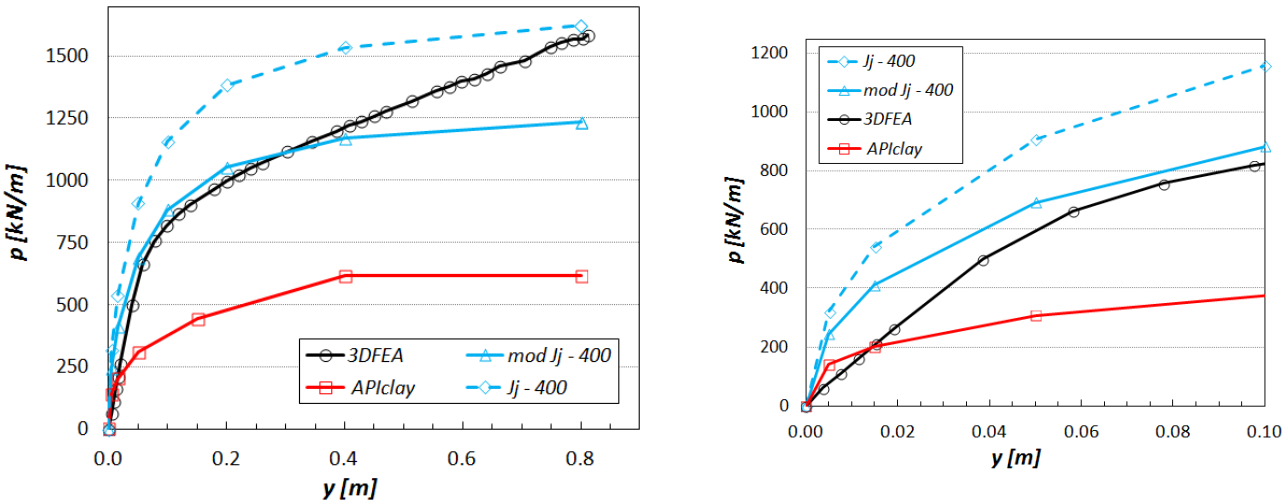

Figure 6.7: slender pile, case SC1 - *p-y curves* at 0.25 m depth for mud line deflections.

Nonetheless, it is not trivial that the same comparison at different depths would lead to similar results. So, instead of investigating all the locations - which may be complex as the extracted curves tend to be more perturbed - we can evaluate the overall response along the pile by tracing the force

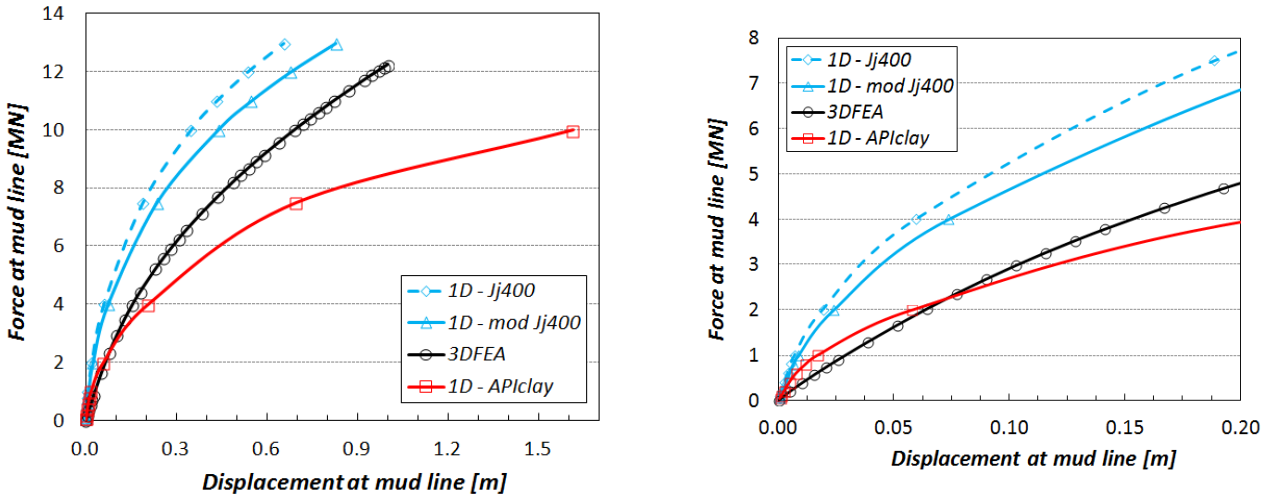

Figure 6.8: slender pile, case SC1 - force in function of the deflection at mud line, in 3DFEA and 1D model calibrated with API/Matlock (1970), Jeanjean (2009) and proposed Jeanjean modification.

at the mud line in function of the corresponding deflection [1]. In particular, we have calibrated the 1D model[2] with the API and Jeanjean formulations. In Figure 6.8 we note that API overestimates the resistance for y <0.07 m while the modified Jeanjean for all the deflections. This can be explained by the fact that in depth the soil response in mainly a small-strain one, as the pile withstands lower displacements.
We conclude that in terms of large-strain behaviour, the API *p-y curves* underestimate the stiffness response, while Jeanjean curves - 2009 and modified - overestimate it. In addition, a further characterization of the small-strain response is required.

A better comprehension of this response may start with the estimation of the coefficient of subgrade reaction ($\times D$) in the large-strain response: by proceeding as presented in paragraph 5.3.1.2, we focus on the *p-y curves* for rigid displacements (Figure 6.2 and 6.4) and we assume the initial slope at 24.5 m depth as representative all along the pile. The obtained value can be compared with the existing analytical methods, where we assume $E = E_0$. The results for case SC1 and SC2 are reported in Table 6.4: note that the 3D results are consistent with the analytical formulations and the best estimation is given by Meyerhof&Baike. In paragraph 5.3.1.2 Selvadurai fitted better, as we targeted a different slope - the *second* one.

case	Biot	Meyerhof & Baike	Vesic	Selvadurai	Klopple & Glock	3DFE
SC1	7.44	12.54	5.56	8.15	13.79	12.5
SC2	3.45	6.27	2.62	4.08	6.90	6.4

Table 6.4: coefficient of subgrade reaction multiplied by the diameter (MPa): comparison between analytical methods of paragraph 5.3.1.2 and 3DFEA - large-strain behaviour ($E = E_0$) for case SC1 and SC2.

Small-strain behaviour

The reaction of soils to small displacements is usually modelled by including a small-strain shear modulus G_{max}: it provides a stiffer initial response, then followed by a stiffness degradation which depends on shear deformations[45] - note that Jeanjean (2009) formula accounts for this phenomenon. In lack of such a constitutive law to impose in the 3D simulations, we may simulate this behaviour by fixing a small-strain Young's modulus E_0 combined with a modified hardening phase.

[1] In a way, this is equivalent to the analysis of the pile deformed profile (e.g. Figure 6.1), while this last does not provide immediate informations - apart from the mud line displacement. On the other hand, we will see this might not be the case for the large pile case

[2] 1D model as defined in chapter 4, with only lateral springs - no terms of base resistance.

Examples for the value of E_0 in sands are given by Pendergast (2016)[46], which proposes to increase the large-strain modulus by ca 3 times. In addition, as mentioned, the first slope of the API *p-y curves* in the discretized form can be taken as a reference and identified as the coefficient of subgrade reaction k_s multiplied by the diameter: in particular it is equal to $2.3p_u/y_c$, therefore presenting a profile in depth similar to the ultimate resistance. For case SC1 we show the distribution in Figure 6.9: note that, by introducing the definition of $p_u = 3S_u$ at the mud line and $y_c = S_u/E$, we obtain 27.6 MPa ($2.76\times E$), increasing in depth - in fact below the zone of reduced resistance ($z > X_r$), $p_u = 9S_u$ (see paragraph 3.3.2.1). As a result, we conclude that a law with the initial stiffness increasing in depth would be required in our model; in alternative, we simply consider the average value of $k_s \times D$ in the API distribution, 64 MPa.

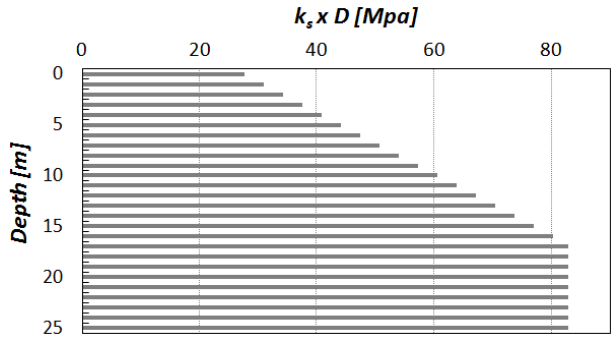

Figure 6.9: slender pile, case SC1 - profile in depth of the first slope of API *p-y curves*, identified as the coefficient of subgrade reaction.

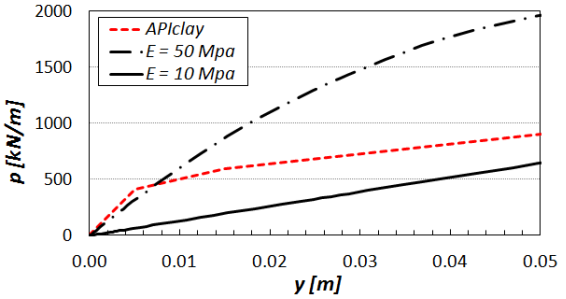

Figure 6.10: slender pile, case SC1 - *p-y curves* at 18.5 m depth, after API (ε_{50}=1%) and 3DFEA under pile rigid displacement with a large-strain and a small-strain Young's modulus.

The corresponding value of the small-strain Young's modulus to include in our model - constant all along the pile - is then estimated by means of a proportion between 64 MPa and the value in Table 6.4, net of the large-strain modulus (10 MPa), obtaining E_0 =50 Mpa. By applying the same procedure for case SC2 leads us to consider E_0 =25 Mpa. Note that in the two cases the ratio between the moduli is the same (5); however this might not be the case for other soil parameters, as the distribution of the API ultimate resistance - therefore of $k_s \times D$ - may have a different shape, presenting a larger or smaller zone of reduced resistance.

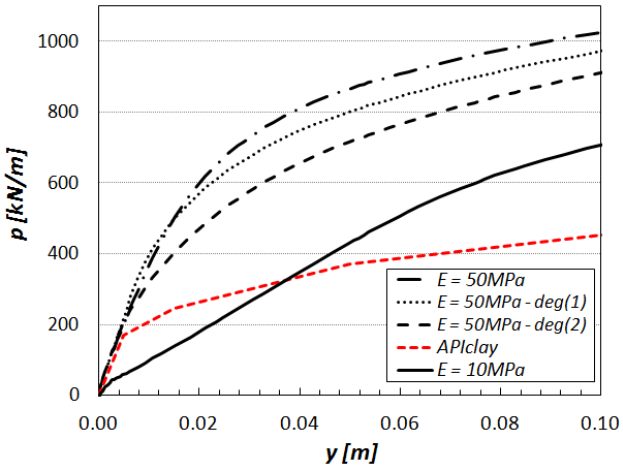

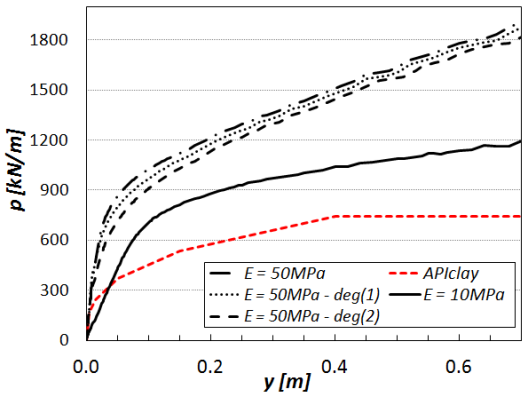

Figure 6.11: slender pile, case SC1 - *p-y curves* at 0.5 m depth, after API (ε_{50}=1%) and 3DFEA under pile rigid displacement with a large-strain and a small-strain Young's modulus combined with two different degradation laws.

In Figures 6.10 and 6.11 we show the *p-y curves* for rigid displacements compared to API ones for case SC1: as expected, the use of E_0 results in a slight overestimation (underestimation) of the small-strain stiffness response at shallow (large) depths[3].

[3]This analysis has been conducted by means of simulations under rigid displacement as they are more time-saving; nonetheless similar results would have been obtained for deflection at mud line.

The stiffness degradation is then simulated by imposing a modified hardening law: several solutions have been tested, acting on the coefficient B_c and the initial cohesion. In Figure 6.11 we propose two degradation curves, both with B_c=0.007 and $S_{u,I}$ respectively of 50 kPa (*deg1*) and 25 kPa (*deg2*). This last is considered the best, as provides a neat deviation from the not degraded curve at small deformations (y=0.01 m, ε=0.2%), tending towards the curve with large-strain modulus. Nonetheless at large displacements - larger than 0.1 m - it probably overestimates the stiffness and the ultimate resistance.
For case SC1, the *p-y curves* for deflections at mud line are reported in Figure 6.12, where the large-strain response previously presented is compared to the small-strain one - E_0 and *deg2*, here simply E_0: note that this second fits good with Jeanjean (2009) for small and medium displacements and the API solution clearly underestimates the mobilized resistance. However, as for the large-strain response, more reliable indications are provided by the force evolution at the mud line (Figure 6.13): the conclusions are the same, apart from that now the proposed modification of Jeanjean is the closest to our prediction.

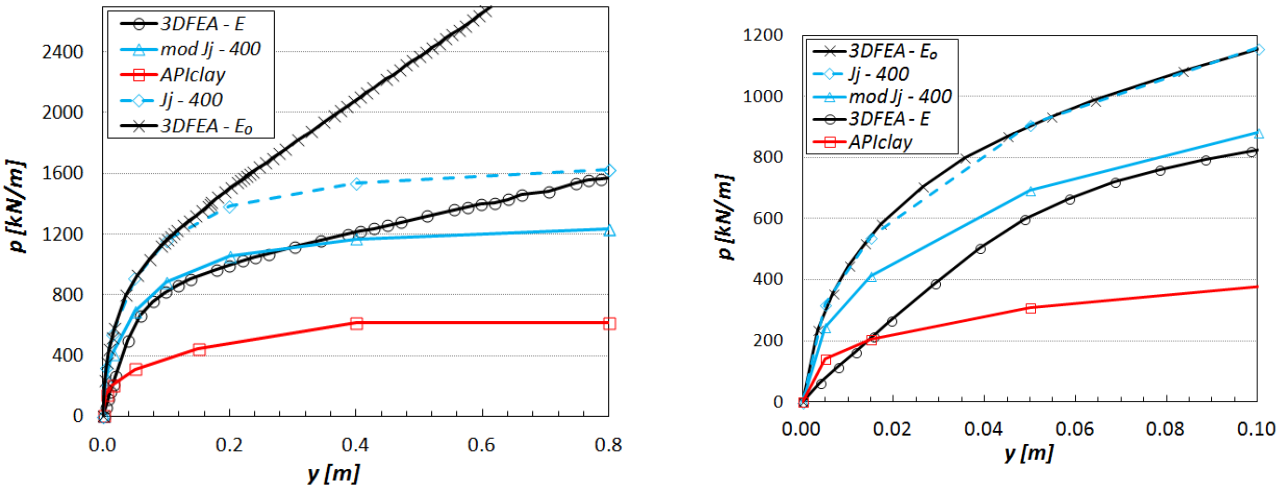

Figure 6.12: Slender pile, case SC1 - *p-y curves* at 0.25 m depth for mud line deflections, in 3DFEA - large-strain (E) and small-strain parameters (E_0 and degradation type 2) - 1D model calibrated with API/Matlock (1970), Jeanjean (2009) and proposed Jeanjean modification.

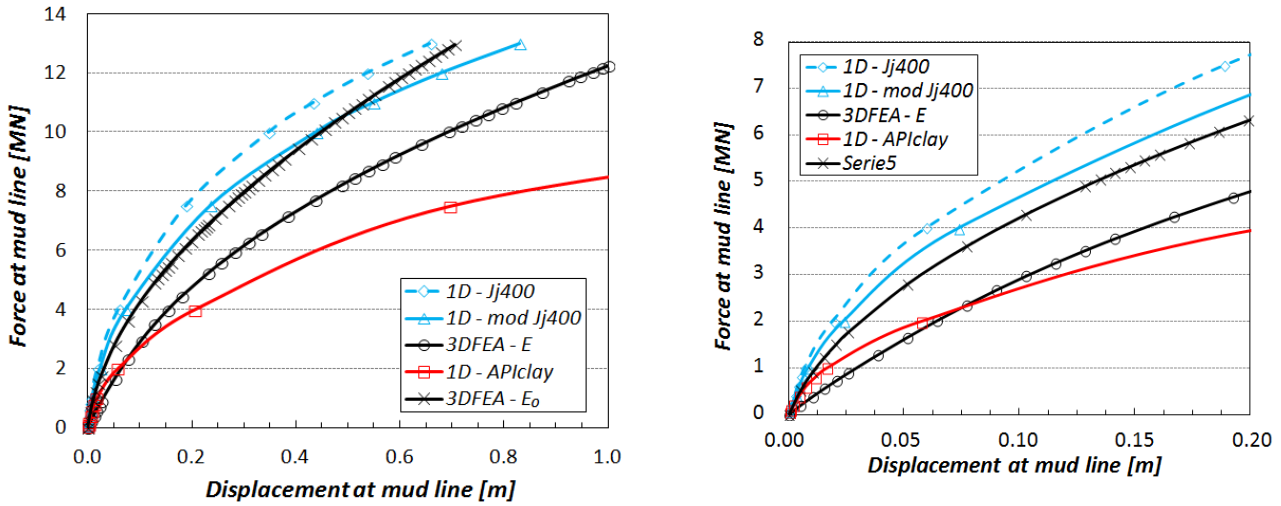

Figure 6.13: Slender pile, case SC1 - force in function of the deflection at mud line, in 3DFEA - large-strain (E) and small-strain parameters (E_0 and degradation type 2), 1D model calibrated with API/Matlock (1970), Jeanjean (2009) and proposed Jeanjean modification.

The same procedure followed for case SC2 - E=5 MPa, E_0=25 MPa combined to B_c=0.007, $S_{u,I}$=12.5 kPa and $S_{u,F}$=100 kPa - returns the results in Figure 6.14. The trend in confirmed and the modified Jeanjean fits even better with the 3D prediction.

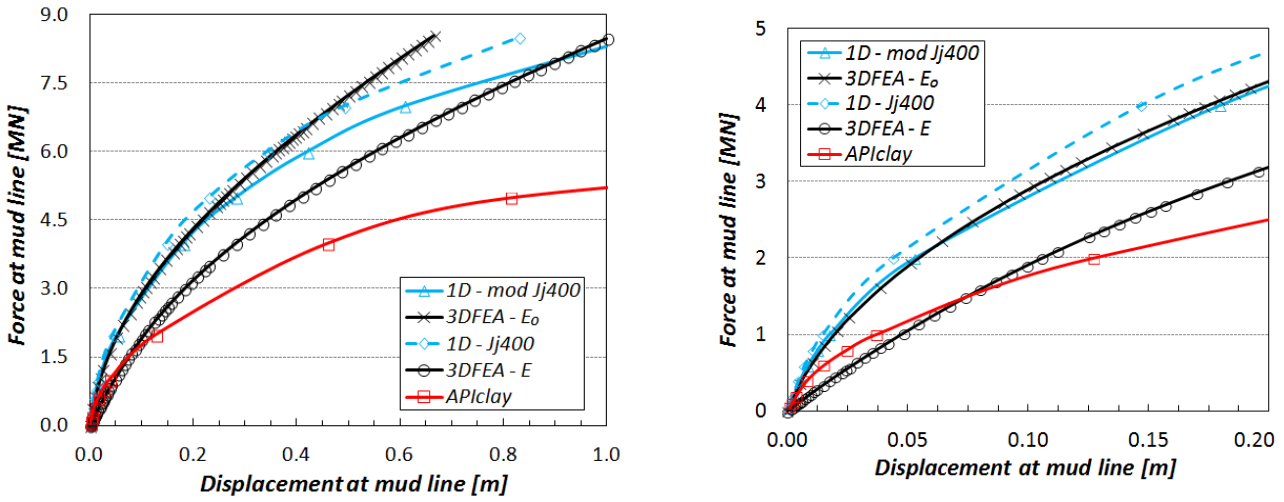

Figure 6.14: Slender pile, case SC2 - force in function of the deflection at mud line, in 3DFEA - large-strain (E) and small-strain parameters (E_0 and degradation type 2), 1D model calibrated with API/Matlock (1970), Jeanjean (2009) and proposed Jeanjean modification.

As an example, in Table 6.5 we report the predicted value of mud line deflection according to the different models for realistic values of lateral load.

case	load (MN)	APIclay	Mod Jj-400	Jeanjean-400	3DFEA-E_0
SC1	10	161	43	35	44
SC2	5	186	28	23	26

Table 6.5: predicted mud line deflection (cm) according to 3DFEA - small-strain parameters (E_0 and degradation type 2) - 1D model calibrated with API/Matlock (1970), Jeanjean (2009) and proposed Jeanjean modification; slender pile, case SC1 and SC2 for typical lateral force.

6.3.3 Discussion

While we remark that in order for the 3D model to provide a solid improvement of the *p-y curves* a more accurate definition of the constitutive law would be required - increasing stiffness in depth, small-strain modulus and degradation - still the presented analysis leads to interesting conclusions. At first, the API/Matlock (1970) formulation is such that both the ultimate resistance of the soil and its stiffness response, either at small and large strains, are underestimated. Secondly, the Jeanjean (2009) formulation, especially in its modification, produces a better prediction, in particular if we consider the proposed stiffness degradation law as the most representative. In the end, we believe this is the case: in fact, with a solicitation as in Figure 6.1 (right), for medium-to-large mud line deflections - e.g. for 9 MN of lateral load - the overall response along the pile is mainly governed by the small-strain response.

In addition, note that, in the presented comparisons, no terms of base resistance have been included in the calibrated 1D model. In fact, some simulations have proved that the implemented law for the base resistance (paragraph 4.2.2.2) does not provide important changes in the results; this is justified by the small pile (tip) section, which is though not to play a big role in the overall resistance. This, along with the good fit found with the Jeanjean formulation, allows us to conclude that for slender piles the simple 1D model with sole lateral springs is still valid, on condition of a consistent choice and improvement of the *p-y curves*.

6.4 Large Pile

The same procedure applied at the slender pile case is now presented for a tubular large pile (caisson), whose parameters are reported in Table 6.6. We consider case SC1 previously investigated, maintaining the parameters of Table 6.1, 6.2 - only the small-strain Young's modulus E_0 will need to be modified.

$L \times D$ (m×m)	t (cm)	E (GPa)	ν (-)	ϕ_{intf} (^{o})	κ_P (Pa)
24×8	8	20	0.3	20	10^9

Table 6.6: large pile parameters - from left to right: lenght, diameter, wall thickness, Poisson's ratio, Young's modulus, interface friction angle and penalization factor.

We make use of the two 3D models presented for this geometry in chapter 5 (paragraph 5.4): with the mesh of Figure 5.36 - no soil inside the caisson and at base - we apply a rigid displacement, allowing to evaluate the ultimate resistance and the large-strain coefficient of subgrade reaction; in the mesh of Figure 5.42 - inner and base soil - we impose a mud line deflection (Figure 6.15). As for the analysis of paragraph 5.4, in order to limit the convergence issues in LAGAMINE, we choose a concrete Young's modulus; however the results proposed are still consistent.

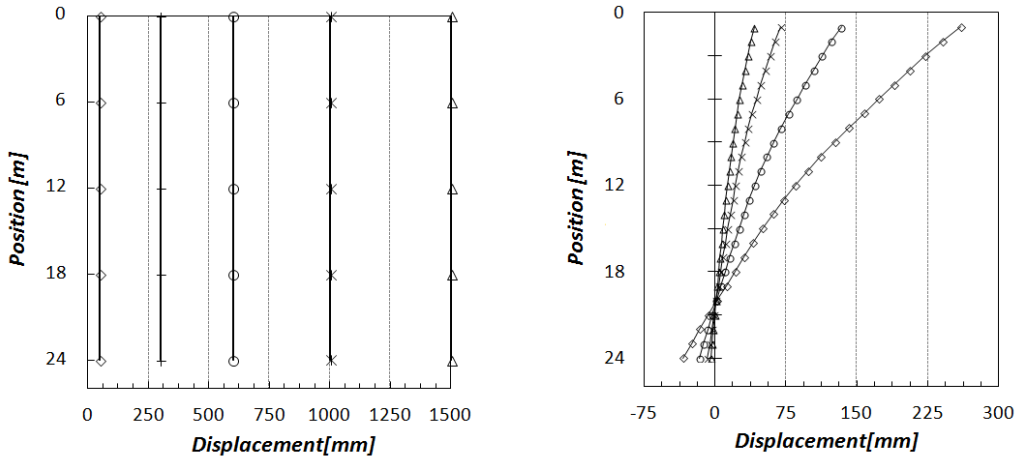

Figure 6.15: large pile - phases of pile rigid displacement, with no inner and base soil (left); deflection at mud line, with base and inner soil (right).

In the analysis of ultimate resistance and stiffness response we follow the same steps just detailed for the slender pile; therefore the main focus is on the differences between the two piles, giving for granted some of the observation previously done.

6.4.1 Ultimate resistance

The *p-y curves* under rigid displacement for case SC1 are showed in Figure 6.16. At shallow depths the simulation presents some issues after 1.1 m of displacement, while for displacements larger than 1.5 m it fails; as a results, while for the slender pile the targeted point of ultimate conditions is $20 \times y_c$, in this case, being y_c=0.2 m, we cannot apply the same criterion. Nonetheless, by extracting the distribution at 1.5 m, the trend is similar to the one in Figure 6.3 - API underestimates at any depth, discrete fit with modified Jeanjean.

However we remark again that the ultimate resistance requires further investigations, as in all our models - slender and large pile - no clear plateau has been detected and the curves have showed a dependence on elastic parameters. More informations might be gathered by targeting relevant locations all around the pile and tracing the stress path in the deviatoric plane.

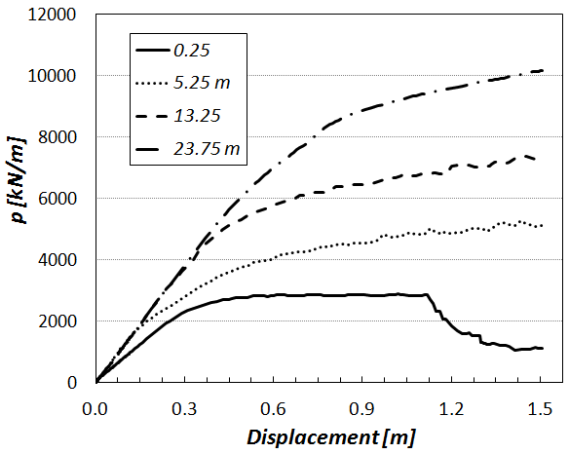

Figure 6.16: large pile, case SC1 - *p-y curves* for different pile rigid displacement.

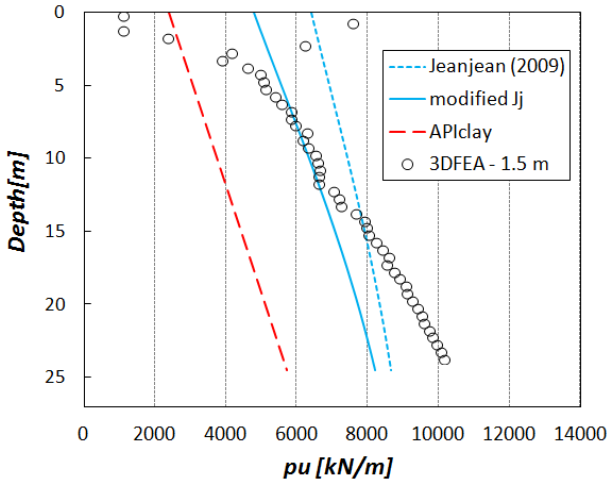

Figure 6.17: large pile, case SC1 - depth profile of ultimate soil resistance after API/Matlock (1970), Jeanjean (2009) and proposed modification; 3DFEA pressure profile for a 1.5 m rigid displacement.

6.4.2 Stiffness response

6.4.2.1 Small-strain behaviour

As previously reported in the discussion on the slender pile, we believe that the proposed degradation law (*deg2*) coupled with a small-strain Young's modulus E_0 is the most representative solution; therefore we limit to show procedure and results only for this case.

Starting from the curves of Figure 6.16, the coefficient of subgrade reaction ($\times D$) is estimated at 12.7 MPa. This is consistent with the analytical predictions of Table 6.4[4] and there is no clear evidence of diameter influence - 3D results for the two geometries are very close. We believe this is due to the fact that no soil is included at the base and eventual effects related to the larger lateral surface - such as additional mobilization of friction - are limited by the type of solicitation - the rigid displacement mobilizes only the friction component in plane *x-y*.
The in-depth distribution of the coefficient of subgrade reaction ($\times D$) according to API - the initial slope of the discretized formula - is presented for the large pile in Figure 6.18. With respect to Figure 6.9, the zone of reduced resistance is more extended; therefore the average value is lower (48 MPa).

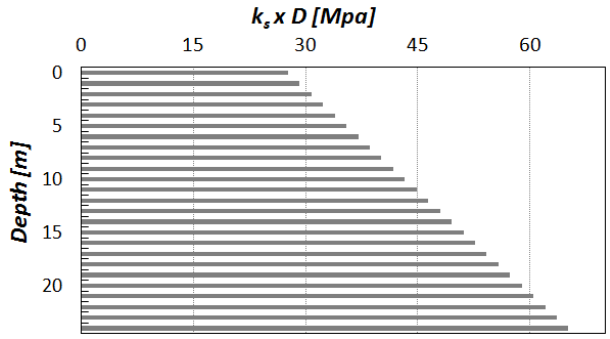

Figure 6.18: large pile, case SC1 - profile in depth of the first slope of API *p-y curves*, identified as the coefficient of subgrade reaction.

The value of the small-strain Young's modulus may then be inferred starting from $k_s \times D$, by a proportion between the API average value and the estimated value of 12.7 MPa, net of the large-strain modulus (10 MPa); we obtain E_0=38 MPa. Nonetheless this method assumes that the targeted slope of the *p-y curves* is comparable in the two models - rigid displacement and mud line deflection. While

[4]Values of Table 6.4 are normalized with respect to the diameter, therefore the analytical solutions are the same for slender and large pile case.

this hypothesis is pertinent for the slender pile, this is not the case for the large pile: in fact, it has been established that at shallow depths and around the pile tip, the *deflected* curves are stiffer than the *rigid* curves - the mentioned limitations of the *rigid* model (limited friction, no soil at base) are enhanced by the larger base section and lateral surface.
For this reason, in the 3D model we consider E_0=35 MPa, in substitution to the value present in Table 6.2 (case SC1). However, this confirms the requirement of an advanced constitutive law including a well defined small-strain modulus.

The *p-y curves* for the large pile and case SC1 with stiffness degradation type 2 (E_0=35 MPa, B_c=0.007, $S_{u,I}$=25 kPa and $S_{u,F}$=100 kPa) are showed in Figure 6.19. Note the important mud line effect (stiffer curve) and the well shaped curves around the pile tip. As expected and similarly to the slender pile case, it has been established that they provide an overestimation (underestimation) of the stiffness response at shallow (medium) depths with respect to the APIclay formula: this is logic as in our model the small-strain Young's modulus is constant in depth, rather than increasing.

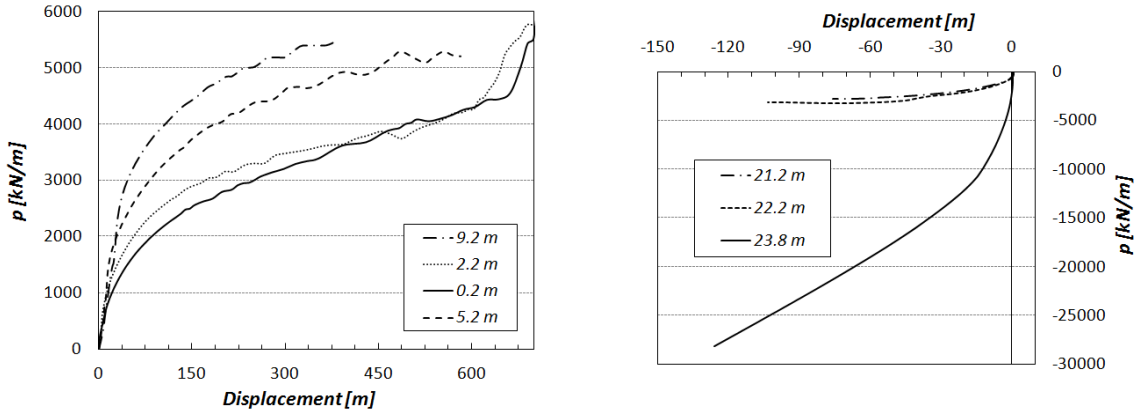

Figure 6.19: large pile, case SC1 with small-strain parameters (E_0 and degradation type 2) - *p-y curves* for different mud line deflections at different locations.

The comparison at the mud line with the API and Jeanjean formulas, this last in the form of the proposed discetization for G_{max}/S_u=400, for its modification and for (discretized) G_{max}/S_u=550, is provided in Figure 6.20. For small-to-medium deflections - below 0.2 m, corresponding to ε=ε_{50}=0.1 % - the 3D curve fit well with Jeanjean550, while towards larger deflections it tends to Jeanjean400.

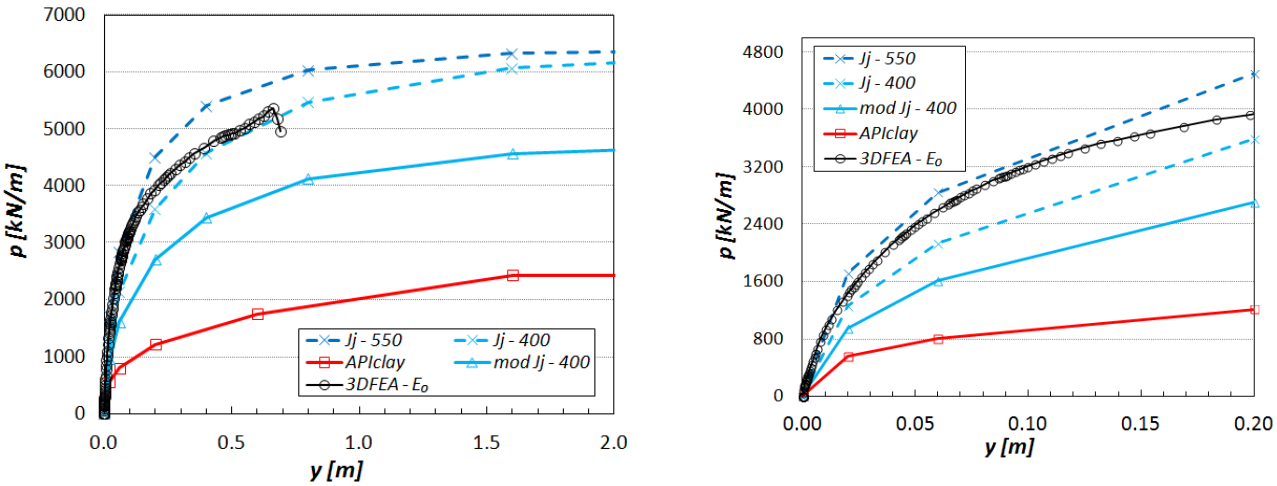

Figure 6.20: large pile, case SC1 - *p-y curves* at 0.2 m depth for mud line deflections, in 3DFEA - small-strain parameters (E_0 and degradation type 2) - 1D model calibrated with API/Matlock (1970), Jeanjean (2009) with G_{max}/S_u=400 and proposed modification, Jeanjean (2009) with G_{max}/S_u=550.

Finally, the evolution of the lateral force is showed in Figure 6.21. The prediction by Jeanjean550 fit very well with the 3D results for all the considered value of lateral load, while the APIclay clearly underestimates the stiffness response - the implemented base resistance in the 1D model provides a limited increase of resistance, not required for Jeanjean550 and not sufficient to improve enough the APIclay prediction.

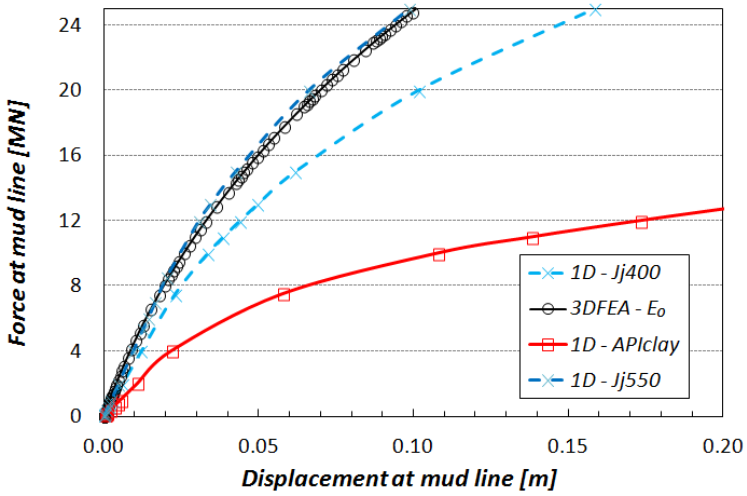

Figure 6.21: large pile, case SC1 - force in function of the deflection at mud line, in 3DFEA - small-strain parameters (E_0 and degradation type 2) - 1D model calibrated with API/Matlock (1970), Jeanjean (2009) with G_{max}/S_u=400 and proposed modification, Jeanjean (2009) with G_{max}/S_u=550.

deflection	load (MN)	APIclay	Jeanjean-400	Jeanjean-550	3DFEA-E_0
head	20	71	10	6.7	6.1
tip	20	47	5	2	0.1

Table 6.7: predicted pile head and tip deflection (cm) according to 3DFEA - small-strain parameters (E_0 and degradation type 2) - 1D model calibrated with API/Matlock (1970), Jeanjean (2009) and proposed Jeanjean modification; slender pile, case SC1 and SC2 for typical lateral force.

A comparison of the predicted pile head and tip displacements for a realistic load of 20 MN is presented in Table 6.7. The only unexpected result is the large difference in the tip deflection between Jenajean550 and the 3D results. We then extract the corresponding profile of Figure 6.22 for a better comprehension - it is discussed in the next paragraph.

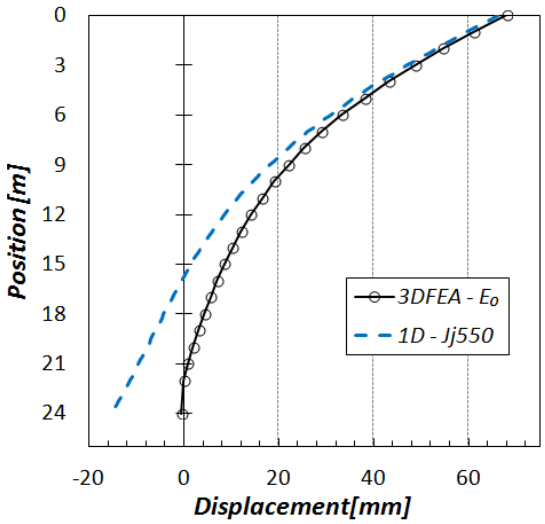

Figure 6.22: large pile, case SC1 with small-strain parameters (E_0 and degradation type 2) - deformed pile for a lateral mud line load of 20 MN, in 3DFEA and Jenajean (2009) with G_{max}/S_u=550.

6.4.3 Discussion

Considering the results obtained in terms of *p-y curves* and force variation, comparing with the numerical results, the APIclay formula provides an evident underestimation of the stiffness response for small, medium and large deflections; in addition, while for the slender pile the best fit was given by Jeanjean400 - especially in the proposed modification - for the large pile Jeanjean550 formula produce a very good prediction.
On the other hand, the direct comparison of the deformed pile suggests that Jeanjean550 overestimates the *toe-kick*, which is almost null in our simulation.

As a result, we conclude that, although the system response at shallow depths can be predicted with a certain accuracy even by applying the 1D standard model, if a full characterization of the overall behaviour is the main goal, rotational springs and base resistance must be implemented along with lateral springs.

Chapter 7

Conclusions

7.1 General

An accurate revision of monopiles foundations for offshore wind turbines has been realised, with a special focus on the soil-structure response under monotonic lateral loads. In particular, we have highlighted the importance of a correct evaluation of the stiffness reaction: the main goal has been the assessment and improvement of the *p-y curves* method.
The main results consists in: (1) a working 1D finite element code able to reproduce the existing design methods, accounting for additional effects related to geometry and mechanical properties; (2) 3D finite element models providing an accurate analysis of the *p-y curves*, highlighting all the physical phenomena in relation to different type of soil, solicitation and geometry; (3) for soft clay and both slender and large pile, an overall evaluation of the existing design methods by comparison between 3D numerical results and predictions of the calibrated 1D code.

7.2 1D finite element code

The 1D code in PYTHON has successfully been validated with the finite difference program OPILE, identifying a post-processing issue in this last. It has been showed that in some cases the standard method based on Euler-Bernoulli (EB) beam and lateral springs requires some improvements: at first, the Timoshenko beam provides a better prediction of pile deflection and internal forces for short piles presenting enough bending, therefore in very stiff and hard soil. In presence of a rigid behaviour and for slender piles, the EB formulation is still valid.
Moreover, additional moment and shear base resistance terms have been implemented, representing a rotational and lateral spring at the pile tip: while the first one has not been validated - still, we believe that the formulation can be taken as a reference - the presence of base shear can limit the pile deflection, either at the base and at the mud line.

7.3 3D finite element analysis

For both slender and large pile, the 3D finite elements analysis has highlighted the main phenomena contributing to the soil response and, therefore, to the *p-y curves*: effects of the initial stress state, detachment and gap propagation, bump, initial slope, base resistance. The shape of the curves is particularly affected by the type of solicitation applied.
The two piles present different behaviours when deflected at the mud line, due to the different flexural rigidity. In presence of bending (slender pile), the mobilized resistance at the base is limited and the overall response depends mainly on the lateral soil reaction; when the rigid rotation prevails (large pile), the soil at the base - which is typically larger - plays a bigger role and the lateral resistance consists in both horizontal and vertical components, especially with a larger surface of contact.

7.4 Monopiles in soft clay

The comparisons between the 3D simulations and the predictions provided by the existing design methods have remarked the requirement of an advanced soil constitutive law and a specific analysis of the ultimate resistance, in order to improve the reliability of the models.
Still, from the results we can draw important conclusions. At first, for both piles, the API/Matlock (1970) formulation for cohesionless materials strongly underestimates the stiffness response at small, medium and large head deflections. Secondly, for the slender pile, Jeanjean400 formulation produces good predictions, especially in the proposed modification, and the simple 1D model with sole lateral springs is still valid.
Lastly, for the large pile, Jeanjean550 formulation produces a very good prediction at shallow depths; nonetheless, a correct characterization at large depths and at the base requires the implementation in the 1D model of rotational springs and base resistance terms.

7.5 Limitations of the method and proposals

With a focus on the 3D finite element analysis, the proposed work relies on specific hypothesis and simplifications: the following list aims to propose a more accurate and realistic model, on which future works may be dedicated, while highlighting the limitations of the presented results. In addition, we report specific subjects that may be tackled.

- Revision of the pile geometry, with steel material, hollow section and soil plug for slender and large piles.
- Advanced soil constitutive law, including small-strain Young's modulus, stiffness degradation and stiffness response increasing in depth.
- With clay, undrained conditions, accounting for pore water pressures - in addition to undrained soil parameters.
- Influence of the water column above the mud line on initial stress state and pressure distribution.
- Investigation of the ultimate conditions, by tracing the stress state evolution at relevant locations.
- Comparisons based on both force in function of the lateral displacement and moment in function of the rotation.
- Calibration of the base resistance starting from the *p-y curve* at the last element.
- Implementation of rotational springs in the 1D model; the starting point for the calibration may be the investigation of the coupling between friction and soil stiffness for large piles.

Appendices

Appendix A

1D Finite Element Formulation

A.1 Weak form and beam stiffness matrix

A.1.1 Euler-Bernoulli beam

Recalling the hypothesis of paragraph 4.2.1.1 for the Euler-Bernoulli beam, we introduce the Hooke's Law in the axial component ($\sigma_{11} = E\epsilon_{11} = E\kappa x_3$) and the second moment of area I. The internal virtual work (IVW) expression of two-dimensional elasticity is then:

$$\begin{aligned} IVW = \int_0^L \int_{-t/2}^{t/2} \sigma_{ij}\epsilon_{ij} dx_3 dx_1 &= \int_0^L \int_{-t/2}^{t/2} \sigma_{11}\epsilon_{11}(v) dx_3 dx_1 \\ &= \int_0^L \int_{-t/2}^{t/2} (E\kappa x_3 \cdot x_3\kappa(v)) dx_3 dx_1 = EI \int_0^L \kappa(u_3)\kappa(v) dx_1 \end{aligned} \tag{A.1}$$

where L and t are length and thickness of the beam, E the Young's modulus, EI the flexural rigidity assumed constant and v is the virtual normal displacement along x_3. The weak form to be used in the FE discretization is obtained by equating the IVW to the external virtual work (EVW) resulting from a charge q distributed along the beam length, including eventual boundary terms (BT). In particular:

$$EVW = \int_0^L qv dx_1 = EI \int_0^L \kappa(u_3)\kappa(v) dx_1 + BT \tag{A.2}$$

The beam potential energy U (kJ) is assumed equal to the energy only due to bending strains:

$$\begin{aligned} U = U_{bend.str} + U_{shear.str} &= \frac{1}{2}\int_0^l \sigma_x \varepsilon_x dx + \frac{1}{2}\int_0^l \tau_{xy}\gamma_x dx \\ &= \frac{1}{2}\int_0^l \frac{M^2}{EI} dx + \frac{1}{2}\int_0^l \frac{V^2}{GA_s} dx \approx \frac{1}{2}\int_0^l \frac{M^2}{EI} dx \end{aligned} \tag{A.3}$$

The problem can now be reduced to a mono-dimensional one in x_1 (here simply x), as the beam can be represented as a disjoint collection of linear finite elements. For each element, two nodal values are given for each variables, in our case the normal displacement and the rotation - two degree of freedom (dof=$n/2$). The variables, and the corresponding test functions (virtual variables), can be interpolated using shape functions (N_i, for $i = 1, ...n$), hence expressed as linear combinations of nodal values and shape functions. In equation A.2 the integral depends on second order derivatives, hence N_i must be at least C^1-continuous. However, a better representation of the variability is assured by cubic functions (C^2), commonly used in these cases: four functions, corresponding to unitary rotation/displacement at one node, are presented in Figure A.1 and equation A.4.

$$
\begin{aligned}
N_1 &= \frac{1}{l^3}(2x^3 - 3x^2 l + l_e^3) \\
N_2 &= \frac{1}{l^3}(x^3 l - 2x^2 l^2 + x l^3) \\
N_3 &= \frac{1}{l^3}(-2x^3 + 3x^2 l) \\
N_4 &= \frac{1}{l^3}(x^3 l - x^2 l^2)
\end{aligned}
\qquad \text{(A.4)}
$$

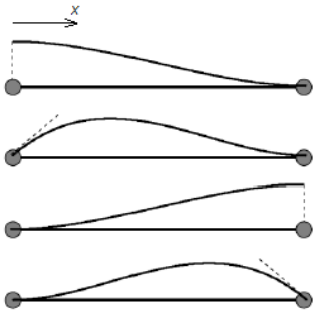

Figure A.1: Cubic shape functions for finite element long l, for Euler-Bernoulli beam

The interpolation equations are then introduced into the weak form, obtaining the FE equation for an Euler-Bernoulli beam. This last provides, for each element, the relationship between the nodal values of the variables and the corresponding loads by means of the symmetric, (n×n) elementary stiffness matrix K_{el} as follows:

$$
K_{el} \cdot w_{el} = F_{el} \;\; ; \;\; \frac{EI}{l^3}\begin{bmatrix} 12 & 6l & -12 & 6l \\ & 4l^2 & -6l & 2l^2 \\ & & 12 & -6l \\ & sym & & 4l^2 \end{bmatrix} \begin{bmatrix} u_3^{(1)} \\ \beta^{(1)} \\ u_3^{(2)} \\ \beta^{(2)} \end{bmatrix} = \begin{bmatrix} v^{(1)} \\ m^{(1)} \\ v^{(2)} \\ m^{(2)} \end{bmatrix} \quad \xrightarrow{assembling} \quad K \cdot w = F \qquad \text{(A.5)}
$$

where the (n×1) vector w_{el} and the (n×1) vector F_{el} represent elementary nodal displacements/ rotations and elementary shear forces/moments at node 1 and 2.
The global system (end of equation A.5), whose shape depends on the discretization (L/l), is obtained by assembling elementary vectors and stiffness matrices, accounting for the contributions at each node.

A.1.2 Timoshenko beam

Recalling the hypothesis of paragraph 4.2.1.2, the Hooke's law is introduced for two contributions ($\sigma_{11} = E\epsilon_{11}$ and $\sigma_{13} = GE\gamma$), therefore the resultant weak form is:

$$
\begin{aligned}
EVW + BT = \int_0^L qv dx_1 + BT = IVW &= \int_0^L \int_{-t/2}^{t/2} [\sigma_{11}\epsilon_{11}(v) + 2\sigma_{13}\gamma(v)] dx_3 dx_1 \\
&= EI \int_0^L \beta_{,1}\phi_{,1} dx_1 + GAk \int_0^L (u_{3,1} - \beta)(v_{,1} - \phi) dx_1
\end{aligned}
\qquad \text{(A.6)}
$$

where v and ϕ are the virtual normal displacement and the virtual rotation, G the shear modulus, A the beam section area and k the shear correction factor - 5/6 for rectangular sections, 9/10 for circulars. Note that two main contributions appear, accounting respectively for the bending and the shear response.
The beam potential energy U (kJ) is now calculated according to equation A.7, where both bending and shear contribution are to be included.

$$
\begin{aligned}
U = U_{bend.str} + U_{shear.str} &= \frac{1}{2}\int_0^l \sigma_x \varepsilon_x dx + \frac{1}{2}\int_0^l \tau_{xy}\gamma_x dx \\
&= \frac{1}{2}\int_0^l \frac{M^2}{EI} dx + \frac{1}{2}\int_0^l \frac{V^2}{GA_s} dx \approx \frac{1}{2}\int_0^l \frac{M^2}{EI} dx
\end{aligned}
\qquad \text{(A.7)}
$$

The following cubic shape functions can then be used [15]:

$$N_1 = \frac{1}{1+\Phi}\left[1 - 3\left(\frac{x}{l}\right)^2 + 2\left(\frac{x}{l}\right)^3 + \left(1 - \frac{x}{l}\right)\Phi\right]$$
$$N_2 = \frac{l}{1+\Phi}\left[\frac{x}{l} - 2\left(\frac{x}{l}\right)^2 + \left(\frac{x}{l}\right)^3 + \frac{1}{2}\left(\frac{x}{l} - \left(\frac{x}{l}\right)^2\right)\Phi\right]$$
$$N_3 = \frac{1}{1+\Phi}\left[3\left(\frac{x}{l}\right)^2 - 2\left(\frac{x}{l}\right)^3 + \frac{x}{l}\Phi\right]$$
$$N_4 = \frac{l}{1+\Phi}\left[-\left(\frac{x}{l}\right)^2 + \left(\frac{x}{l}\right)^3 - \frac{1}{2}\left(\frac{x}{l} - \left(\frac{x}{l}\right)^2\right)\Phi\right] \tag{A.8}$$

where the term $\Phi = \dfrac{12EI}{kAGl^2}$ gives the relative importance of the shear deformations to the bending deformations. Note that if neglecting shear deformations (Φ=0), it correspond to functions A.4. As a result, we obtain the elementary stiffness matrix of equation A.9, which corresponds to the matrix in equation A.5 for Φ=0.

$$K_{el} = \frac{EI}{l^3(1+\Phi)}\begin{bmatrix} 12 & 6l & -12 & 6l \\ & (4+\Phi)l^2 & -6l & (2-\Phi)l^2 \\ & & 12 & -6l \\ & sym & & (4+\Phi)l^2 \end{bmatrix} \tag{A.9}$$

We remark that the weak form of equation A.6 contains at most C^0 functions, hence a linear interpolation for the Timoshenko problem could be sufficient: it would provide a more time-saver method for the system resolution while lowering the quality of the approximated solution. In particular, the resulting (elementary) stiffness matrix accounts for the two contributions separately - shear ($K_{el,s}$) and bending ($K_{el,b}$), equation. The numerical integration is carried out by Gaussian quadrature, on one and two points respectively for $K^{[1]}_{el,b}$ and $K^{[2]}_{el,s}$.

$$K_{el} = K^{[1]}_{el,b} + K^{[2]}_{el,s} = \frac{EI}{l}\begin{bmatrix} 0 & 0 & 0 & 0 \\ & 1 & -6l & 1 \\ & & 0 & 0 \\ & sym & & 1 \end{bmatrix} + \frac{GAk}{l}\begin{bmatrix} 1 & \frac{l}{2} & -1 & \frac{l}{2} \\ & \frac{l^2}{3} & -\frac{l}{2} & \frac{l^2}{6} \\ & & 1 & -\frac{l}{2} \\ & sym & & \frac{l^2}{3} \end{bmatrix} \tag{A.10}$$

Nonetheless, since displacements and rotations are interpolated with the same shape functions, a too stiff numerical behaviour is detected, especially in thin beams for which it is impossible to reproduce null shear rotations - $\gamma \neq 0$ for thickness $t \to 0$. This tendency to lock (locking) drives to computed FE displacements much smaller than the exact solution and can be avoided by applying a one point integration also for the shear stiffness matrix ($K^{[2]}_{el,s}$). In particular:

$$K^{[1]}_{el,s} = \frac{GAk}{l}\begin{bmatrix} 1 & \frac{l}{2} & -1 & \frac{l}{2} \\ & \frac{l^2}{4} & -\frac{l}{2} & \frac{l^2}{4} \\ & & 1 & -\frac{l}{2} \\ & sym & & \frac{l^2}{4} \end{bmatrix} \tag{A.11}$$

A.2 Soil stiffness matrix and solicitation vector

For the cubic shape functions proposed in the Euler-Bernoulli beam theory (equation A.4), the resulting soil stiffness matrix and solicitation vector are listed below - here $k_i^s = k_i$.

$$K_{el}^s = \begin{bmatrix} \frac{l}{35}(10k_1+3k_2) & \frac{l^2}{420}(15k_1+7k_2) & \frac{9l}{140}(k_1+k_2) & \frac{-l^2}{420}(7k_1+6k_2) \\ & \frac{l^3}{840}(5k_1+3k_2) & \frac{l^2}{420}(6k_1+7k_2) & \frac{-l^3}{280}(k_1+k_2) \\ & & \frac{9l}{140}(k_1+k_2) & \frac{-l^2}{420}(7k_1+6k_2) \\ & sym & & \frac{l^3}{840}(3k_1+5k_2) \end{bmatrix} \tag{A.12}$$

$$g_{el} = \begin{bmatrix} \frac{l}{20}(7\sigma_1+3\sigma_1) \\ \frac{l^2}{60}(3\sigma_1+2\sigma_1) \\ \frac{l}{20}(3\sigma_1+7\sigma_1) \\ \frac{-l^2}{60}(2\sigma_1+3\sigma_1) \end{bmatrix} \tag{A.13}$$

For the cubic shape functions proposed in the Timoshenko beam theory (equation A.8):

$$K_{el}^s = \begin{bmatrix} K_{1,1} & K_{1,2} & K_{1,3} & K_{1,4} \\ & K_{2,2} & K_{2,3} & K_{2,4} \\ & & K_{3,3} & K_{3,4} \\ & sym & & K_{4,4} \end{bmatrix} \tag{A.14}$$

$$g_{el} = \begin{bmatrix} \frac{l}{60(\Phi+1)}[30\sigma_1(1+\Phi)+l\delta_\sigma(10\Phi+9)] \\ \frac{l^2}{120(\Phi+1)}[10\sigma_1(1+\Phi)+l\delta_\sigma(5\Phi+4)] \\ \frac{l}{60(\Phi+1)}[30\sigma_1(1+\Phi)+l\delta_\sigma(20\Phi+21)] \\ -\frac{l^2}{120(\Phi+1)}[10\sigma_1(1+\Phi)+l\delta_\sigma(5\Phi+6)] \end{bmatrix} \tag{A.15}$$

where $\delta_\sigma = \dfrac{\sigma_2-\sigma_1}{l}$ and

$$K_{1,1} = \frac{l}{420(\Phi+1)^2}[(105k_1+35k_2)\Phi^2+(224k_1+70k_2)\Phi+120k_1+36k_2]$$

$$K_{1,2} = \frac{l^2}{840(\Phi+1)^2}[(21k_1+14k_2)\Phi^2+(50k_1+27k_2)\Phi+30k_1+14k_2]$$

$$K_{1,3} = \frac{l}{420(\Phi+1)^2}(k_1+k_2)(35\Phi^2+63\Phi+27)$$

$$K_{1,4} = -\frac{l^2}{840(\Phi+1)^2}[(21k_1+14k_2)\Phi^2+(36k_1+27k_2)\Phi+14k_1+12k_2]$$

$$K_{2,2} = \frac{l^3}{1680(\Phi+1)^2}[7(k_1+k_2)\Phi^2+(16k_1+12k_2)\Phi+10k_1+6k_2]$$

$$K_{2,3} = \frac{l^2}{840(\Phi+1)^2}[(14k_1+21k_2)\Phi^2+(27k_1+36k_2)\Phi+12k_1+14k_2]$$

$$K_{2,4} = -\frac{l^3}{1680(\Phi+1)^2}(k_1+k_2)(7\Phi^2+14\Phi+6)$$

$$K_{3,3} = \frac{l}{420(\Phi+1)^2}[(35k_1+105k_2)\Phi^2+(70k_1+224k_2)\Phi+36k_1+120k_2]$$

$$K_{3,4} = -\frac{l^2}{840(\Phi+1)^2}[(14k_1+21k_2)\Phi^2+(27k_1+50k_2)\Phi+14k_1+30k_2]$$

$$K_{4,4} = \frac{l^3}{1680(\Phi+1)^2}[7(k_1+k_2)\Phi^2+(16k_1+12k_2)\Phi+10k_1+6k_2]$$

Note that neglecting shear deformations (Φ=0), expressions A.14 and A.15 are equal, respectively, to A.12 and A.15.

In presence of base resistance, additional terms for shear force (g_{bs}, K_{bs}) and moment (g_{bm}, K_{bm}) are added in the last bean element as follows:

$$g_{last.el} = \begin{bmatrix} g_1 \\ g_2 \\ g_3 + g_{bs} \\ g_3 + g_{bm} \end{bmatrix} \qquad K^s_{last.el} = \begin{bmatrix} K_{1,1} & K_{1,2} & K_{1,3} & K_{1,4} \\ K_{2,1} & K_{2,2} & K_{2,3} & K_{2,4} \\ K_{3,1} & K_{3,2} & K_{3,3} + K_{bs} & K_{3,4} \\ K_{4,1} & K_{4,2} & K_{4,3} & K_{4,4} + K_{bm} \end{bmatrix}$$

A.3 Code Structure

In Figure A.2 we report the flow-sheet of the code.

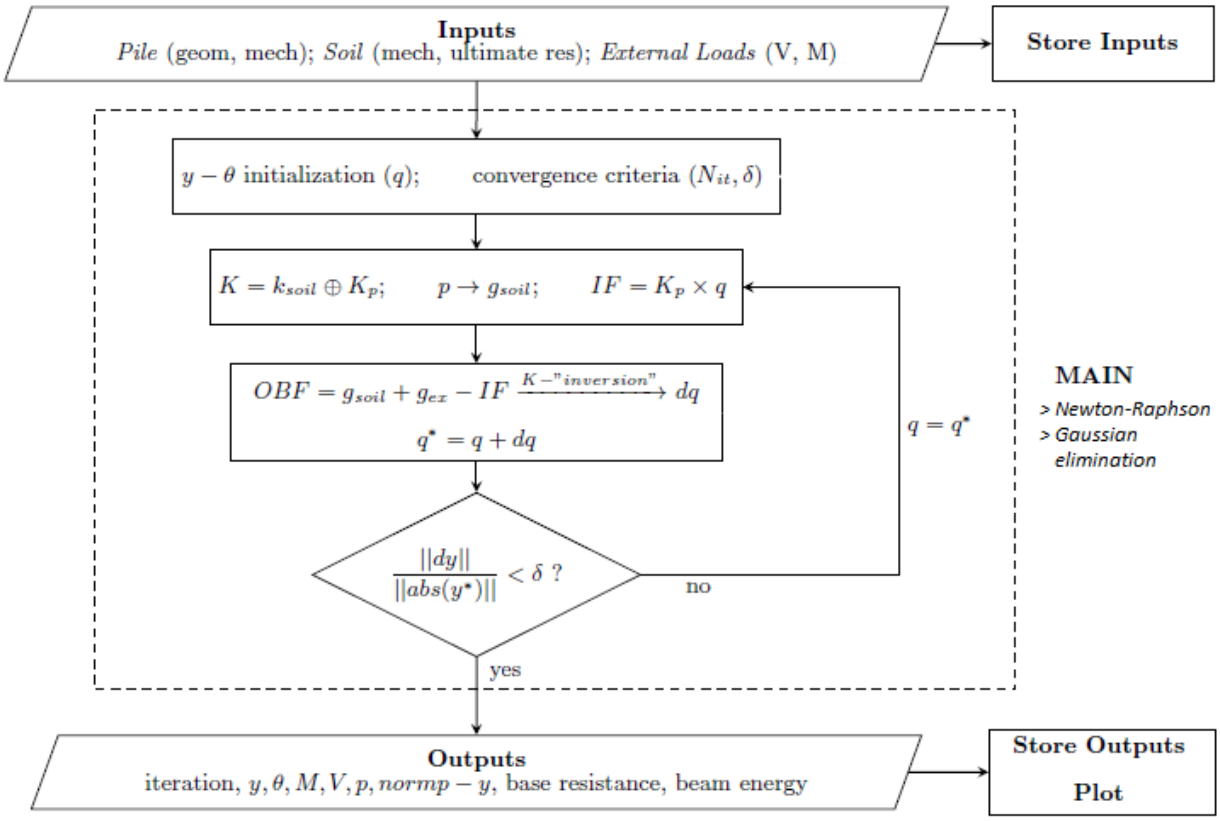

Figure A.2: Flow-sheet of the 1D finite element code.
V, M (MN, MNm) lateral force and moment applied at mud line; q vector of y, θ (m, rad), lateral displacement and rotation; N_{it} number of iteration, δ targeted residual; K, k_{soil}, K_p (kN/m or kN) total, soil and beam stiffness matrices; p, g_{soil} (kN/m, kN) lateral pressure and equivalent nodal loads; IF, OBF, g_{ex} (kN) internal, out-of-balance and external forces.

The main phases are three:

- **Input definition**: geometry, mesh and mechanical properties of pile and soil, including *API-clay* and Jeanjean(2009) ultimate lateral resistance; applied loads. A specific function allows to export the data in *Excel* format.
- **Main loop**: the applied iterative resolution method is the Newton-Raphson, resumed in Figure A.3.

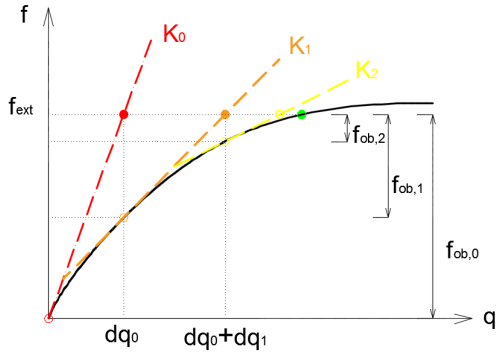

Figure A.3: Newton-Raphson resolution method. Forces f as function of the displacement q.

Starting at null displacement and null solicitation, we adjust the total stiffness matrix K_i by increasing progressively the displacement, in order to minimize the resulting out-of-balance forces $f_{ob,i}$. These lasts, defined as the difference between the external solicitation and the internal forces in beam (IF) and soil (g_{soil}), determine the displacement increment in the next iteration. The linear system is solved by means of the Gaussian elimination: in fact the matrix K_i, representing the reaction of the beam-soil system, is usually a sparse one, with an high conditioning number, therefore its inversion is not recommended. Once the solution does not evolve any more - increment of displacement negligible - the loop stops.

- Output: the resulting profiles of displacements, rotations and solicitations are returned, as well as the details of the last iteration. Specific plotting and exporting functions are implemented.

Bibliography

[1] Bakmar, C. L. (2009). Design of Offshore Wind Turbine Support Structures: Selected topics in the field of geotechnical engineering. Aalborg: Department of Civil Engineering, Aalborg University. (DCE Thesis; No. 18).

[2] Kallehave D, Byrne BW, LeBlanc Thilsted C, Mikkelsen KK. 2015. Optimization of monopiles for offshore wind turbines. *Phil. Trans. R. Soc. A* 373: 20140100. See `http://dx.doi.org/10.1098/rsta.2014.0100`.

[3] European Wind Energy Association. The European offshore wind industry - key trends and statistics 2015. February 2016.

[4] L. Zdravkovic et al. (2015). Numerical modelling of large diameter piles under lateral loading for offshore wind applications. Frontiers in Offshore Geotechnics III – Meyer (Ed.) © 2015 Taylor & Francis Group, London, ISBN: 978-1-138-02848-7

[5] B.W. Byrne et al. (2015). New design methods for large diameter piles under lateral loading for offshore wind applications. Frontiers in Offshore Geotechnics III – Meyer (Ed.) © 2015 Taylor & Francis Group, London, ISBN: 978-1-138-02848-7

[6] Cathie Associates. `http://www.cathie-associates.com/`

[7] G. Kress, 31 May 2014. Structural Analysis with FEM. Composite Materials and Adaptive Structures. ©ETH Zurich IMES-ST, March 26, 2014

[8] F. Cirak. Finite Element Formulation for Beams, Handout 2, Completed Version. University of Cambridge.

[9] Collin (2015) Conception et execution des ouvrages geotechniques, Ouvrages géotechniques – RC JPR FC 2014, ULg.

[10] Ensoft, Inc. LPILE Plus 5.0. Ensoft, Inc., 2005.

[11] American Petroleum Institute, API 2003. Recommended Practice for Planning, Designing and Constructing Fixed Offshore Platforms—Working Stress Design.

[12] Offshore Standard DNV-OS-J101. Design of Offshore Wind Turbine Structures, May 2014. Det Norske Veritas As.

[13] Offshore Standard DNV-OS-J101. Design of Offshore Wind Turbine Structures, October 2010. Det Norske Veritas As.

[14] D. Dinev, Engineering MECHANICS, Vol. 19, 2012, No. 6, p. 381–392.

[15] H.P. Gavin, Fall 2014. Structural Element Stiffness, Mass, and Damping Matrices CEE 541. Structural Dynamics, Department of Civil and Environmental Engineering, Duke University.

[16] J.N. Reddy. On locking-free shear deformable beam finite elements. Comput. Methods Appl. Mech. Engrg. 149 (1997) 113-132. Department of Mechanical Engineering, Texas A&M University, College Station, TX 77843-3123, USA.

[17] Morison, J. R., O'Brien, M. P., Johnson, J. W. and Schaaf, S. A. (1950). The Force Exerted by Surface Wave on Piles, Petroleum Transactions, American Institute of Mining Engineers 189: 149-154.

[18] Sanjeev Malhotra (2011). Selection, Design and Construction of Offshore Wind Turbine Foundations

[19] DONG Energy, also reported by Kallehave 2015 [2].

[20] M. J. Kaiser and B. F. Snyder, *Offshore Wind Energy Cost Modeling*, Green Energy and Technology, DOI: 10.1007/978-1-4471-2488-7_2, ©Springer-Verlag London 2012.

[21] Review of Options for Offshore Foundation Substructures, Prepared by the Center for Wind Energy at James Madison University, August 2012.

[22] Reese, L.C. and Van Impe, W.F.. *Single Piles and Pile Groups Under Lateral Loading*. CRC Press/Balkema, 2011. ISBN: 9780415469883, LCCN: 2010036401. `https://books.google.com/books?id=7qg0SwAACAAJ`.

[23] American Society of Civil Engineers (ASCE) (1990). Minimum design loads for for building and other structures. *ASCE standards* (formerly ANSI A58.1):7-88.

[24] Sachs, P. (1978). Wind forces in engineering, 2nd edn:24. Oxford: Pergamon Press.

[25] American Association of State Highway and Transportation Officials (AASHTO) (1992). Standard specifications for highway bridges, Washington, D.C., 15th edn, 686 pp.

[26] CLAUSEN, C.J.F., et al., 1975. Observed behaviour of the Ekofisk oil storage tank foundation.

[27] Andersen, K.H. 1991. Foundation design of offshore gravity structures. In Cyclic Loading of Soils. From Theory to Design. Edited by M.P. O'Reilly and S.F. Brown. Blackie and Son Ltd., Glasgow and London. pp. 122–173. (Also published in Publikasjon - Norges Geotekniske Institutt, Vol. 185.).

[28] Eurocode 7: Geotechnical design - Part 1: General rules [Authority: The European Union Per Regulation 305/2011, Directive 98/34/EC, Directive 2004/18/EC]

[29] Christos Anagnostopoulos and Michael Georgiadis. Interaction of axial and lateral pile responses.

[30] Sheikh Sharif Ahmed and Bipul Hawlader, 2016. Numerical Analysis of Large-Diameter Monopiles in Dense Sand Supporting Offshore Wind Turbines. DOI: 10.1061/(ASCE)GM.1943-5622.0000633. © 2016 American Society of Civil Engineers.

[31] Knut H. Andersen. Bearing capacity under cyclic loading — offshore, along the coast, and on land. The 21st Bjerrum Lecture presented in Oslo, 23 November 2007. DOI:10.1139/T09-003

[32] Principles of Foundation Engineering, SI. Seventh Edition. BRAJA M. DAS.

[33] Meyerhof, G. G. (1976). *Bearing Capacity and Settlement of Pile Foundations*, Journal of the Geotechnical Engineering Division, American Society of Civil Engineers, Vol. 102, No. GT3, pp. 197–228. With permission from ASCE.

[34] Vesic, A. S. (1977). *Design of Pile Foundations*, National Cooperative Highway Research Program Synthesis of Practice No. 42, Transportation Research Board,Washington, DC.

[35] Federal Highway Administration Research and Technology, *Analyses of the lateral load tests at the route 351 bridge*, March 2006, FHWA-HRT-04043.

[36] Richard C. Aster et al. (2005). Parameter Estimation and Inverse Problems. ISBN: 0-12-065604-3

[37] Augustesen, A. H., Brødbæk, K. T., Møller, M., Sørensen, S. P. H., Ibsen, L. B., Pedersen, T. S., & Andersen, L. (2009). Numerical Modelling of Large-Diameter Steel Piles at Horns Rev. In B. H. V. Topping, L. F. C. Neves, & R. C. Barros (Eds.), Proceedings of the Twelfth International Conference on Civil, Structural and Environmental Engineering Computing. Civil-Comp Press. (Civil-Comp Proceedings; No. 91).

[38] Reese, L.C., W.R. Cox & F.D. Koop 1975. Field testing analysis of laterally loaded piles in stiff clay; *Proceedings of the VII Annual Offshore Technology Conference, Houston, Texas,* 2(OTC 2312): 672-690.

[39] M. Achmus, K. Abdel-Rahman, Y.-S. Kuo. Numerical Modelling of Large Diameter Steel Piles under Monotonic and Cyclic Horizontal Loading. Leibniz University of Hannover, Hannover, Germany.

[40] B.B. Broms (1964). Lateral resistance of piles in cohesive soils. Journal of the soil mechanics and foundations division, ASCE.

[41] R.B. Gilbert et al. (2015). Design of Wind Turbines Monopiles for Lateral Loads

[42] H. Matlock (1970). Correlation for Design of Laterally Loaded Piles in Soft Clays. 2nd Offshore Technology Conference, Houston, Texas, 577-594.

[43] C.G. Feslikenian, L. Zdravkovic. Practical engineering analysis of laterally loaded monopiles for wind turbines.

[44] Wolf, T. K., Rasmussen, K. L., Hansen, M., Roesen, H. R., & Ibsen, L. B. (2013). Assessment of p-y Curves from Numerical Methods for a non-Slender Monopile in Cohesionless Soil. Aalborg: Department of Civil Engineering, Aalborg University. (DCE Technical Memorandum; No. 024).

[45] Suched Likitlersuanga et al. (2013). Small strain stiffness and stiffness degradation curve of Bangkok Clays.

[46] L.J. Prendergast n, K. Gavin (2015). A comparison of initial stiffness formulations for small-strain soil–pile dynamic Winkler modelling.